# LOW RADON PERMEABLE GLOVES AND LASERBALL SIMULATIONS FOR SNO+

BY

Zachariah Carranza-Barnard

Thesis submitted in partial fulfillment
of the requirements for the degree of
Master of Science (MSc) in Physics

The School of Graduate Studies
Laurentian University
Sudbury, Ontario, Canada

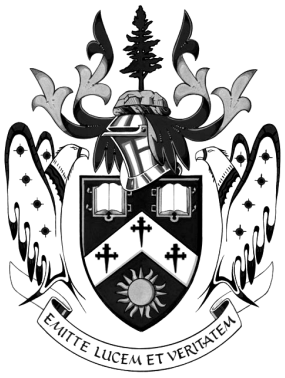

## THESIS DEFENCE COMMITTEE/COMITÉ DE SOUTENANCE DE THÈSE

**Laurentian Université/Université Laurentienne**
School of Graduate Studies/École des études supérieures

| | |
|---|---|
| Title of Thesis<br>Titre de la thèse | LOW RADON PERMEABLE GLOVES AND LASERBALL SIMULATIONS FOR SNO+ |
| Name of Candidate<br>Nom du candidat | Carranza-Barnard, Zachariah |
| Degree<br>Diplôme | Master of Science |

| | | | |
|---|---|---|---|
| Department/Program<br>Département/Programme | Physics | Date of Defence<br>Date de la soutenance | December 10, 2013 |

**APPROVED/APPROUVÉ**

Thesis Examiners/Examinateurs de thèse:

Dr. Christine Kraus
(Supervisor/Directrice de these)

Dr. Chris Jillings
(Committee member/Membre du comité)

Dr. Doug Hallman
(Committee member/Membre du comité)

Dr. Andrew Sonnenschein
(Committee member/Membre du comité)

Approved for the school of Graduate Studies
Approuvé pour l'École des études supérieures
Dr. David Lesbarrères
M. David Lesbarrères
Director, School of Graduate Studies
Directeur, École des études supérieures

**ACCESSIBILITY CLAUSE AND PERMISSION TO USE**

# Abstract

The SNO+ experiment is a multipurpose liquid scintillator detector whose first goal is to measure neutrinoless double beta decay. This thesis describes two important components: simulations to optimize the time window for the prompt peak of an optical calibration source, the "laserball" and the search for gloves to handle calibration sources while maintaining stringent background conditions.

Non-direct light found in laserball runs creates challenges for optical calibration. By changing the time profile from the standard $\pm 4ns$ to an asymmetric profile of $^{+2}_{-4}\ ns$ this contribution of non-direct light can be reduced up to 45%.

Gloves provide an access point to manipulate calibration sources during deployment inside the detector and as barrier to $^{222}$Rn, a known background to the experiment. However, typical glove materials are found to permeate large amounts radon. Through a careful selection process the material Silver Shield was chosen for use in SNO+ with a permeation rate of $1.1 \times 10^{-6}$ radon atoms/hour.

# Acknowledgments

First and foremost I would like to thank my supervisor, Christine Kraus. Without her encouragement, guidance and keeping me on track this thesis would probably not have come together as well as it did and in such a short span of time. Her positive attitude towards the work I have done has instilled in me a great deal of confidence that I have never had before.

I would also like to thank my wife, Samantha Carranza-Barnard, for keeping me well fed while I slacked off from household chores to focus on writing. Her cat herding skills are also appreciated for keeping away the cute cat distractions known as Archimedes and Lola. But most of all, I thank her for her never ending love and support.

Thank also to the SNO+ collaboration for allowing me to play my part on the forefront of particle physics. I am looking forward to read about the success of the experiment in the future!

I would also like to thank all the local SNO+ members for all the good times cracking jokes at Laurentian University or just chatting away waiting for the 4 pm surface cage. In particular I would like to thank Mike Schwendener and Dave Braid for all the hours they put in as bottom guards and keeping an eye out for me.

Thanks to Ben Davis-Purcell for all the hard work keeping up with me during those long afternoon shifts cleaning the acrylic vessel. We were pretty much the AV cleaning dream team. I still do not understand how you can eat so much.

I would also like to thank my internal committee members, Chris Jillings and Doug Hallman for reviewing my thesis. Also thank you to Andrew Sonnenschein, my external committee member, for taking the time to go over my thesis. Your outside opinion is greatly

appreciated.

I would also like to thank everyone who went out of their ways to pick me up for those early 6 am cage times.

# Table of Contents

# List of Figures

**Chapter 5**

**Chapter 6**

# List of Tables

# Chapter 1: Introduction

One of the most interesting particles found in nature is the neutrino. There are many different sources of neutrinos; for example they are created in great abundance in fundamental processes inside the Sun. Of the four fundamental forces of nature (electromagnetism, gravity, the strong nuclear force, and the weak nuclear force) neutrinos only interact through the weak nuclear force, unlike most (standard) matter which interact through the electromagnetic force. As a result neutrinos can pass harmlessly through solid matter. In fact if you take a small area on your body there are billions and billions of neutrinos that pass through every second, whether it be day or night. This also means that detection of neutrinos is somewhat of a challenge. However, by observing weak force interactions in tonne scale and extremely sensitive detectors, physicists have been able to learn more about this elusive particle.

What we know about neutrinos is that they come in three different "flavours", the electron neutrino, the muon neutrino and the tau neutrino, each with their own respective anti-neutrinos. This naming convention follows the other leptons, the electron, the muon and the tau particles. We also know that neutrinos oscillate. When a neutrino is created it exists as a specific flavour, but as it travels long distances it is the mass eigenstates that are important. From the superposition of mass eigenstates that one can determine what flavour the neutrino is detected as. As a result, we can also imply that neutrinos have a non-zero mass, otherwise this oscillation could not occur.

One of the challenges with neutrino physics is that we have yet to measure or deduce the masses of each neutrino.[1] This knowledge is useful because it can further the understanding

[1] An upper limit for the sum of all three flavours of neutrinos has been set by the Plank observatory by measuring the cosmic microwave background to $\sum m_\nu < 0.32\ eV$, although this relies heavily on the

of how neutrinos affected the evolution of the universe and perhaps explain why we see more matter than antimatter in the universe.

A summary of each Chapter is presented here. Chapter 2 presents a short summary of the rich and extensive history of neutrino physics. In particular the contribution to the knowledge of neutrino oscillation theory from the Sudbury Neutrino Observatory (SNO) is included. The SNO experiment is the predecessor to the SNO+ experiment, meaning that SNO+ inherited the hardware left behind after the conclusion of the SNO experiment. In addition, neutrinoless double beta decay is introduced. Searches for neutrinoless double beta can determine if neutrinos are indeed Majorana particles as predicted by theory and has the potential for determining neutrino mass scale.

Chapter 3 introduces how SNO+ plans to measure neutrinoless double beta decay by using a liquid scintillator detector. In addition, this Chapter will also cover the other physics goals that SNO+ plans to achieve by observing solar neutrinos, nuclear reactor neutrinos, geo-neutrinos and even possibly neutrinos from an (inter)galactic supernova. Furthermore, changes that are required to transition from the SNO experiment to the SNO+ experiment will be discussed, which also includes expected backgrounds and the need for cleanliness and low radioactive components.

The calibration system used in SNO+, including details of specific components involved, will be covered in Chapter 4. This Chapter will show how natural radioactivity in the air, specifically from radon, is kept to a minimum through special design features for the calibration system and the use of a "cover gas".

My own contribution to the calibration system, through simulations of an optical calibration source known as the laserball, is described in Chapter 5. These simulations study in detail the contribution of delayed light in scintillator that is produced through absorption/re-emission and Rayleigh scattering in the scintillator.

Chapter 6 will cover my contribution in reducing the amount of radon that is allowed into the SNO+ experiment by selecting an appropriate glove material for the calibration system. The glove material needs investigation because typical polymer membranes used

assumptions in the model [1]. The upper limit from direct measurements for the electron flavour neutrino was measured to be $m_{\nu_e} < \sim 2\ eV$ [2] by measuring tritium $\beta$ decays in the Mainz experiment.

by glove manufacturers are known to allow radon to diffuse through them. By studying the permeability between two different low permeable materials and how the gloves can be used an informed choice can be made for the ideal glove material used for SNO+.

In summary, this thesis is written on the multipurpose SNO+ experiment, which is capable of improving on the knowledge of neutrino physics in several areas. It also shows the amount of consideration needed to reduce the amount of radioactive background from just one source, radon. Even from my own contribution to a small piece of the calibration system, the gloves, can make all the difference in success of the entire experiment. This work reflects the effort required in developing and operating a neutrino detector and how this work is necessary to push the understanding of neutrino physics to the next level.

# Chapter 2: Neutrino Physics

## 2.1 History of the Neutrino

The neutrino hypothesis was a solution to a problem found in the radioactive process known as beta ($\beta$) decay. In the beginning of the twentieth century $\beta$ decay was understood as a two-body decay process of one atom transforming into another atom by the release of an electron. Due to conservation of energy and momentum, a two-body decay should result in a discrete energy spectrum; however this was not what was observed. It was confirmed in 1927 by Ellis and Wooster that the $\beta$ decay process did in fact produce a continuous energy spectrum [3]. One solution to this problem put forth by Bohr was that $\beta$ decay actually violated conservation of energy.

A second proposal to the missing energy came from Pauli's idea of an extremely light, on the same scale as an electron, electrically neutral particle that he called the "*neutron*" [4]. This *neutron* would also be emitted during $\beta$ decay, creating the observed continuous spectrum, but was simply not yet observed. Two years later the neutron, as we know it today, was discovered by Chadwick in 1932 [5], which could not be Pauli's proposed particle because it was too massive. It was Fermi who made the distinction between the two by renaming Pauli's *neutron* to "neutrino", Italian for little neutral one. Fermi further expanded on Pauli's ideas into the theory of $\beta$ decay and assumed neutrinos to be massless [6].

It took 23 years after Fermi's theory before the actual experimental observation of the neutrino. In 1956, Cowan and Reines did not detected the neutrino but instead detected the neutrino's antiparticle the anti-neutrino ($\bar{\nu}$) [7]. Originally Cowan and Reines proposed to

find neutrinos from nuclear explosions but found that nuclear reactors produced a sufficient amount of neutrinos as well. Their detector used water with 40 kg of $CdCl_2$ dissolved into two 100 l tanks as a target material and was placed in between three layers of liquid scintillator, in which was described as a "club sandwich". The anti-neutrinos were then detected by the inverse $\beta$ decay reaction,

$$\bar{\nu} + p \rightarrow n + e^{+}. \tag{2.1}$$

The positron produced annihilates immediately with an electron creating two gamma rays that are emitted in the opposite direction, then 3 to 10 microseconds later the neutron is captured by cadmium creating another gamma ray. This delayed coincidence signal provided a clear way to distinguish likely neutrino events from other background signals. Furthermore, Cowan and Reines had the ability to shut down the reactor and compare the signal rate, solidifying the evidence that they had indeed detected the neutrino.

A second type of neutrino, the muon neutrino ($\nu_\mu$), was discovered in 1962 by Lederman *et al.* from decays in pions created by the Alternating Gradient Synchrotron (AGS) particle accelerator [8]. With two types of neutrinos it was established that neutrinos came in different "flavours", and similarly the first generation of neutrino, the electron neutrino ($\nu_e$), was named after its associated lepton, the electron. Maki, Nakagawa and Sakata suggested that a partial mixture of states could exist between the two neutrino flavours in the same year [9]. The first concept of neutrino oscillations came from Pontecorvo. Pontecorvo proposed in 1957 that neutrinos could oscillate with its antiparticle the anti-neutrino [10], but later extended his theory with $\nu_e \Leftrightarrow \nu_\mu$ oscillations in 1968 [11] following the discovery of the muon neutrino.

The third generation of lepton, the tau, was discovered at the Stanford Linear Accelerator Center (SLAC) in 1975 [12] and the existence of a corresponding neutrino flavour was predicted. Furthermore, using precise measurements of the the Z boson, in 1989, the Stanford Linear Collider (SLC) and the Large Electron-Positron Collider (LEP) constrained the number of neutrino flavours to three [13], also predicting a third neutrino flavour. By

2000 the Direct Observation of the NU Tau (DONUT) experiment was finally able to confirm the existence of the tau neutrino from the decay of charmed mesons produced by the Tevatron [14]. This was achieved by carefully tracking the paths of particle interactions in the DONUT detector and using the characteristics of a tau lepton decay.

One big problem in neutrino physics came in 1968, with the first detection of neutrinos from the Sun. This was accomplished by R. Davis *et al.* in the Homestake experiment[15] using a 100,000 gallon detector of perchloroethylene, which was chosen because it is rich in chlorine . Neutrino detection was seen through neutrino capture on the chlorine,

$$\nu_e + {}^{37}Cl \rightarrow {}^{37}Ar + e^- \tag{2.2}$$

and measuring the decay of $^{37}$Ar in a proportional counter. To do so single atoms of $^{37}$Ar had to be able to be removed from the detector, which Homestake was the first experiment to do so.

The problem itself came from measured neutrino flux by Homestake, which was found close to one-third the predicted solar neutrino flux calculated by Bahcall and Shaviv [16]. This deficit in the solar neutrino flux was also observed and confirmed by other solar neutrino detectors including Kamiokande-II [17], IMB [18] and GALLEX [19]. This became a big problem in the field of neutrino physics and was subsequently named the "Solar Neutrino Problem".

### 2.1.1 The Sudbury Neutrino Observatory

The Sudbury Neutrino Observatory (SNO) was designed specifically to resolve the Solar Neutrino Problem [20]. The Solar Neutrino Problem was a major discrepancy between the measured solar neutrino flux and the predicted solar models. SNO is brought up because the majority of the hardware used in SNO will be also used in the SNO+ experiment; more detail will be presented in Chapter 3.1.

SNO was built between 1990-1999 and located 2,070 m underground in Canada's deepest nickel mine, VALE's Creighton Mine. The experiment was placed deep underground to

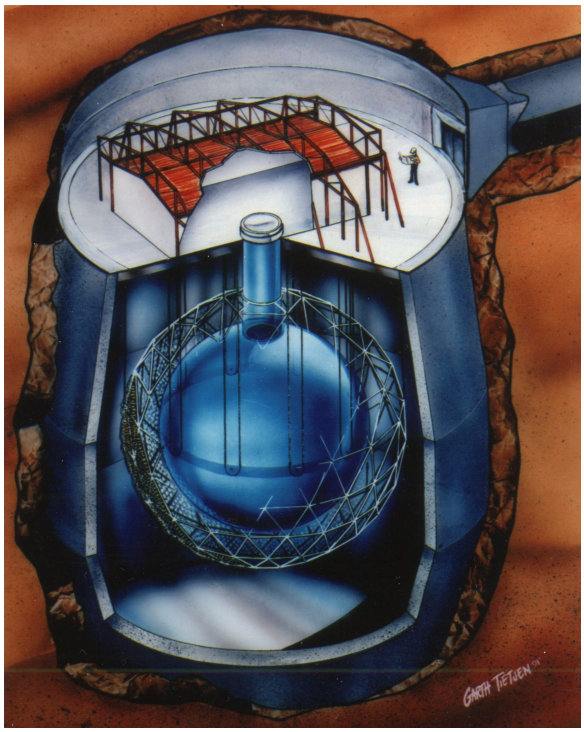

Figure 2.1: An artist's rendition of the SNO detector showing off the acrylic vessel with the hold up ropes and the photomultiplier support structure.

provide 6000 meters water equivalent ($m.w.e.$) of shielding from cosmic radiation. The target material consisted of 1,000 tonnes heavy water, $D_2O$, which was held inside a 12 m diameter acrylic vessel (AV), see Figure 2.1. Surrounding the AV was approximately 9500 photomultiplier tubes (PMTs) that were secured to a 18 m stainless steel frame, known as the PMT support structure (PSUP). The detector was additionally suspended in 7400 tonnes of ultra-pure light (normal $H_2O$) water which was used as additional shielding to radioactive backgrounds coming from the rock walls. Also, the AV was held up with ropes for additional support because heavy water is in fact heavier than normal water.

The ultimate purpose of SNO was to distinguish electron-neutrino events, through a process known as the charged current interaction (CC), from all flavours of neutrino through the neutral current interaction (NC). By comparing the ratios of the CC to the NC, SNO would prove that the missing neutrinos flux was a direct result of neutrino flavour change. This would also indicate that the Solar Neutrino Problem only occurred because past experiments were only sensitive to the electron neutrino.

The charged current and neutral current are two nuclear interactions with the deuterium in $D_2O$

$$\nu_e + D \rightarrow p + p + e^- \quad (CC) \ , \tag{2.3}$$

$$\nu_x + D \rightarrow \nu_x + n + p \quad (NC) \ . \tag{2.4}$$

In the charged current interaction the neutrino creates its partner lepton. Therefore, at low neutrinos energies, only the electron neutrino can participate in this process. For the neutral current interaction, this process can occur for all three neutrino flavours. However, no neutrino flavour can be distinguish and thus the neutrino is denoted $\nu_x$. In addition, neutrinos were also detected from neutrino-electron elastic scattering,

$$\nu_x + e^- \rightarrow \nu_x + e^- \quad (ES) \ . \tag{2.5}$$

These events are six times more likely to occur from electron neutrinos than the other respective flavours. The signals produced by these events were then detected by the PMTs by collecting the corresponding Čerenkov light.

SNO published its first scientific results in June 2001, measuring the non-electron neutrino flavour contribution to the solar neutrino flux, and confirmed that the total solar neutrino flux was in agreement to predicted solar models [21]. Furthermore the measured $\nu_e$ flux in SNO was also consistent with the Homestake experiment. These results provided evidence that the missing neutrino flux was a direct product of neutrino flavour oscillation and further implied, from oscillation theory, that neutrinos have a non-zero mass.

## 2.2 Neutrino Oscillation

In the standard model of particle physics there are three distinct neutrino flavours, $\nu_e$, $\nu_\mu$, $\nu_\tau$, which also have corresponding anti-neutrinos. From the confirmation of neutrino oscillations from SNO and other past experiments, neutrinos are known to change flavour. Thus the neutrino flavour is a weak eigenstate and neutrinos must have mass. This oscillation is

accounted for by introducing mass eigenstates of the Hamiltonian in free space. The three neutrino flavours along with masses $m_1$, $m_2$, $m_3$ are related by the weak eigenstate by

$$|\nu_\alpha\rangle = \sum_{j=1}^{3} U_{\alpha,j}\ |\nu_k\rangle, \qquad \alpha \in \{e, \mu, \tau\}, \quad j \in \{1, 2, 3\} \tag{2.6}$$

where $U_{ij}$ is the transformation matrix from flavour and mass eigenstates known as the Pontecorvo-Maki-Nakagawa-Sakata (PMNS) matrix [22]. The PMNS matrix can be expressed in a general form in terms of three rotation angles and one complex phase. For convenience the mixing angles for neutrino oscillations are labelled $\theta_{13}$, $\theta_{23}$, $\theta_{13}$, and the complex phase space as $\delta$. The PMNS matrix is represented as thus,

$$U_{\alpha,j} = \begin{pmatrix} 1 & 0 & 0 \\ 0 & c_{23} & s_{23} \\ 0 & -s_{23} & c_{23} \end{pmatrix} \begin{pmatrix} c_{13} & 0 & s_{13}e^{-i\delta} \\ 0 & 1 & 0 \\ -s_{13}e^{i\delta} & 0 & c_{13} \end{pmatrix} \begin{pmatrix} c_{12} & s_{12} & 0 \\ -s_{12} & c_{12} & 0 \\ 0 & 0 & 1 \end{pmatrix} \tag{2.7}$$

where $c_{mn} = \cos(\theta_{mn})$, $s_{mn} = \sin(\theta_{mn})$. The mixing angle provides a measure for the contribution of neutrino with a specific flavour to a neutrino with a specific mass. Neutrino oscillations would not exist if the mixing angles were zero. This complex phase $\delta$ term is non-zero only if neutrinos violate CP-symmetry [23], which would be an explanation why there is an observed excess of matter seen in the Universe, as opposed to equal parts matter and anti-matter.

Unfortunately neutrino flavour oscillations only depend on the differences of the squares of the masses, instead of the absolute masses of neutrinos. This comes from the measuring the probability that a neutrino created with a given flavour is observed as another flavour. Considering the two neutrino case this is just,

$$P_{\alpha\to\beta} = \sin^2(\theta_{jk}) \sin^2\left(\frac{\Delta m^2_{jk} L}{4E}\right) \qquad \alpha \neq \beta \tag{2.8}$$

where $\theta_{jk}$ is the mixing angle between neutrino masses, $\Delta m^2_{jk} \equiv m^2_j - m^2_i$, $L$ is the distance

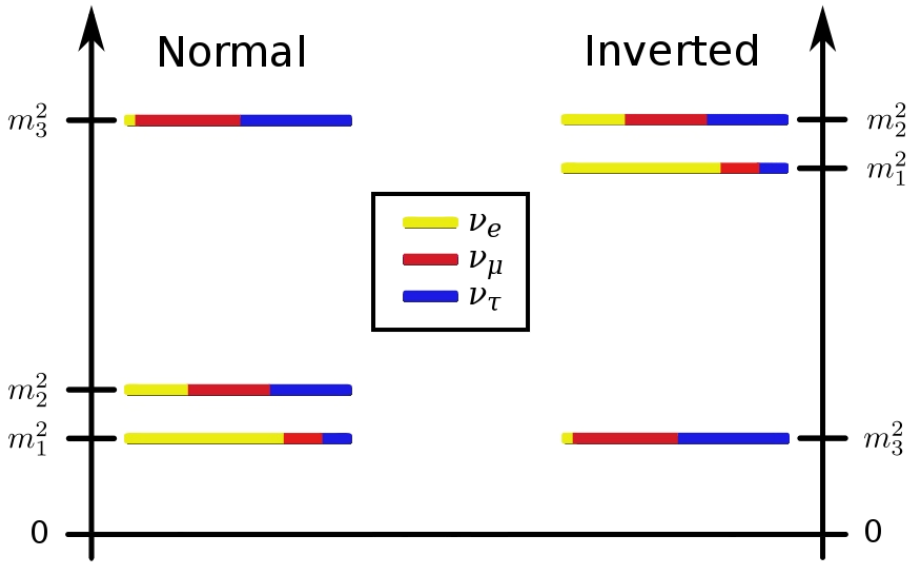


Figure 2.2: A visual representation of the normal and inverted neutrino mass hierarchies.

travelled by the neutrino, and $E$ is the energy of the neutrino.

Additionally there can be two types of configurations, or "hierarchy", to the arrangement of the neutrino mass squared splittings for all three flavours. These different hierarchies are as follows,

$$\text{Normal Hierarchy} : \Delta m^2_{12} \ll \Delta m^2_{23}$$

$$\text{Inverted Hierarchy} : \Delta m^2_{12} \ll |\Delta m^2_{13}|$$

where it is still unknown whether $\Delta m^2_{13}$ has positive or negative sign. The "normal" hierarchy is referred as such because it is comparable to the mass hierarchy of leptons, $m_e < m_\mu < m_\tau$. These different hierarchies are also shown in Figure 2.2. Currently the best measurements for the mass differences squared are $\Delta m^2_{21} = 7.50^{+0.19}_{-0.20} \times 10^{-5}\ eV^2$ from the KamLAND experiment solar data [24], and $\Delta m^2_{32} = |2.32^{+0.12}_{-0.08} \times 10^{-3}|\ eV^2$ from the MINOS experiment [25].

## 2.3 Neutrinoless Double Beta Decay

Double beta decay, $2\nu\beta\beta$, is a rare process which occurs in an isotope when a single beta decay is energetically forbidden. The isotope then can undergo two beta decays simultaneously,

$$(Z, A) \rightarrow (Z + 2, A) + 2e^- + 2\bar{\nu}_e \ . \tag{2.9}$$

This situation is capable of occurring naturally in 35 even-even nuclei, but has only been observed in 11 isotopes. These observed isotopes are $^{48}$Ca, $^{76}$Ge, $^{82}$Se, $^{96}$Zr, $^{100}$Mo, $^{116}$Cd, $^{128}$Te, $^{130}$Te, $^{136}$Xe, $^{150}$Nd, and $^{238}$U.

A far more interesting phenomenon than double beta decay is the neutrinoless double beta decay. This event would only occur if the neutrino could act as its own anti-particle,

$$(Z, A) \rightarrow (Z + 2, A) + 2e^- \ , \tag{2.10}$$

where one nucleon absorbs the neutrino emitted by the other nucleon. The expected probability of observing neutrinoless double beta decay is extremely small. If neutrinoless double beta decay is measured then neutrinos would be the first Majorana particle observed, where all other particles are Dirac particles (distinct particle/anti-particle pairs). A Majorana particle would also be a violation of lepton number conservation. The Feynman diagrams both for double beta decay and neutrinoless double beta decay are shown in Figure 2.3.

If the neutrino is found to be a Majorana particle it will also have its own contribution to the PMNS Matrix, $U_{j,k}^{Maj}$,

$$U_{j,k}^{Maj} \equiv \begin{pmatrix} e^{i\alpha_1/2} & 0 & 0 \\ 0 & e^{i\alpha_2/2} & 0 \\ 0 & 0 & 1 \end{pmatrix} \ , \tag{2.11}$$

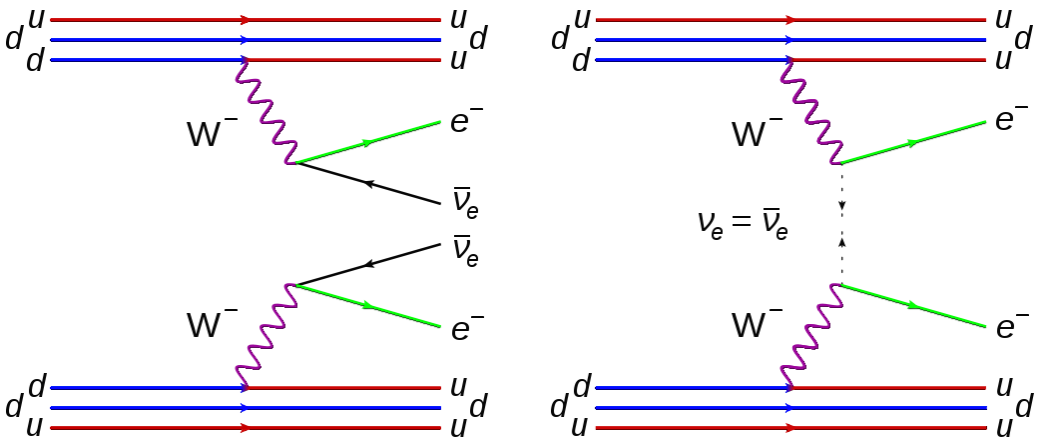


Figure 2.3: Feynman diagrams for both double beta decay and neutrinoless double beta decay.

where $\alpha_m$ are Majorana the phases.

What makes the discovery of the Majorana particle so interesting, other than being a new type of particle, is that it would also provide a measurement of the effective neutrino mass. The decay rate ($\Gamma$) for neutrinoless double beta decay is related to the effective Majorana mass by,

$$\Gamma = G \, |M|^2 < m_{\beta\beta} >^2 \tag{2.12}$$

where $G$ is the phase space factor, $M$ the nuclear matrix element and $m_{\beta\beta}$ the effective Majorana neutrino mass. This effective Majorana neutrino mass is then related to the neutrino masses by,

$$| < m_{\beta\beta} > | \equiv \Big| \sum_{k=1}^{3} m_k U_{\nu_e,k}^2 \Big| \, , \tag{2.13}$$

where $m_i$ are the three neutrino masses and $U_{\nu_e,k}$ are the elements of the PMNS mixing matrix coupling the mass states to the electron neutrino flavour state. Only the electron neutrino flavour state needs to be considered typically because only electron neutrinos are "seen" in experimental detectors; detectors are not large enough to see neutrino oscillations from an internal source.

| Nuclide | $2\nu\beta\beta$ half-life [$10^{21}$ y] | Q-Value [$MeV$] | Natural Abundance [%] |
|---|---|---|---|
| $^{48}$Ca | 0.044 | 4.274 | 0.187 |
| $^{76}$Ge | 1.74 | 2.039 | 7.8 |
| $^{82}$Se | 0.096 | 2.996 | 9.2 |
| $^{96}$Zr | 0.0235 | 3.348 | 2.8 |
| $^{100}$Mo | 0.00711 | 3.035 | 9.6 |
| $^{116}$Cd | 0.028 | 2.809 | 7.8 |
| $^{130}$Te | 0.7 | 2.530 | 34.5 |
| $^{136}$Xe | 2.38 | 2.462 | 8.9 |
| $^{150}$Nd | 0.00911 | 3.372 | 5.6 |

Table 2.1: Isotopes that have been measured exhibiting double beta decay along with the known $2\nu\beta\beta$ half-life, $0\nu\beta\beta$ Q-Values and the natural abundance of the isotope [26].

## 2.4 Double Beta Decay Experiments

Double beta experiments are specifically built around a single isotope chosen from known isotopes that exhibit double beta decay, these isotopes and their properties are summarized in Table 2.1. Since neutrinoless double beta decay occurs at a much lower rate then double beta decay, so low it has yet to be measured[1], current results are limited by low counting statistics and backgrounds. Thus experiments need to be designed with low background, excellent energy resolution and large amounts of double beta isotope. Due to cost and complexity constraints, experiments can be separated by those with good energy resolution versus those with large isotope mass.

Currently the best limit on the rate of neutrinoless double beta decay is set by the GERmanium Detector Array (GERDA). The GERDA experiment used detectors made of ∼86% enriched $^{76}$Ge immersed in a liquid argon cryostat, located at Laboratori Nazionali del Gran Sasso, Italy. The total exposure used in the analysis of their latest paper amounts to 21.6 $kg\ yr$ of enriched germanium. This lead to a limit on the half life of neutrinoless double beta decay of $T^{0\nu}_{1/2} > 2.1 \times 10^{25}\ yr$ at 90% C.L [28].

[1] A claim of observing neutrinoless double beta decay was made by a subset of members from the Heidelberg-Moscow collaboration, known as the Klapdor claim [27], however this claim is controversial at best.

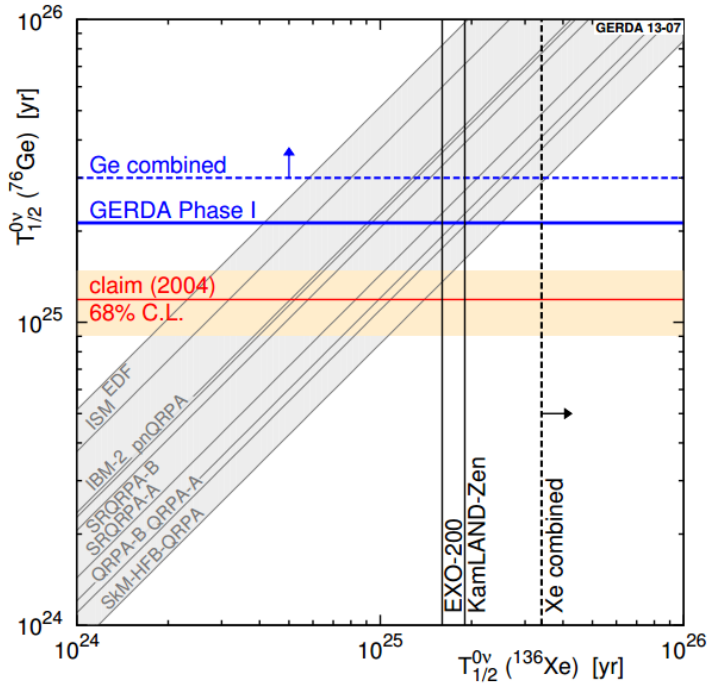


Figure 2.4: Comparing nuclear matrix elements from $0\nu\beta\beta$ limits from $^{76}$Ge with GERDA and $^{136}$Xe with EX0 and KamLAND-Zen. The shaded grey lines are predictions for the correlation of half lives between the two isotopes [28].

Similar recent results were observed for $^{136}$Xe by the Enriched Xenon Observatory (EXO) and the Kamioka Liquid scintillator Anti-neutrino Detector Zero Neutrino (KamLAND-ZEN). EXO measured double beta decay by using 200 $kg$ pure liquid xenon enriched to 80% $^{136}$Xe kept liquid by being cooled by a cryostat. KamLAND-ZEN used a different approach and instead loaded 2.5% of ~90% enriched $^{136}$Xe gas into 13 tonnes liquid scintillator, giving them ~300 $kg$ of double beta isotope. These experiments set limits on the half life of neutrinoless double beta decay to $T^{0\nu}_{1/2} > 1.6 \times 10^{25}\ yr$ [29] and $T^{0\nu}_{1/2} > 1.9 \times 10^{25}\ yr$ [30] both at the 90% C.L. respectively.

The effective Majorana mass limits are not mentioned because of differences in nuclear matrix elements, $|M|^2$. Nuclear matrix elements are not easily calculated, and thus there can be a wide range of effective Majorana masses. From the limits set by the previously mentioned experiments, a comparison between $^{76}$Ge and $^{136}$Xe is shown in Figure 2.4 with different nuclear matrix elements in grey. Notice that there is a factor of 2-3 between different nuclear matrix elements. By observing neutrinoless double beta decay in multiple

isotopes, this could also exclude different nuclear matrix element models and improve measurements on effective Majorana mass.

The SNO+ experiment will be using $^{130}$Te for the double beta isotope, mainly due to its large natural abundance of 34.5%. SNO+ will load 0.3% Tellurium into 780 tonnes of liquid scintillator. Another upcoming experiment to use tellurium is the Cryogenic Underground Observatory for Rare Events (CUORE) in at Gran Sasso, Italy. CUORE uses a different approach with an array of 988 bolometric detectors containing 204 $kg$ of $^{130}$Te.

## 2.5 Scintillator Experiments

The SNO+ experiment will be utilizing a liquid scintillator approach. A scintillator is just a material that is easily excited by ionizing radiation and emits light. Other past liquid scintillator experiments in the field of neutrino physics include the KamLAND and Borexino experiments.

KamLAND and SNO+ are very similar experiments in that both are multipurpose neutrino detectors. Both are able to see neutrinos from the Sun, and anti-neutrinos from nuclear reactors and from radioactive decays from the Earth's interior (geo-neutrinos). One way that SNO+ will improve on KamLAND is the fact that SNO+ has a larger detector than KamLAND and thus will have a higher event rate. SNO+ will also be able to improve on KamLAND's solar neutrinos measurement because KamLAND was restricted to only measuring $^{8}$B neutrinos due to backgrounds coming from cosmogenic muons, whereas SNO+ will be able to measure $^{8}$B neutrinos at a lower energy and also from other solar processes. SNO+ does not have this problem with cosmogenic muons as a result of ∼6000 meters water equivalent (m.w.e) of shielding from the overburden rock, which leads to a rate of about 70 muons a day [20]. Comparatively the KamLAND experiment only has ∼2700 m.w.e. of shielding which leads to a much higher rate of about 17,000 muons a day [31].

The anti-neutrino measurement from reactors will be improved on by SNO+ because even though KamLAND is closer to reactors and has a higher event rate, SNO+ is at an interesting distance where the neutrino oscillations can be seen in the shape of the signal,

Chapter 3.2.3 will cover this in more detail. SNO+ will also have a better geo-neutrino measurement due to the fact that the experiment is located in the Canadian Shield. The continental crust of the Canadian Shield has a higher concentration of radioactive elements as opposed to the oceanic crust around Japan where the KamLAND experiment is located.

The Borexino experiment is related to SNO+ in not only being a similar scintillator detector but also because Borexino was the first experiment to directly measure *pep* neutrinos [32], one of the physics goals of SNO+. Borexino was also able to set a limit on the CNO neutrino flux. One of the big backgrounds Borexino suffered from is for measuring *pep* and CNO neutrinos comes from $^{11}$C activation from cosmogenic muons. Borexino has $\sim$3800 m.w.e. of shielding, which gives a muon rate of around 4300 muons a day [33]. As mentioned before SNO+ has a lower rate of 70 muons a day and there can improve on measurements taken by Borexino.

# Chapter 3: SNO+

The SNO+ experiment is a new liquid scintillator neutrino detector that is being refurbished from the old SNO detector. A liquid scintillator is an organic liquid that, when excited by ionizing radiation, produces light. Compared with the Čerenkov process utilized in SNO, scintillation has a significantly higher light yield. Because of this higher light output, SNO+ will be sensitive to lower energy events than those seen in SNO. Furthermore, SNO+ also has the sensitivity to observe neutrinos from a broad variety of interesting sources making it a "Swiss Army knife" of neutrino detectors.

## 3.1 SNO+ Detector

The SNO+ detector inherits the majority of its hardware from its predecessor the Sudbury Neutrino Observatory (SNO). The SNO+ detector is located 2,070 $m$ underground in VALE's Creighton Mine. This is to provide 6,000 meters water equivalent ($m.w.e.$) of shielding from cosmic rays and atmospheric muons.

The detector itself consists of a 12 $m$ diameter acrylic vessel (AV) which holds the target material, ∼780 tonnes of the liquid scintillator, linear alkylbenzene (LAB). The detection of signals comes from ∼9500 photomultiplier tubes (PMTs) that look into the detector volume and are held in place by a 18 $m$ geodesic stainless steel support structure; often referred to as the PMT support structure or PSUP. There is an additional 7400 tonnes of ultra-pure water (UPW) shielding that surrounds the AV from additional radiation from the surrounding rock cavity.

By transitioning to scintillator as the target material there are some changes that need

to be made in regards to how the acrylic vessel is anchored. In SNO, "hold-up" ropes were needed to help support the weight of acrylic vessel and the heavy water. SNO+ stills uses the hold up ropes for air fill and water fill stages of the experiment, however the old ropes from SNO have been replaced with new ropes that are lower in radioactivity. Furthermore, because the density of linear alkylbenzene is 862.8 $kg/m^3$ compared to the density of heavy water, 1,110 $kg/m^3$, an additional rope net is used to prevent the acrylic vessel from floating. These "hold-down" ropes are anchored directly to the rock below the cavity and the tension in the ropes is monitored by load cells. Likewise, the tension in the hold-up ropes is also monitored with load cells.

Linear alkyl benzene was chosen for SNO+ because of its relatively high light yield, compatibility with acrylic, high flash point, and low toxicity levels. LAB is composed of a benzene ring attached to a hydrocarbon chain. The benzene ring is the source of the scintillation light, but by itself is toxic to humans. The hydrocarbon chain is responsible for reducing the toxicity of the benzene ring. LAB is also an ingredient used for biodegradable detergents.

In addition, there will be a fluor, 2,5 diphenyloxazole (PPO), added to the liquid scintillator at 2 $g/L$. When the scintillator becomes excited from ionizing radiation this energy is then non-radiatively transferred to the fluor which emits photons at a higher wavelength. This is necessary because if the light is not shifted by the fluor to higher wavelengths the light produced will just be reabsorbed by the scintillator itself.

Furthermore the PMTs that have broken down or been deemed faulty during the lifetime of SNO have been refurbished and re-installed. The electronics and the data acquisition system also have been upgraded to be able to handle the higher data rates expected from scintillator. This includes buffer memory on the read out electronics in order to preserve all data in case of extremely high data rates, which could happen from supernova neutrinos (Chapter 3.2.5).

Because of the stringent background requirements that come with detecting low energy neutrinos, the calibration system for SNO+ has been designed to be completely sealed from the surrounding air. This will be further discussed in detail in Chapter 4.3.

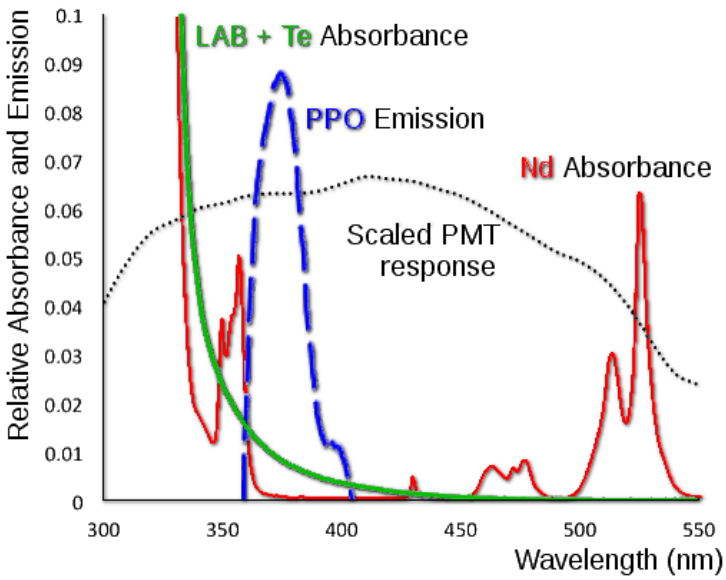


Figure 3.1: Absorption lines of $^{130}$Te loaded scintillator cocktail compared to $^{150}$Nd loaded scintillator and the emission spectrum of PPO.

## 3.2 Physics Goals

As a scintillator detector SNO+ will be able to act as a multipurpose detector being able to observe double beta decay, solar neutrinos, reactor neutrinos, geo-neutrinos and even possibly supernova neutrinos. The experiment is broken down into two different phases. The first phase, double beta phase, involves loading Te isotope into the detector. The second phase, solar phase, involves the search for low energy solar neutrinos. The other reactor, geo and supernova neutrinos can be detected concurrently during both phases.

### 3.2.1 Neutrinoless Double Beta Decay

The first phase of SNO+ will utilized scintillator loaded with $^{130}$Te to search for neutrino less double beta decay. With a loading level of 0.3% and a natural abundance of 34% for $^{130}$Te, this will place 800 $kg$ of double beta decay isotope into the scintillator. While SNO+ is running it will be one of the largest double beta decay experiments to date.

One benefit with Tellurium is that it does not suffer from absorption lines at higher wavelengths that other isotopes can run into, like seen in $^{150}$Nd in Figure 3.1. This

effectively means that increasing the loading percent of Tellurium will not affect the light yield significantly, and thus SNO+ has the potential to load even higher percentage of double beta isotope into the scintillator. However at lower wavelengths, in particular in the region of PPO light emission, there is some light absorption, but this can be circumvented by introducing an additional wavelength shifter.

$^{150}$Nd is mentioned because it was an isotope considered for SNO+. The experiment is not just limited to using $^{130}$Te or $^{150}$Nd as other double beta isotopes can also be loaded into scintillator. The reason why Neodymium was a contender was because its high energy end point of 3.372 $MeV$, which placed it above low energy backgrounds. After careful consideration Tellurium was chosen because the natural abundance of $^{150}$Nd is only 5.6% and enriching Neodymium was not a feasible choice.

However, by going to $^{130}$Te there is a trade off for natural abundance to being susceptible to low energy backgrounds near the endpoint energy of 2.53 $MeV$. The backgrounds that will overlap the $0\nu\beta\beta$ signal region will be covered later in Chapter 3.3.

### 3.2.2 Solar Neutrinos

The second phase of SNO+ will primarily involve the search for low energy solar neutrinos after removing the Tellurium cocktail from the scintillator. With a lower energy threshold around 0.5 MeV, SNO+ will be sensitive to different types of solar neutrinos. Of particular interest are the neutrinos that come from proton-electron-proton fusion, known as the *pep* process, and the carbon-nitrogen-oxygen (CNO) cycle in the Sun.

#### *pep* Neutrinos

The proton-electron-proton (*pep*) neutrinos come from one of initial stages of proton fusion inside the Sun. With the fusion of proton-electron-proton the Sun creates $^{2}$H and emits an electron neutrino. Figure 3.2 shows the whole proton-proton reaction chain that the *pep* process is part of.

The *pep* neutrinos are an excellent tool for studying neutrino oscillation studies primarily from it's low uncertainty of 1.2%, which comes from the luminosity constraint in the solar

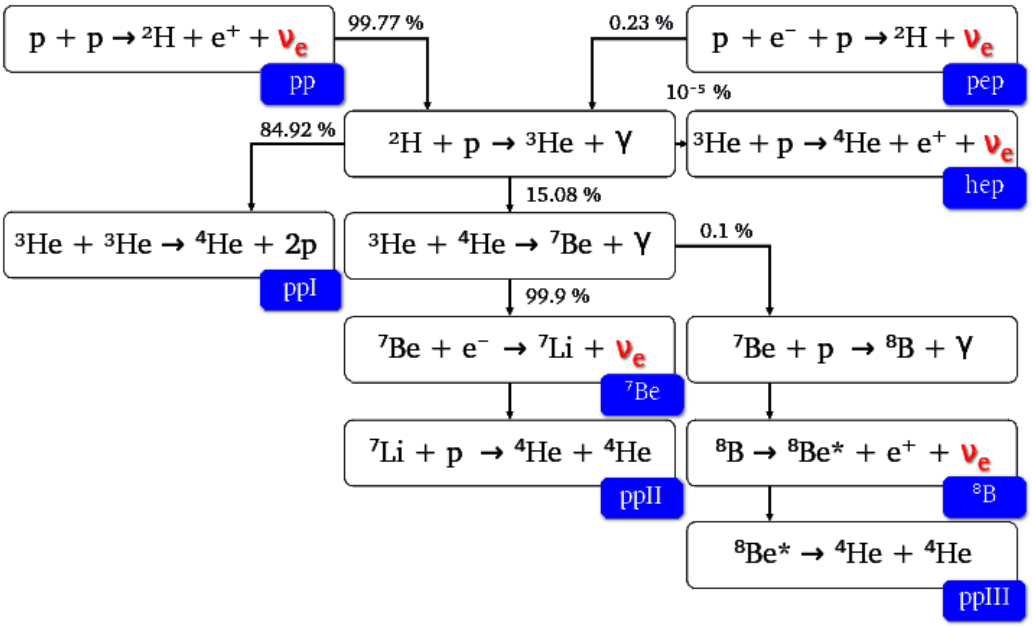


Figure 3.2: Proton-proton reaction chain that occurs in the Sun.

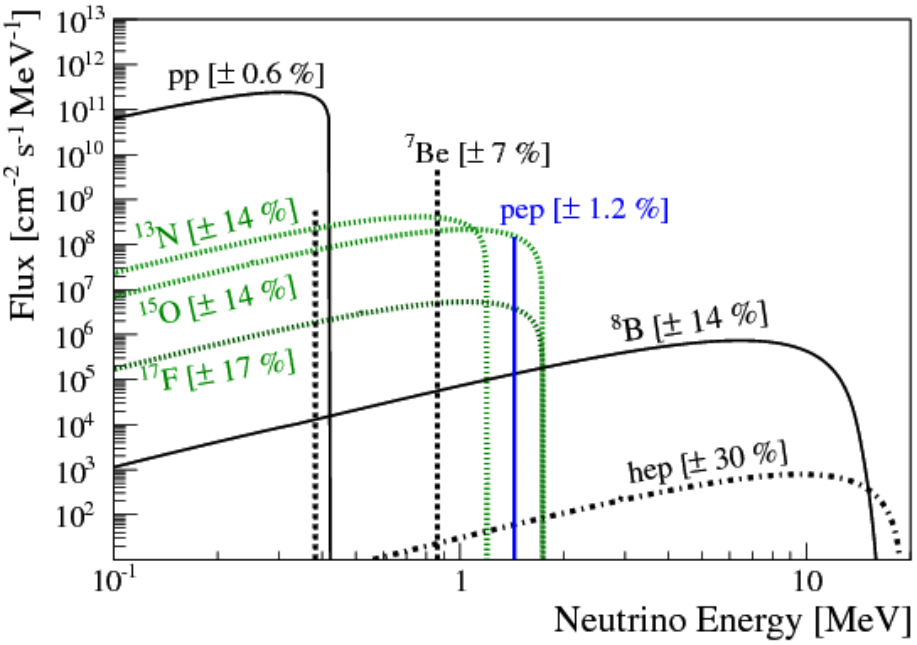


Figure 3.3: Expected solar neutrino fluxes from proton-proton fusion and the CNO cycle with respect to energy, along with their uncertainty [34].

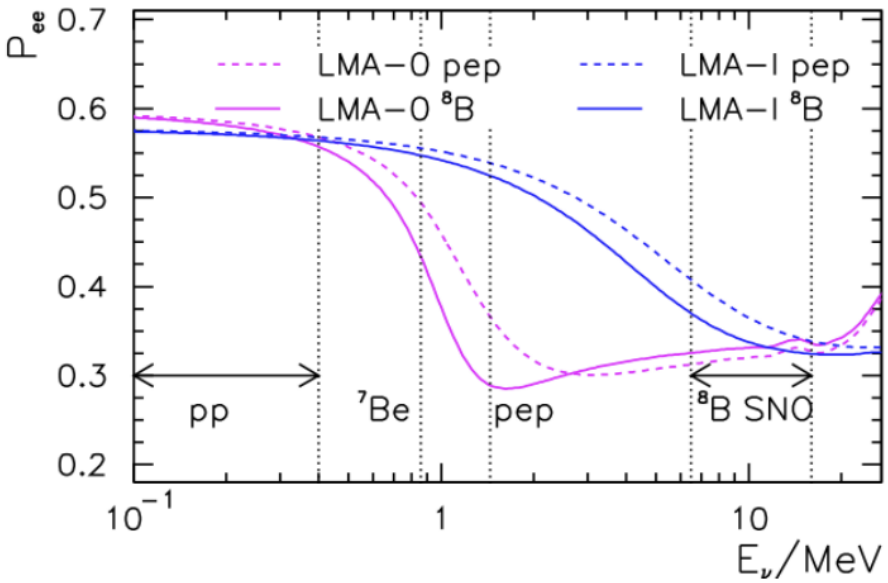


Figure 3.4: Electron neutrino survival probability from neutrinos produced in the Sun averaged over time as a function of neutrino energy. These probabilities assume the existence of non-standard neutrino matter interactions [35].

standard model (SSM) [34]. Since only a electron neutrino is emitted from the *pep* process, the energy of the neutrino is at a single value of 1.44 $MeV$. Figure 3.3 shows the expected neutrino flux for *pep* neutrinos as well from the proton-proton chain in Figure 3.2 and from CNO neutrinos.

SNO+ can also measure the $^8$B neutrinos that were measured in SNO but in an even lower energy region than SNO could measure. Also, SNO+ can measure $^7$Be neutrinos, but due to the larger uncertainty of 7% of the flux rate, $^7$Be neutrinos are less useful for oscillation studies. The *pp* neutrinos would also be excellent to measure because they are the first step in the fusion reaction in the Sun and where the majority of solar neutrinos come from. Furthermore, *pp* neutrinos have an even lower uncertainty in neutrino flux of 0.6% from the SSM. Unfortunately, seeing *pp* neutrinos in SNO+ will be difficult due to intrinsic $^{14}$C backgrounds in the scintillator.

Figure 3.4 shows the probability that an electron neutrino produced in the Sun is detected as an electron neutrino as a function neutrino energy. At high energies matter effects are important and there is a uniformly low survival probability. However, at lower

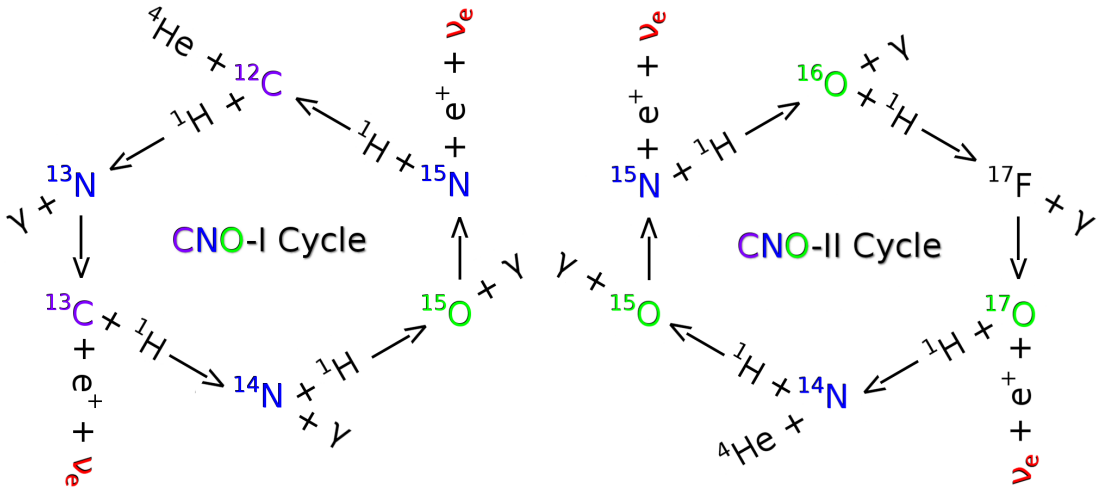


Figure 3.5: The CNO cycles found inside the Sun. CNO-II cycle is a minor branch from CNO-I that occurs only 0.04% of the time. The neutrinos that are produced are highlighted in red.

energies the matter effects eventually give way to vacuum oscillations and the survival probability improves.

The reason why the *pep* neutrino flux is so interesting is because at the energy at 1.44 $MeV$ is in a region where matter dominated oscillations give way to vacuum dominated oscillations. The vacuum dominated and matter dominated extremes have have already been studied but this transition region has not been well measured [35]. Measuring this transition region will help constrain the models used for neutrino oscillation theory and as a probe for sub-dominant effects such as sterile neutrinos and non-standard neutrino matter interactions.

### CNO Neutrinos

Where *pep* neutrinos will give insight on neutrino physics, measurements of CNO neutrinos will probe the physics involved in the inner workings of the Sun. The proton-proton chain reactions are thought responsible for about 98.5% of the Sun's energy, with the CNO cycle contributing only 1.5% [36]. This contribution from the CNO cycle is still quite uncertain and depends on the the amount of "metals" (all elements minus hydrogen and helium) in the Sun. Therefore by measuring the CNO flux, in Figure 3.3, it will be possible for

SNO+ to determine the contribution of energy produced by the CNO cycle and provide a measurement for the metallicity content of the Sun.

### 3.2.3 Reactor Neutrinos

SNO+ will also be able to detect electron anti-neutrinos ($\bar{\nu}_e$) from Bruce, Pickering, and Darlington nuclear power plants. The anti-neutrinos themselves come from beta decay of the fission products of the heavy elements used in nuclear power plants. Because thermal power produced in each nuclear reactor is recorded, the anti-neutrino flux contribution is well known. This also leads to a known energy spectrum of the anti-neutrinos emitted; however it is dependent on the nuclear fuel used.

Anti-neutrinos are easily distinguished in scintillator due to inverse beta decay process,

$$\bar{\nu}_e + p \;\rightarrow\; n + e^+ \;. \tag{3.1}$$

The positron quickly annihilates with a nearby electron while the neutron diffuses through the detector with an average time of $\sim$200 $\mu s$ before being captured by a proton. These two separated events provide a delayed coincidence signal. Furthermore, when the positron is produced it is created with a kinetic energy 1.804 $MeV$ less than that of the anti-neutrino. This relationship between positron and anti-neutrino energy makes measuring the anti-neutrino spectrum relatively easy.

Similarly to solar neutrinos, reactor anti-neutrinos undergo oscillation as they propagate the 240 $km$ from the Bruce reactor and $\sim$330 $km$ from Pickering and Darlington reactors. Because of the well understood anti-neutrino flux and spectrum, measuring the anti-neutrinos from the reactor becomes a powerful tool for studying (anti)neutrino oscillations. This is not the first study of reactor anti-neutrinos, may other scintillator experiments have exploited the free anti-neutrinos produced from reactors such as the KamLAND experiment [37]. What makes a measurement from SNO+ so interesting is that the baseline (distance from the power plants) gives a well defined substructure, such as seen in Figure 3.6, that could not be seen in KamLAND.

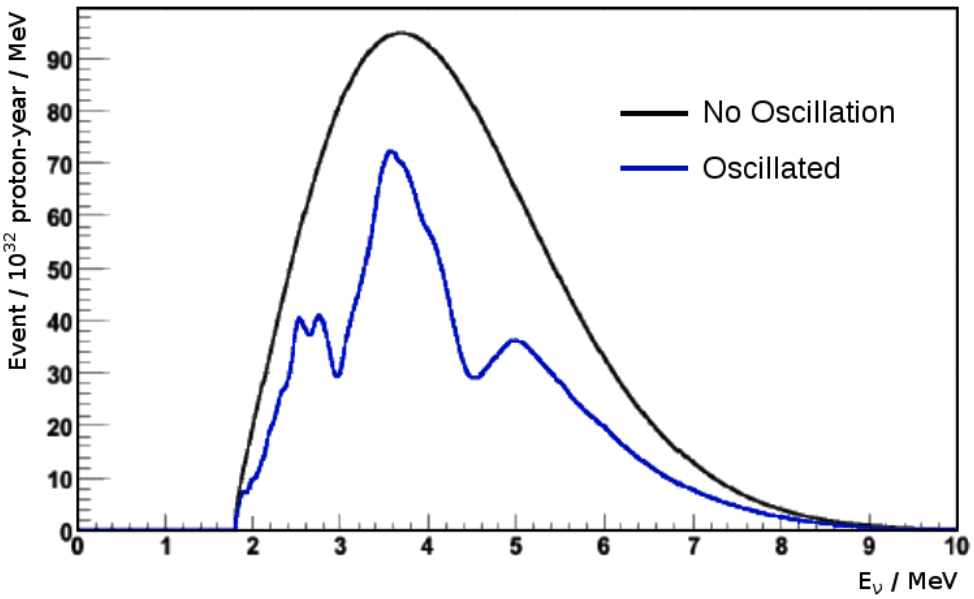


Figure 3.6: Expected nuclear reactor anti-neutrino spectrum multiplied by the inverse beta decay spectrum. [38]

### 3.2.4 Geo-Neutrinos

Anti-neutrinos are not only exclusive to nuclear reactors but can also be released through radioactive isotopes in the Earth's mantle and crust. In particular are anti-neutrinos from isotopes from the decay chains of $^{238}$U and $^{232}$Th, see Figure 3.10 and Figure 3.11 respectively, and from $^{40}$K. These anti-neutrinos are known as geo-neutrinos. Geo-neutrinos are interesting because they can give insight on the amount of radioactivity present deep within the Earth. It is thought this energy is responsible for an unknown fraction (50%-100%) of the heat production inside the Earth. Furthermore, measuring this radioactivity will give insight on how the interior of the Earth has cooled over time and how it might play out in the future [39].

SNO+ will not be the first to measure geo-neutrinos as they were measured by the KamLAND experiment as well [40]. SNO+ benefits over KamLAND by being situated in the Canadian Shield, were the continental crust has a higher concentration of radioactive elements over the oceanic crust around Japan.

Similar to reactor neutrinos, the anti-neutrinos can be easily distinguished from back-

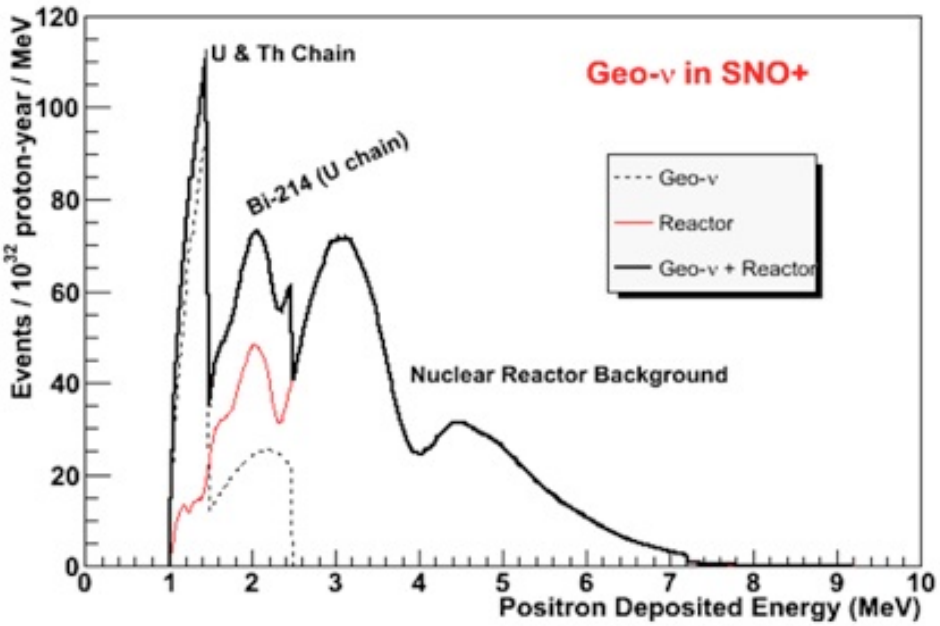


Figure 3.7: Expected geo-neutrino signal in SNO+ [38]. The geo-neutrinos are more clearly defined from the reactor anti-neutrinos at lower energies.

ground events through inverse beta decay, Equation 3.1. The only significant background to geo-neutrinos is the overlap of the reactor anti-neutrinos, see Figure 3.7, but with precise knowledge of the reactor anti-neutrino flux the geo-neutrinos signal should be easily identified.

### 3.2.5 Supernova Neutrinos

Neutrinos can also be observed when a massive star has spent all its nuclear fuel and undergoes a supernova explosion. When a star's core mass exceeds around 1.4 solar masses, known as the Chandrasekhar limit, the outer part of the core undergoes rapid contraction. This is known as a type II supernova. The gravitational collapse releases a vast amount of energy, but because only weakly interacting particles can easily escape the core in a couple of seconds, more than 99% of the binding energy is carried away by neutrinos [41].

The neutrino burst emits more neutrinos in the span of a few seconds than in the total lifespan of the star. The neutrinos are predicted to be evenly divided by flavours and between particles/anti-particles. The expected average energy of the neutrinos is around

| (Anti)Neutrino Interaction | Expected Events |
|---|---|
| $\nu_e + e^- \rightarrow \nu_e + e^-$ | 8 |
| $\bar{\nu}_e + e^- \rightarrow \bar{\nu}_e + e^-$ | 3 |
| $\nu_{\mu,\tau} + e^- \rightarrow \nu_{\mu,\tau} + e^-$ | 4 |
| $\bar{\nu}_{\mu,\tau} + e^- \rightarrow \bar{\nu}_{\mu,\tau} + e^-$ | 2 |
| $\bar{\nu}_e + p \rightarrow n + e^+$ | 263 |
| $\nu_e + {}^{12}\mathrm{C} \rightarrow {}^{12}\mathrm{N} + e^-$ | 27 |
| $\bar{\nu}_e + {}^{12}\mathrm{C} \rightarrow {}^{12}\mathrm{B} + e^+$ | 7 |
| $\nu_x + {}^{12}\mathrm{C} \rightarrow {}^{12}\mathrm{C}^* + \nu_x$ | 58 |
| $\nu_x + p \rightarrow \nu_x + p$ | 273* |

Table 3.1: Expected number of neutrino events from a $3 \times 10^{53}$ $erg$ supernova originating 10 $kpc$ away and assuming neutrino-matter oscillations (* Assuming 0.2 MeV threshold for proton scattering) [43].

15 $MeV$ [42]. So large is this neutrino flux that even at Galactic distances a large number of events will be detected in SNO+.

Because SNO+ is a large volume scintillator experiment, SNO+ will also make a good supernova detector. The different types of interactions coming from supernova neutrinos, along with their expected number of detected events from a "standard" supernova 10 $kpc$ away, are listed in Table 3.1. This distance is as a good approximation for a potential supernova due to the fact that the distance from Earth to the Galactic centre is 8.33 $\pm 0.35$ $kpc$ [44]. Detection of a Galactic supernova by SNO+ would have good statistics and would provide some ability to distinguish between different neutrino flavours. This flavour separation is expected to provide even more information about supernova physics and neutrino oscillations.

## 3.3 Background Requirements

Neutrinoless double beta decay is a rare process, therefore ideally SNO+ should be "background free" in the $0\nu\beta\beta$ region. This however, is not the case. The amount of backgrounds that are expected after two years of data have been simulated and are represented in Figure

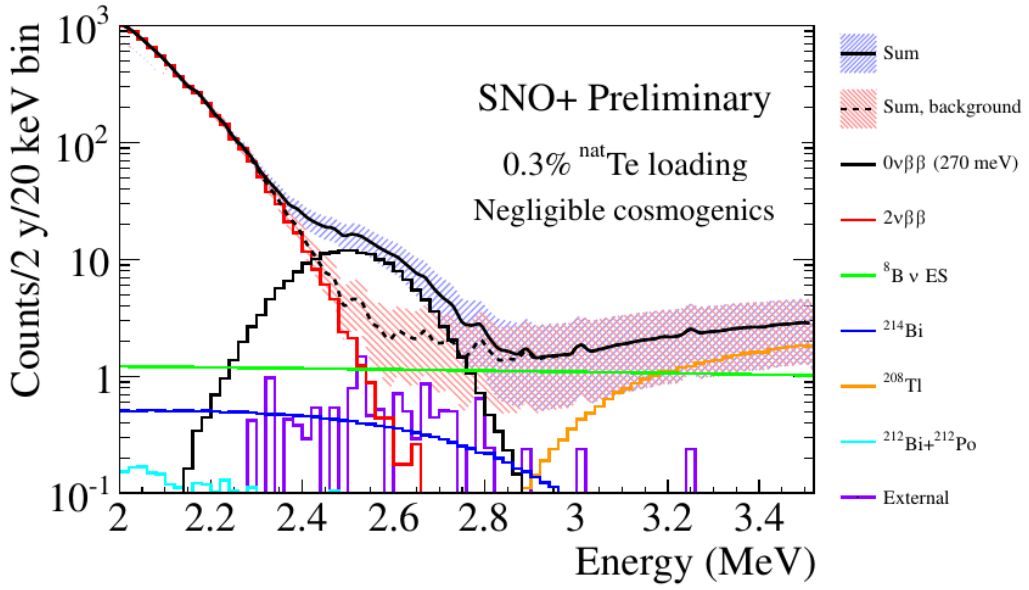


Figure 3.8: Energy spectrum of $0\nu\beta\beta$ signal and expected backgrounds for $^{130}$Te after two years of data taking [45].

3.8. Some of these backgrounds are unavoidable, such as the $2\nu\beta\beta$ spectrum.

Another inescapable background, which is expected to be the largest contributor comes from the $^{8}$B neutrino flux. These $^{8}$B neutrinos were also the primary signal in SNO and are visible in scintillator through elastic scattering. Fortunately, the $^{8}$B neutrino flux can be constrained by the measurements that were taken by SNO.

The majority of radioactive backgrounds from within the scintillator itself come from the decay chains of $^{238}$U and $^{232}$Th, shown in Figure 3.10 and Figure 3.11 respectively. Near the end of the decay chain of Uranium 238 is $^{214}$Bi, which decays by beta and gamma emission with a $Q$-value of 3.27 MeV. This results in an energy range that overlaps with the $0\nu\beta\beta$ region. However, these events can be reduced by 99.99% from the $^{214}$Bi - $^{214}$Po $\beta$-$\alpha$ time coincidence [46].

From the Thorium 232 decay chain there are backgrounds from both $^{208}$Tl and from $^{212}$Bi decaying into $^{212}$Po. $^{208}$Tl beta decays into excited states of $^{208}$Po. $^{208}$Po then decays into the ground state by an emission of a 2.614 MeV gamma. Subsequently $^{208}$Tl has a $Q$-value of 4.99 MeV which also interferes with the $0\nu\beta\beta$ region. These events can also be reduced by 97% from $\alpha$ tagging of $^{212}$Bi to $^{208}$Tl [47].

| Isotope | Borexino Level ($g/g$) |
|---|---|
| $^{238}$U | $1.60 \times 10^{-17}$ |
| $^{232}$Th | $6.80 \times 10^{-18}$ |

Table 3.2: Target radiopurity levels in scintillator taken from Borexino [48] in grams of isotope per gram of LAB.

Beta decay from $^{212}$Bi has an energy spectrum endpoint of 2.25 MeV, whereas $^{212}$Po emits a single alpha at 8.785 MeV. The reason that $^{212}$Bi decaying into $^{212}$Po is a background concern comes from the quenching factor in the scintillator. The $^{212}$Po alpha loses energy through multiple Coulomb scattering and ionization resulting in only around 0.9 MeV seen in the detector. That coupled with the relatively short half-life of $^{212}$Po (300 ns), falling into the SNO+ trigger window of 440 ns, means that the detector would see the two decays as one event. This observed energy potentially overlaps with the $0\nu\beta\beta$ energy region. Likewise, these events can be tagged and reduced with an expected 94% efficiency [49]. With additional study these tagging values can be improved on in the future.

These simulated backgrounds all come from the assumption of reduced $^{238}$U and $^{232}$Th levels from proper cleaning and purification procedures. The target levels of radiopurity for the scintillator in SNO+ have been established to accomplish, if not improve on, background levels that were measured in the Borexino experiment [48]. This is because, to date, Borexino has the most sensitive measurements of radioactivity in a comparable scintillator detector. These background levels are summarized in Table 3.2.

External backgrounds are classified as sources of radioactivity that occur outside the of the scintillator. These include, but are not limited to, the acrylic vessel, the surrounding water shielding, and the photomultiplier tubes. The majority of external backgrounds are due to $^{208}$Tl and $^{214}$Bi, where the gammas produced are the biggest concern since they can travel much farther than the other decay products. These external backgrounds are reduced by limiting the fiducial volume of the detector to 3.5 meters, which is 20% of the total fiducial volume [50].

During the solar phase of SNO+ one of the biggest sources of background comes from radon, or to be precise from $^{210}$Bi the daughter of $^{222}$Rn. $^{210}$Bi has an endpoint point energy

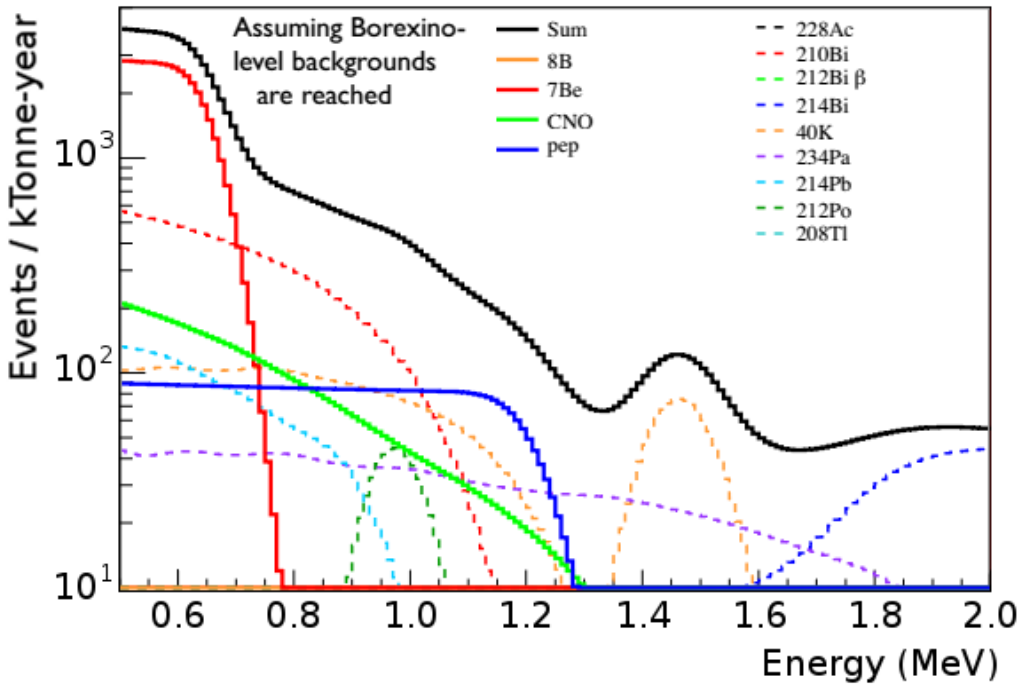


Figure 3.9: Expected backgrounds during the solar phase of SNO+ [51].

of 1.16 MeV and overlaps the *pep* and CNO energy regions, as seen in Figure 3.9. The real problem comes from $^{222}$Rn decaying on the surface of the acrylic vessel and embedding from alpha decays. The decay daughters of radon all have relatively short half lives with the exception of $^{210}$Pb, which has a half life of 22.26 years, which then directly beta decays into $^{210}$Bi.

While transitioning from SNO to SNO+ the acrylic vessel has been exposed to air for years, this accounts for a large amount of lead in the acrylic itself. Not only that, but because SNO+ is located in an active mine, rock blasting increases the natural amount of $^{222}$Rn in the air, which averages to 131.0 $\pm$ 6.7 $Bq/m^3$ [52]. To reach the levels of background achieved by Borexino much work needs to be done to ensure the removal of $^{210}$Pb from the acrylic and to prevent additional radon into the detector. One of the ways to constraining radon ingress into the detector is by having a sealed system which will be described further in the next Chapter (see Chapter 4.3).

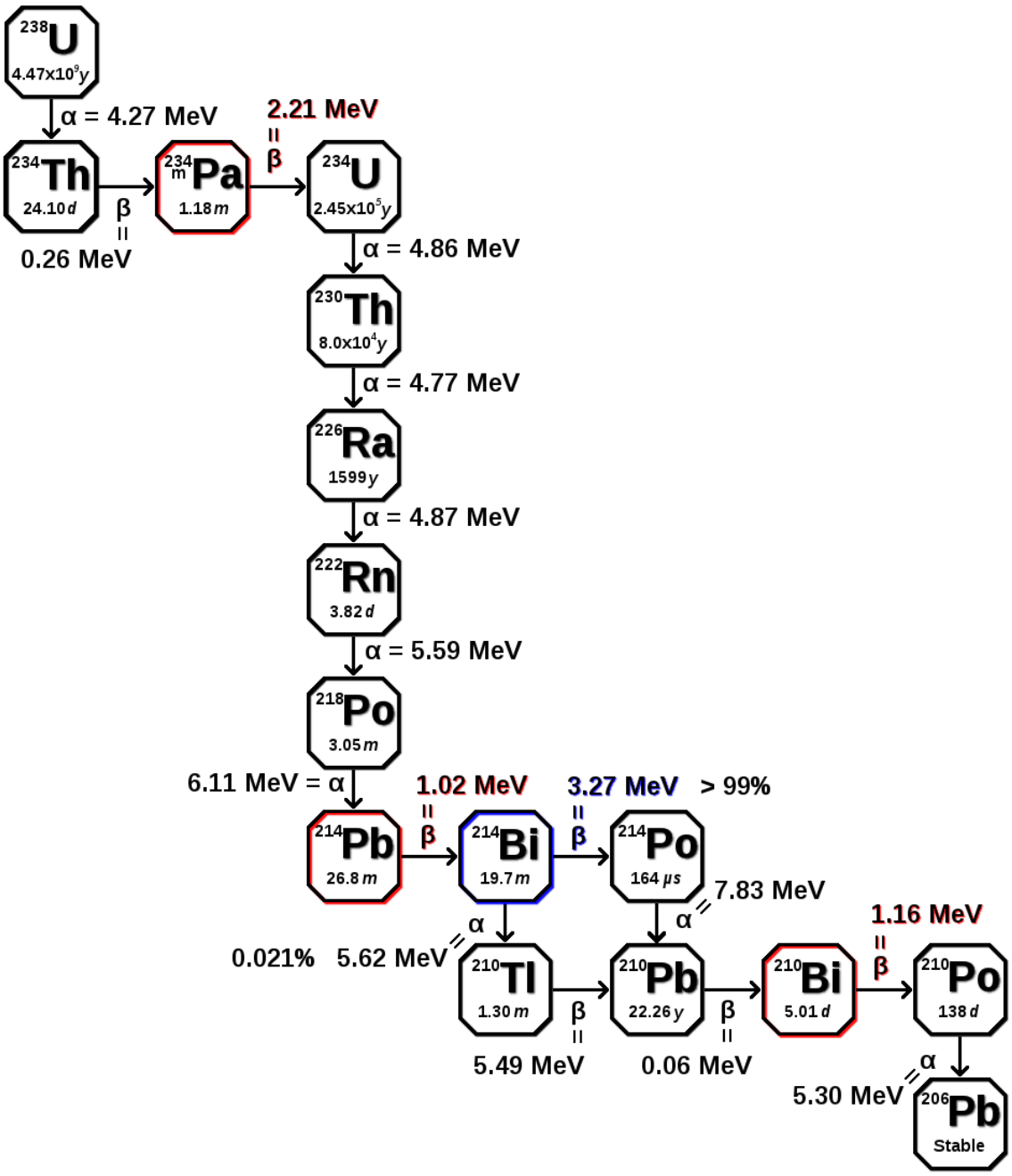


Figure 3.10: Uranium 238 decay chain. Isotopes that are a background for double beta phase are highlighted in blue while backgrounds for solar phase are highlighted in red.

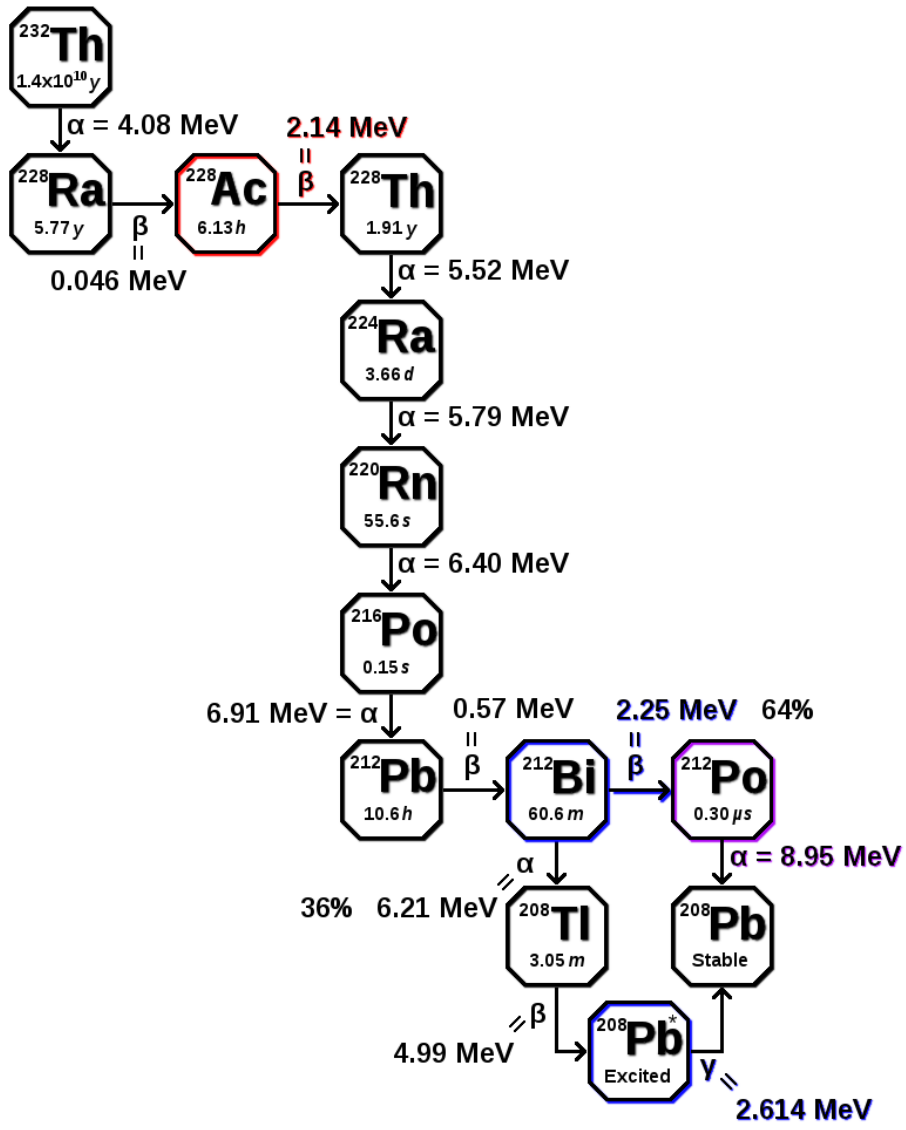


Figure 3.11: Thorium 232 decay chain. Isotopes that are a background for double beta phase are highlighted in blue while backgrounds for solar phase are highlighted in red. $^{212}$Po, which is a background for both phases, is highlighted in purple.

# Chapter 4: Calibration

Calibration is an important process for any high precision measuring device. Because SNO+ is indeed a very complex light measuring device, calibration must be at a sufficient frequency to insure that data collected is well understood. This is accomplished by deploying different calibration sources, i.e. well known devices, in order to understand the detector. For each calibration source there will be a specific parameter of the detector to investigate, with some overlap of parameters between sources. These parameters include electronic response, optical response, and energy response.

## 4.1 Deployment of a Calibration Source

This section will go over the basics of deploying a calibration source into the detector volume. Knowing how a source is deployed in SNO+ will assist in understanding the importance of the different hardware that will be discussed further in this Chapter and in Chapter 6.

To enter the detector calibration sources must be first connected to the "umbilical" and placed inside the umbilical retrieval mechanism (URM). The umbilical is the cable that houses all the wiring necessary for the calibration source to operate. The URM is then connected to the universal interface (UI). The URM and UI are both isolated from the labratory air with their own set of gate valves and once attached the air between gate valves is purged to minimize contamination.

Next, the calibration source is lowered into the UI by the URM. While inside the UI, additional side motor ropes are attached to the calibration source by an individual wearing a pair of gloves. Not all side ropes are reachable from one set of gloves so there are additional

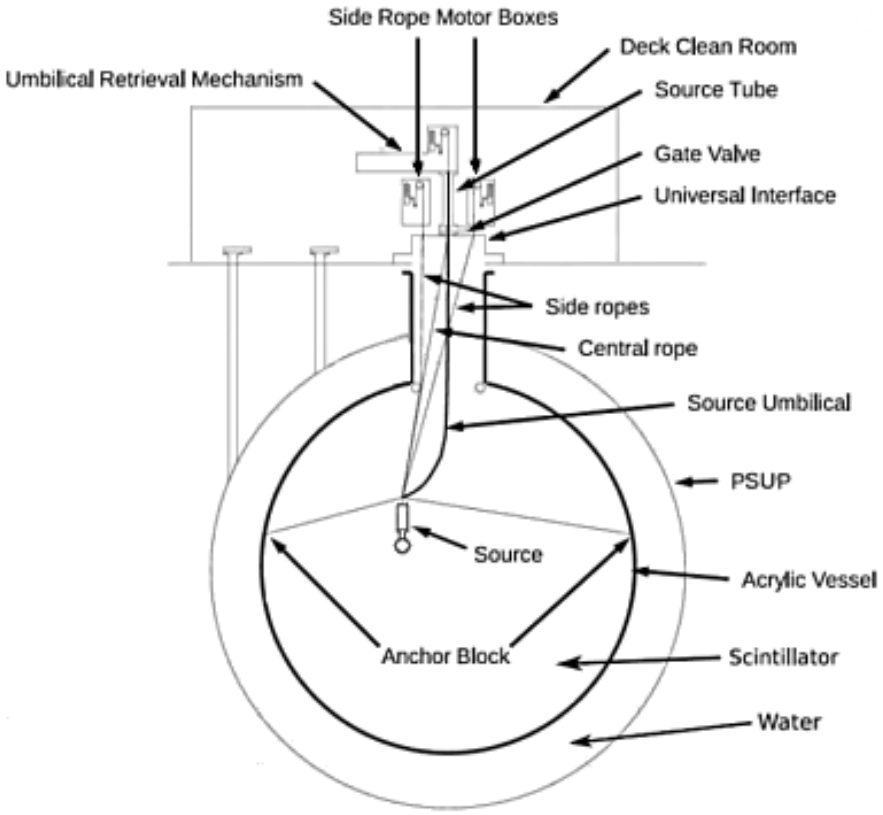


Figure 4.1: Calibration source deployment into the detector. The source is moved off to the side by use of the side ropes, while the Umbilical Retrieval Mechanism (URM) is used to control the vertical positioning.

pairs of gloves that another individual can use to help expedite the process. Once the side ropes are attached the calibration source is ready to be deployed.

The URM is then used to lower the source to the appropriate vertical position, while the side ropes are used to move the source in the horizontal plane. An image of a deployed calibration source is shown in Figure 4.1. To ensure exact position placement each motor on the URM and side ropes also have encoders to track source position.

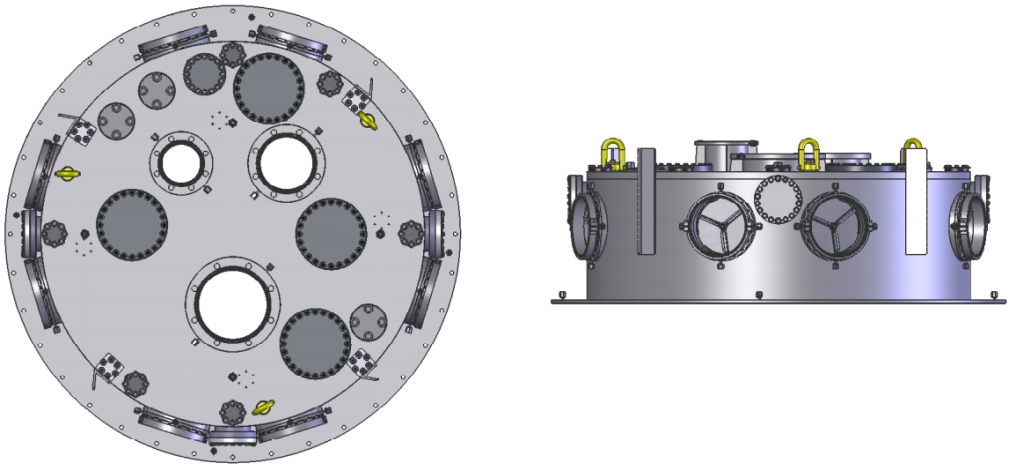

Figure 4.2: Top view of the upper universal interface on the left, with a side view of the upper universal interface on the right.

## 4.2 Calibration Hardware

### 4.2.1 Universal Interface

The universal interface (UI) is the supporting stainless steel structure that rests on top of the acrylic vessel (AV). The UI is designated into two different parts; the lower UI and upper UI. The lower UI provides the seal between the AV and the steel of the UI using a double o-ring configuration. The lower UI is also the attachment point for pipes used to move liquid in and out of the AV. Furthermore a flexible membrane, known as the "sliding floor", is attached to the lower UI which allows for the AV to move horizontally up to six inches in each direction.

The upper UI, see Figure 4.2, is the where the human interface to the detector is located. On the top of the UI are three gate valve ports, which allow for calibration sources to enter the detector volume through the umbilical retrieval mechanism (URM). To access the source four pairs of glove ports are arranged around the UI, each with an acrylic window, known as a view port, where a user of the gloves can view into the UI. Furthermore the side rope manipulators are also housed on top of the UI.

Furthermore, located on the upper UI will be 4 PMTs, known as neck PMTs. These will be used to collect signals that travel from the AV up through the neck or even events created

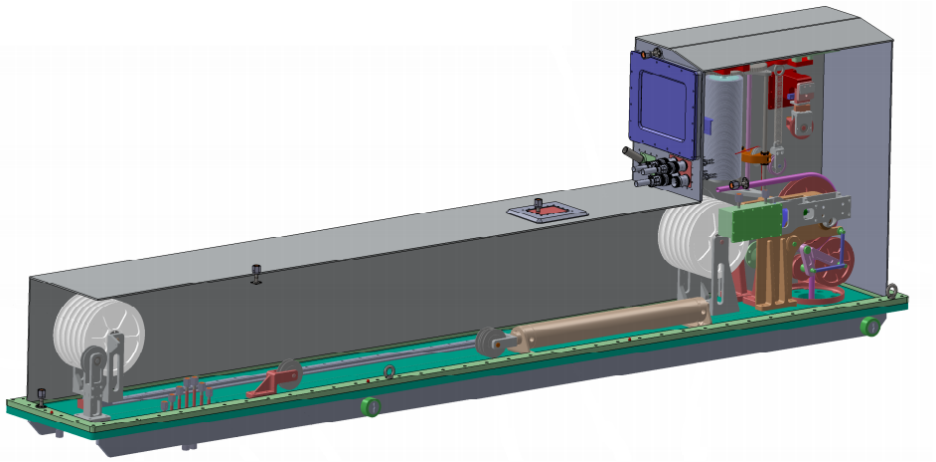

Figure 4.3: A view of the inner pulley system of the umbilical retrieval mechanism

inside the neck. There will also be a high precision oxygen monitor to detect contamination in the pure nitrogen gas inside the UI, referred to as the cover gas. In addition, there will be a pressure transducer to determine the pressure difference between inside/outside the UI. Lists of these different instrumentation for the UI and other parts of the calibration system are organized into tables found in Appendix B.

### 4.2.2 Umbilical Retrieval Mechanism

The umbilical retrieval mechanism (URM) is the work horse of the calibration system. It houses the umbilical, a clear flex filled tygothane cable that holds electrical, fiber optic, or gas line as needed for a calibration source. The URM moves the calibration source vertically while inside the detector.

The URM also acts as the transfer mechanism between getting a source from the source storage box and placing it in the detector. The URM also incorporates a long stainless steel cylinder which can house the source while it is being moved. The source is then isolated from the surrounding lab air by a gate valve.

### 4.2.3 Gate Valves

Gate valves, see Figure 4.4, control access to anything that goes into the detector. There are three sizes of gate valves on top of the UI, 6” diameter port, 8” diameter port and 10”

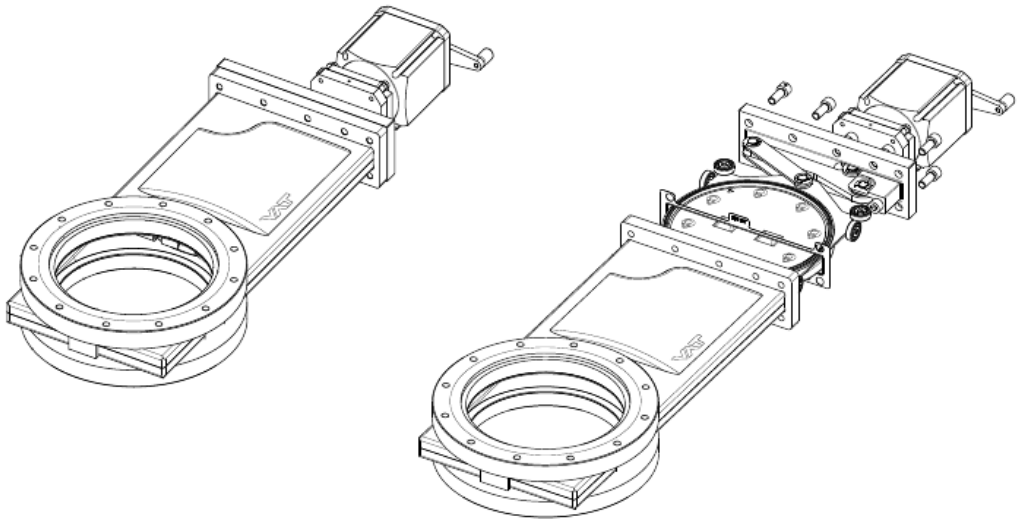

Figure 4.4: Potential 10" gate valve in the left with disassembled view of the inner structure of the gate valve on the right. A key feature in the disassembled view is the hinged moving arm that is used for position sensing.

diameter port. For each gate valve on the UI there will be a corresponding gate valve on the URMs. Similarly, there will be corresponding gate valves on the source storage box. Whenever a pair of gate valves are connected the space between them must be purged with cover gas quality air, see Chapter 4.3, to reduce any contamination to the detector.

Also installed on the gate valves are position sensors to indicate whether the gate valve is open/closed. Part of my work was to determine the appropriate sensors to use as position indicators. One idea was to mount inductive sensors that would detect an iron disc mounted on the hinged moving arm of the gate valves. However an easier solution came about as the manufacturer that designs the gate valves has an option for pre-installed microswitch sensors. These micro switches work in a similar fashion in that they detect the open/closed position based on the position of the hinged moving arm.

This information is important to know because if the gate valve is open then it is easy to assume that a calibration source is deployed. Therefore anyone remotely connecting to the detector will be aware if a calibration source is running and won't falsely record the data as physics data. It can also be used to determine when calibration sources where used and for how long by logging the sensor information in a database.

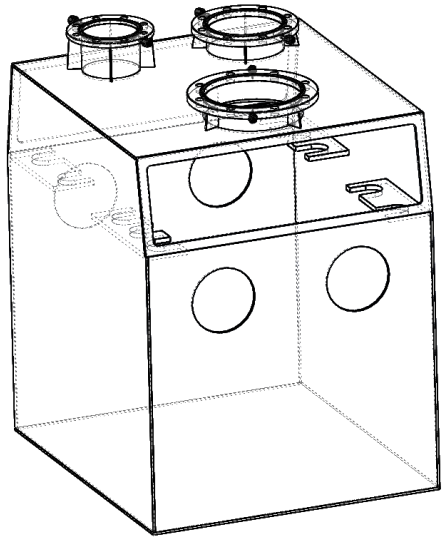

Figure 4.5: The Source Storage Box where calibrations sources that can be kept underground for long periods of time can be stored.

### 4.2.4 Side Rope Manipulator

The side rope manipulator, is the device that controls the side ropes, which are seen in Figure 4.1. The side ropes are important because they allow movement in the vertical plane for any calibration source that enters the scintillator volume. These ropes are attached at anchor points at the equator of the AV. By pulling on a single side rope the source is moved to the anchor point of the respective rope. By adjusting these ropes, sources can be moved around in a majority of the detector volume.

There are four side rope manipulators with each manipulator containing two parts, the motor box and the load cell box. The motor box drives the side ropes and stores the excess rope. The load cell box incorporates an encoder to measure the amount of rope movement and a load cell to monitor the tension in the rope. These are also used in determining horizontal and vertical position of sources inside the detector.

### 4.2.5 Source Storage Box

Calibration sources that can spend a long time underground will be housed in the source storage box, see Figure 4.5. The benefit of the storage box is that it can be kept in a low background environment, either submerged in scintillator or immersed in cover gas. This

will prevent radioactive surface contamination, especially from radon daughters, and reduce potential backgrounds from introducing calibration sources in the detector.

The source storage box will work similarly to the UI with its own set of gate valves and gloves. A quick connect device will also be used to ease the process of attaching the sources to the umbilical while wearing gloves.

## 4.3 Cover Gas System

One problem that occurs from having the SNO+ experiment in an active mine comes from the increased $^{238}$U and $^{232}$Th backgrounds from exposure of rock. This leads to an increased rate of $^{222}$Rn found in the air, which is measured to amount to $131.0 \pm 6.7\ Bq/m^3$ around the detector [52]. $^{222}$Rn needs to be constrained because of the decay daughter $^{214}$Bi is a direct background for observing $0\nu2\beta\beta$, see Chapter 3.3. This is accomplished by using a sealed system and replacing the air volume with a gas which has low amounts of contamination from $^{222}$Rn, which is known as the cover gas.

The cover gas in SNO+ will use $N_2$ gas. Nitrogen is chosen because it is a highly pure inert gas. To increase the purity of the nitrogen gas, boil off from liquid nitrogen is used. Cylinders of nitrogen gas can be used, but because the cylinders can be easily contaminated at low pressure, boil off liquid nitrogen is preferred. The boil off gas has low radon contamination due to the fact that the boiling point of liquid nitrogen is -196 $^\circ C$, whereas liquid radon boils at -62 $^\circ C$. Therefore most of the unwanted radon would remain in the gas cylinder, leaving the boil off gas extremely pure.

To handle the pressure fluctuations in the mine, three 240 $L$ aluminum flexible bags are also incorporated into the cover gas system. The maximum pressure fluctuation was measured to be 8 $kPa$ from data taken in 2006 over a four month period [53], with a maximum pressure change rate of 15.94 $Pa/s$ [54]. In case a large swing in pressure occurs an emergency U-trap system is also installed into the cover gas system.

| Source | Radon Atoms per Day |
|---|---|
| Universal Interface O-Ring Seal | ∼250 |
| Cover Gas Bags - Emanation | 228 ±83 |
| Cover Gas Bags - Permeation | <36 |
| Gloves - Emanation | 102 |
| Gloves - Permeation | ∼3000 |

Table 4.1: Contribution of radon inside the cover gas [55]. The amount from gloves were taken simulated in Chapter 6 for butyl rubber gloves left in the cover gas volume 24 hours a day.

### 4.3.1 Cover Gas Radon Requirements

The amount of radon allowed into the cover gas is based on the achieved $^{238}$U rates seen in Borexino, see Table 3.2. This corresponds to 4897 radon decays per year, 13.4 decays per day, in the scintillator. Assuming there is a factor of 50 reduction of radon from stagnation and decays in the cover gas to radon that mixes with the scintillator, the target level of radon in the cover gas is set to 670 decays per day [56]. The main contributors of radon contamination are shown in Table 4.1.

# Chapter 5: Laserball Simulations

The "laserball" is one of many optical calibration sources that can be deployed in the detector. The laserball consists of a light diffusing quartz flask illuminated through optical fibres by a $N_2$ Transversely Excited Atmosphere (TEA) thyratron triggered ultraviolet pump laser. This laser system, which produces 600 $ps$ pulses at a wavelength of 337.1 $nm$, can be used to pump one of five laser dyes, whose properties are summarized in Table 5.1.

## 5.1 Laserball Generator

In SNO+ the simulation software used to simulate the detector is known as RAT. In RAT for each calibration source is a generator file which produces the expected signal from the respective source. However for the laserball, the generator file can only produce single wavelengths. This is problematic because lasers are known to produce distributions of wavelengths, for example a homogeneously broadened laser produces a Lorentzian-shaped emission spectrum.

To generate photon wavelengths based on a certain dye's properties, first of all the wave-

| Laser Dye | Peak Wavelength [$nm$] |
|---|---|
| PPO | 380 |
| PBBO | 396 |
| bis-MSB | 421 |
| Coumarin-440 | 439 |
| Coumarin-481 | 490 |

Table 5.1: Laser dyes used in the dye laser for the laserball optical calibration source.

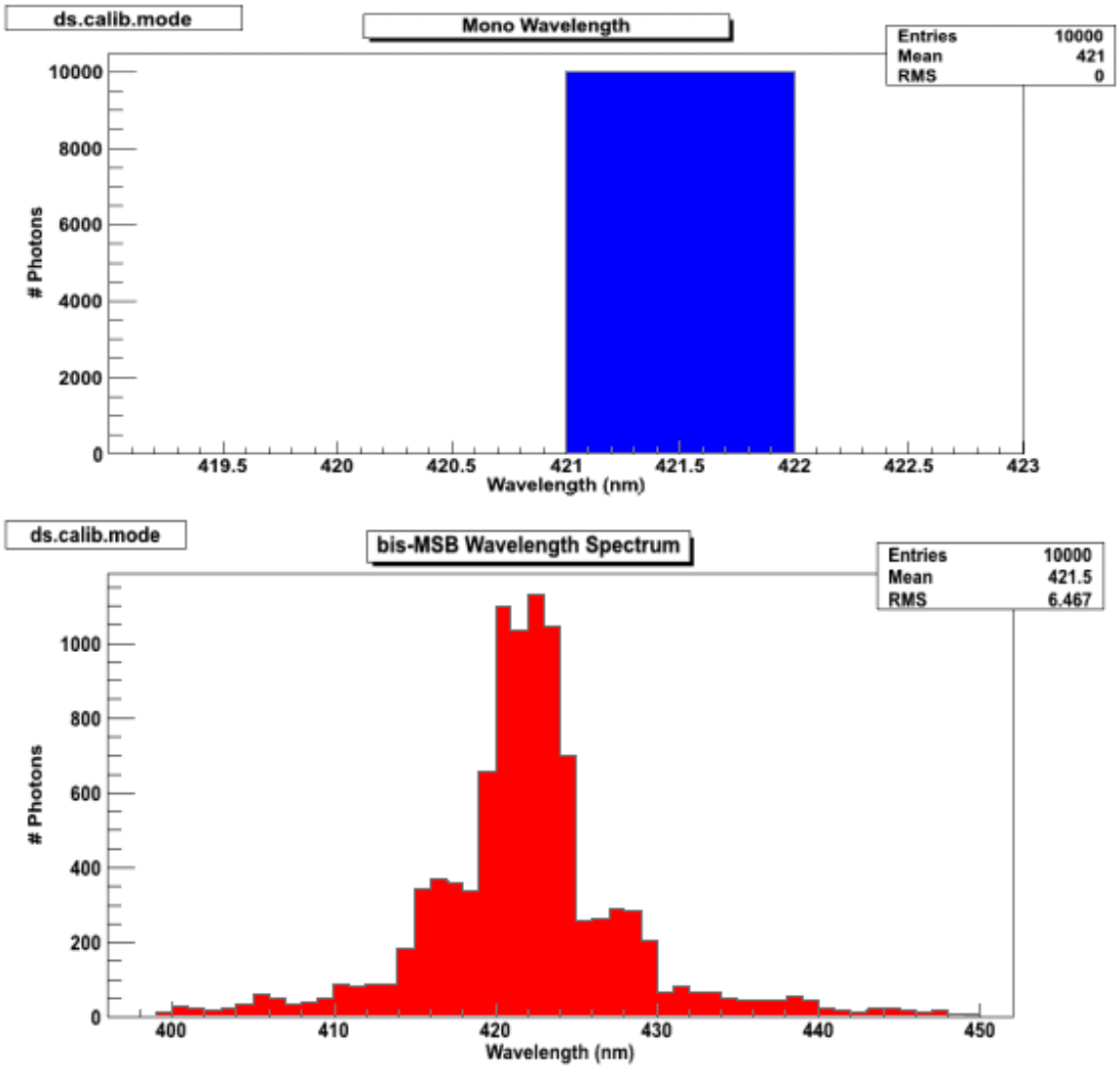


Figure 5.1: The top figure shows how the old laserball generator worked for 421 *nm*. On the bottom the new laserball generator is used to generate a distribution of light similar to seen with the bis-MSB laser dye.

length spectrum is pulled from the laserball database. Then a new distribution, known as the cumulative magnitude distribution, is created from the wavelength spectrum by adding the magnitude of all the previous wavelengths for all wavelengths in the spectrum. By randomizing between zero and the maximum value of the cumulative magnitude distribution and then translating to wavelength in that region then randomized photons will reproduce the chosen laser dye's wavelength spectrum. Figure 5.1 demonstrates the difference between the old laserball generator (top) and the using the new distribution functionality (bottom).

## 5.2 Non-direct light contribution from laserball simulations

One of the problems the calibration group runs into comes from non-direct light from absorption/re-emission and Rayleigh scattering in the scintillator. This "late" light adds additional complexity to the analysis of calibration data and so it would be ideal to minimize its contribution. One way of accomplishing this is by introducing an asymmetric cut on the prompt light peak of the time signal, as opposed to the symmetric time profile of $\pm 4$ $ns$ on the prompt peak that was used in SNO. A problem that comes with introducing this asymmetric time profile is that the prompt light signal will also be affected, therefore the two parameters of contribution of non-direct light and the reduction of prompt light need to be optimized.

The time signal is the measurement of the light collected by the photomultiplier tubes (PMTs) during a physics event, or by a calibration source. Figure 5.2 shows what a time signal would look like coming from the centre of the detector. The light that comes directly from the source is known as the prompt peak. There are also some interesting features seen in this time signal which occur from effects in the PMTs and from the detector.

The pre-pulsing comes from photons that bypass the photocathode and that produce an electron in the dynode. The typical signal seen in the PMTs, for example the prompt peak, comes from electrons that are created by photon absorption in the photocathode which are then collected on the dynode by an electric field. This difference between electron drift and direct photon collection accounts for the time separation of the two features. Late pulsing

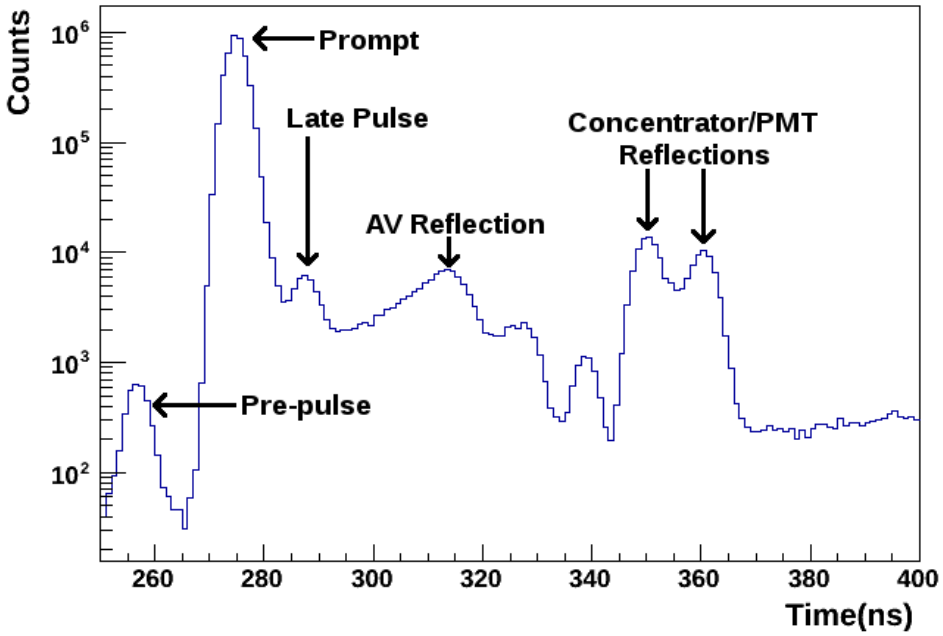


Figure 5.2: Time profile of an event occurring the in centre of the detector for SNO+.

comes from optical feedback inside the PMT which can create additional electrons on the photocathode. The other features in the time signal come from reflection of light in the detector from the acrylic vessel itself, the PMTs, and the light concentrator panels that surround the PMTs.

To compare the effects of scattering and absorption/re-emission in the scintillator, four different simulations were done for each laser dye. The first simulation disallowed scattering and absorption/re-emission processes in order to determine the ideal prompt peak. Then each process was simulated separately to see the contribution of each effect individually, and finally both effects were simulated to observe the total contribution of non direct light. These simulations were also placed in selected positions in the detector. The positions are referenced from the centre of the detector by the (x, y, z) positions and the laserball runs are done at positions (0, 0, 0) the centre of the detector, (-1.9 $m$, 0, -4.6 $m$), (-2.3 $m$, 0, -2.3 $m$), and (-1.5 $m$, 0, -1.5 $m$).

Figure 5.3 shows the contributions of the different physics effects for PPO dye (380 $nm$ peak wavelength) with the laserball positioned in the centre of the detector. The major contribution of non-direct light comes from the absorption and re-emission of light in the

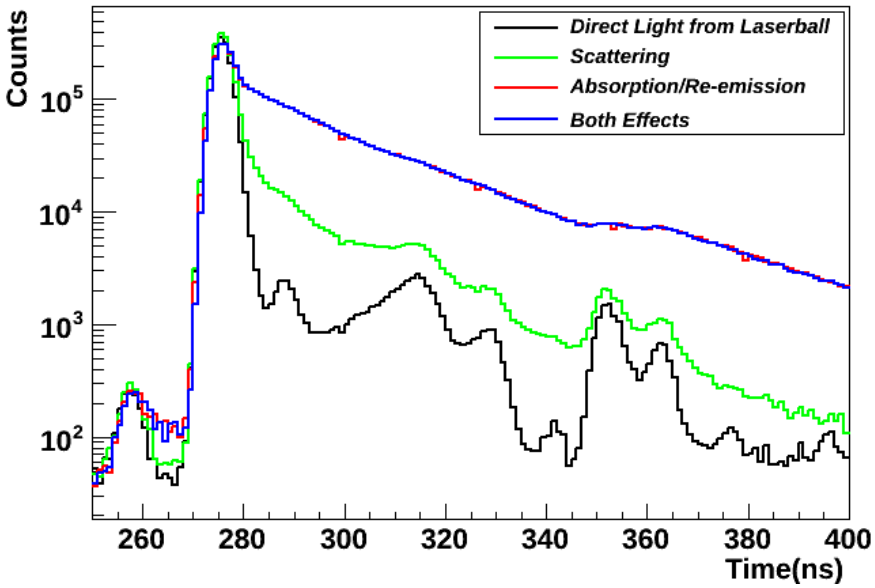


Figure 5.3: The contributions of non-direct light come from scattering, absorption/re-emission and both scattering and absorption/re-emission compared to direct light for the laserball running at 380 $nm$ in the centre of the detector.

scintillator. Scattering also has a significant contribution by itself but when considering both sources of non-direct light the absorption/re-emission dominates the process.

By subtracting the direct light from the different simulations, the contribution of non-direct light can be determined. Figure 5.4 demonstrates the amount of non-direct light from the scattering only profile. There is a large contribution of non-direct light after the prompt peak, however the features in the time profile can still be distinguished.

In Figure 5.5 the effects non-direct light from the effects of absorption and re-emission are observed. In this case there is significant non-direct light after the prompt peak that washes out all the distinct features seen the direct light time profile.

In Figure 5.6 the contribution of non-direct light from both scattering and absorption/re-emission is seen. The time profile is similar to Figure 5.5 and thus the major contribution of non-direct light comes from the absorption and re-emission process.

From here the different time profiles are placed around the prompt peak, which for the laser running with PPO dye in the centre of the detector is located at 275 $ns$. Because the majority of non-direct light comes after the prompt peak, the different time profiles are

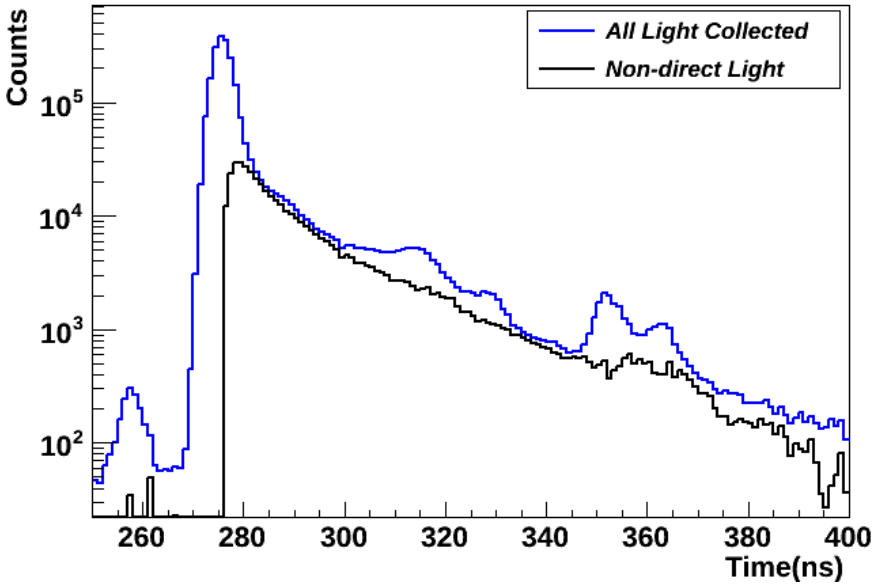


Figure 5.4: The effects of scattering with absorption/re-emission turned off and the laserball running at 380 $nm$ in the centre of the detector.

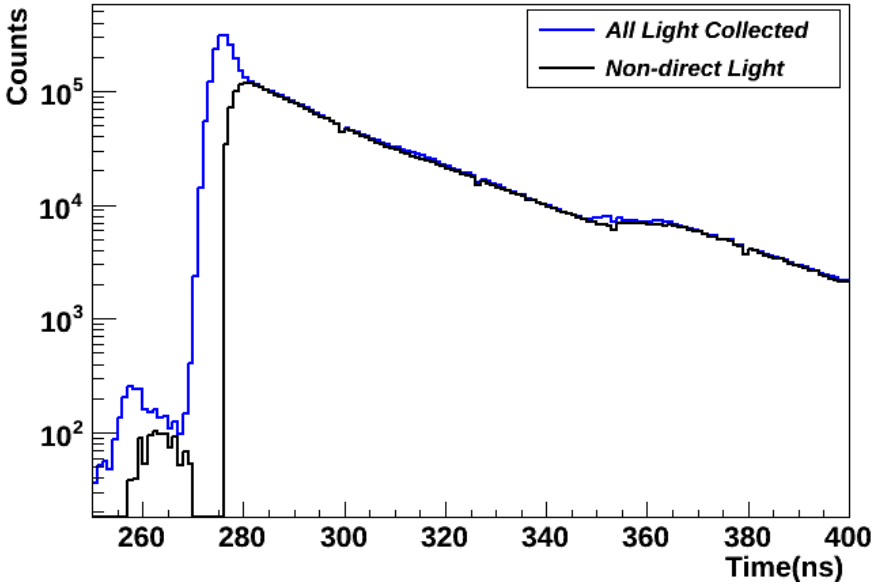


Figure 5.5: The effects of absorption/re-emission with scattering turned off and the laserball running at 380 $nm$ in the centre of the detector.

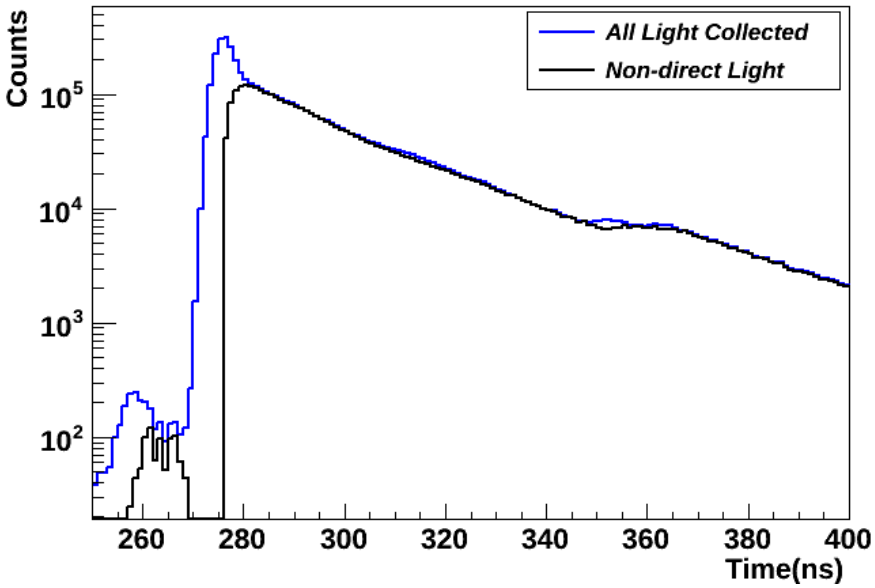


Figure 5.6: The effects of both scattering and absorption/re-emission with the laser running at 380 $nm$ in the centre of the detector.

selected as $\pm 4$ $ns$, $^{+3}_{-4}$ $ns$, and $^{+2}_{-4}$ $ns$. These values are recorded in Table 5.2 for all laser dyes and with the laserball being positioned in the centre of the detector. Furthermore, the reduction of prompt light from going the typical $\pm 4$ $ns$ time profile to an $^{+3}_{-4}$ $ns$ or $^{+2}_{-4}$ $ns$ asymmetric time profile is also included in the table. This is important to consider as well because if too much prompt light is cut then there is a reduction in the data that is wanted for analysis.

In the $\pm 4$ $ns$ time profile off the prompt peak there is a contribution of 21.52% non-direct light for PPO dye in the centre of the detector from both scattering and absorption/re-emission. By implementing an $^{+3}_{-4}$ $ns$ asymmetric time profile there is a reduction by 26.86% of the non-direct light. However, this also leads to a reduction of 9.43% in the prompt light. By going even further to an $^{+2}_{-4}$ $ns$ asymmetric time profile the contribution of non-direct light is reduced by 54.88%. The reduction in prompt light is reduced by 21.54%. Comparing the ratio of reduction of non-direct light to reduction of prompt light it is clear that the most benefit comes from implementing the $^{+3}_{-4}$ $ns$.

## 5.3 Centre Laserball Simulations

Positioning the laserball, whose details can be found at the beginning of this Chapter, at the centre of the detector is important for simultaneously measuring the relative timing and gain (PCA) of the PMTs. The intensity of the laserball needs to adjusted so that the PMT signals collected are mostly from single photo electrons. Once the PCA calibration is completed, it can be monitored with an external LED driven system.

This system is known as the Timing Embedded LED Light Injection Entity (TELLIE) and consists of 92 wide aperture optical fibres that are mounted directly to the PMT support structure (PSUP) with one LED per fibre operating at 505 $nm$ wavelength. TELLIE is just one of three systems that uses optical fibres mounted on the PSUP for optical calibrations, which are referred to in general as the Embedded LED Light Injection Entity (ELLIE) system.

By increasing the intensity of the laserball the effect of occupancy, how many PMTs are hit, on the the timing and gain calibration can be studied. The laserball can also be used to measure the absorption length in both water and scintillator phase. By running through all the different laser dyes the timing profile compared to wavelength can also be measured.

The central run of PPO dye was discussed in Section 5.2, with the contributions of non-direct light show in Figure 5.3 and summarized in Table 5.2. For PPBO dye, with a 396 $nm$ peak wavelength, the contributions of non-direct light is shown in Figure 5.7. At the higher wavelength more features can be seen in the timing profile, where as now the reflection from PMT/Concentrators can be identified. This is a clear indication that there is a lesser effect from absorption/re-emission in the scintillator at 396 $nm$. There is also a slight increase from scattering at this wavelength.

In the "standard" $\pm 4$ $ns$ time profile of there is 11.40% non-direct light collected from the effects of both absorption/re-emission and scattering. Individually there is leads to a contribution of 9.36% from absorption/re-emission and 6.66% from scattering. By restricting the time profile to $^{+3}_{-4}$ $ns$ this non-direct light from both effects can be reduced to 8.44% and even further by a $^{+2}_{-4}$ $ns$ time profile to 5.29%. This is data summarized in

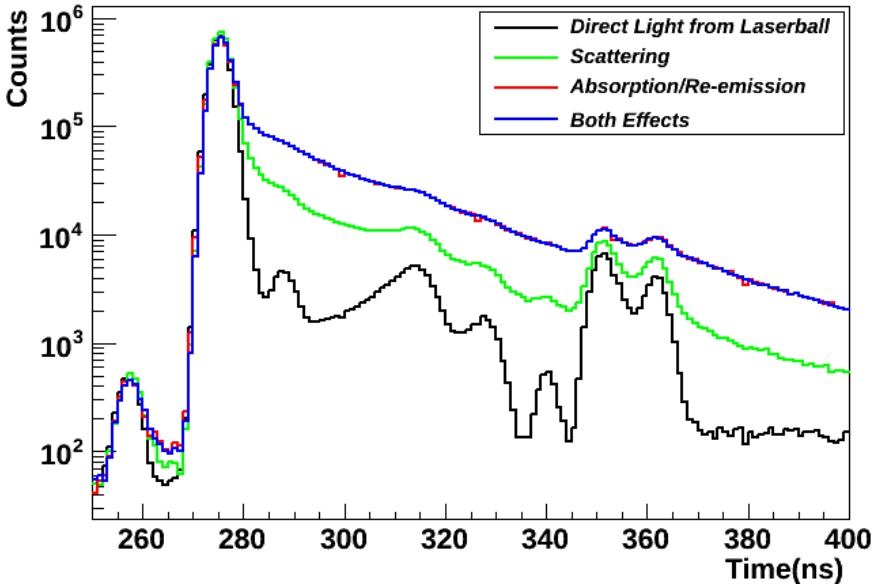


Figure 5.7: The different contributions of non-direct light for the laserball running at 396 $nm$ in the centre of the detector.

Table 5.2, along with the reduction prompt light by applying the different asymmetric time profiles.

Figure 5.8 shows the different contributions of non-direct light running with the bis-MSB laser dye, with a 421 $nm$ peak wavelength. At this higher wavelength even more features are seen in the timing profile even with non-direct light. This includes an increase in sharpness in the prompt light peak, and the reflection of the AV being discernable. There is a clear decrease in the effect of absorption/re-emission at 421 $nm$, however scattering does not seem to change much from 396 $nm$.

In the standard $\pm 4$ $ns$ time profile of there is 5.34% non-direct light collected from the effects of both absorption/re-emission and scattering. Individually there is leads to a contribution of 5.29% from absorption/re-emission and 3.63% from scattering. Already just by increasing the wavelength, the effects of non-direct light decrease faster than by implementing strict time cuts. However the amount of non-direct light can still be reduced by implementing the asymmetric time cuts. Using a $^{+3}_{-4}$ $ns$ and $^{+2}_{-4}$ $ns$ time profile the amount of non-direct light from both effects are reduced to 3.68% and 2.10% respectively.

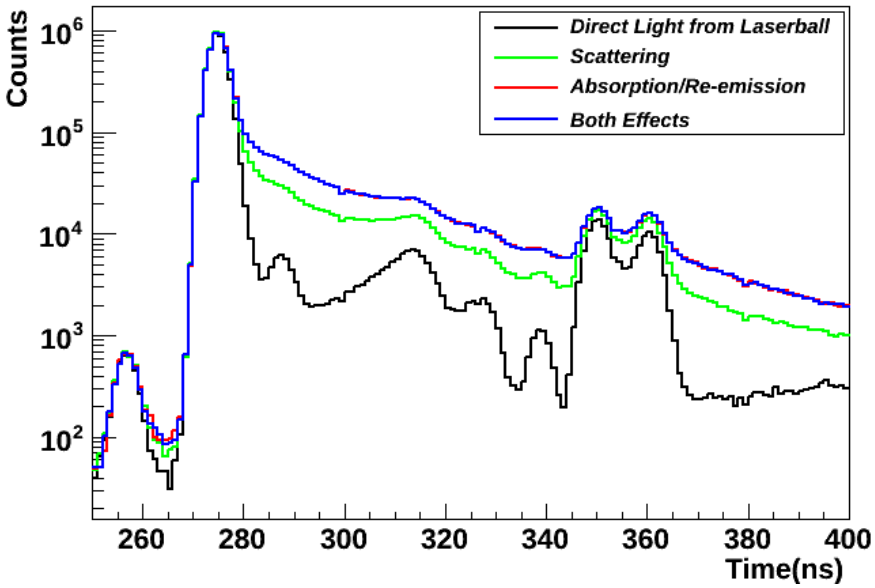


Figure 5.8: The different contributions of non-direct light for the laserball running at 421 $nm$ in the centre of the detector.

This is data summarized in Table 5.2, along with how the asymmetric time profiles reduces the amount of prompt light.

Figure 5.9 shows the contributions of non-direct light running with the Coumarin-440 laser dye, with a 439 $nm$ peak wavelength. Like with the previous simulations there is a reduction in the amount of non-direct light. However, it is not as significant as from the change of previous wavelengths.

This leads to 4.53% non-direct light seen from both absorption/re-emission and scattering in the standard time profile. The individual contributions from scattering/re-emission and scattering are 3.94% and 3.82% respectively. Now the asymmetric time cuts are less beneficial as there is less than a percent reduction in non-direct light contribution. From the $^{+3}_{-4}$ $ns$ time profile there is only 0.91% reduction from the standard time profile, leaving a contribution of 3.62% non-direct light. Likewise with a $^{+2}_{-4}$ $ns$ there is only 0.4% improvement from the previous time profile, leaving a contribution of 3.22% non-direct light. This information is summarized in Table 5.2, along with how the asymmetric time profiles reduces the amount of prompt light.

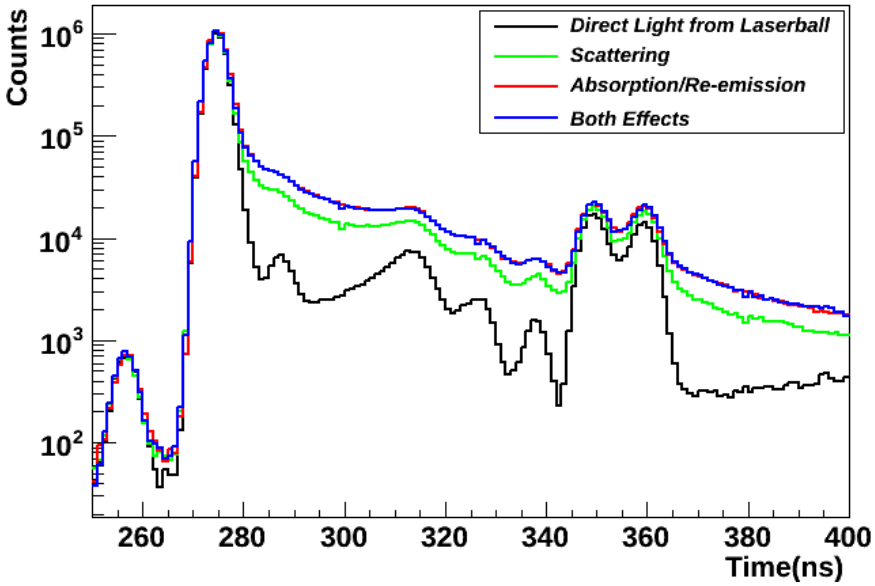


Figure 5.9: The different contributions of non-direct light for the laserball running at 439 $nm$ in the centre of the detector.

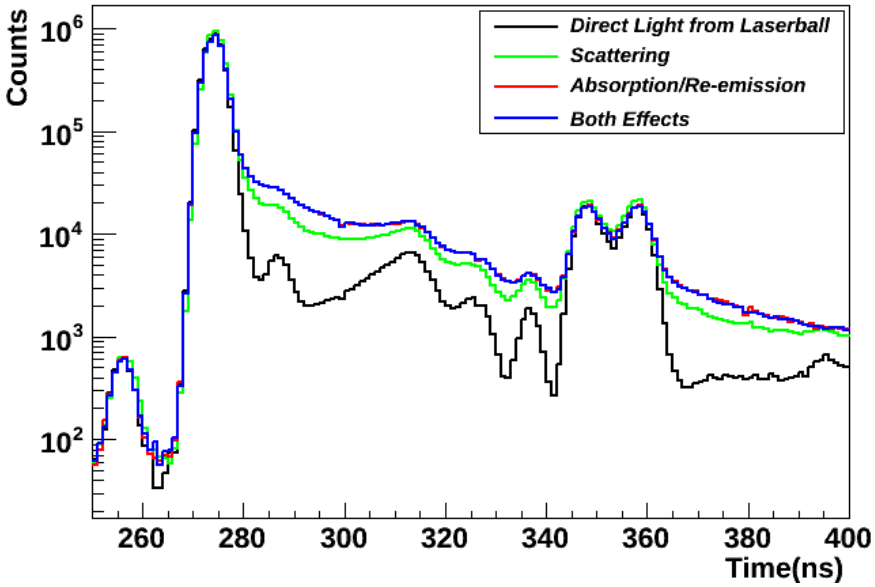


Figure 5.10: The different contributions of non-direct light for the laserball running at 490 $nm$ in the centre of the detector.

Figure 5.10 shows the contributions of non-direct light running with Coumarin-481 laser dye, with a 490 $nm$ peak wavelength. From observing the differences from 439 $nm$ to 490 $nm$ wavelength there is no visible change in the contribution of absorption/re-emission. However, there is an increase in the amount of non-direct light in scattering seen by an increased sharpness in features past the prompt peak. In the reflections from PMTs/Concentrators the amount of non-direct light from scattering overtakes absorption/re-emission for the first time.

As far as non-direct light in the $\pm 4$ $ns$ standard time profile of interest, 490 $nm$ contributes the least compared to all previous wavelengths, with only 2.84%. The increased amount of scattering seen in the full time profile is also observed in the standard time profile, contributing 5.18%, whereas absorption/re-emission only contributes 2.93%. It seems that when both processes are observed that non-direct light the would should in the prompt peak is pushed outside of it from multiple scattering and/or absorption/re-emission and thus the individual effects contribute more than the total. Like with the previous wavelength, the asymmetric time profile reduces less than a percent for each subsequent cut giving a contribution of 1.97% from the $^{+3}_{-4}$ $ns$ profile and 1.10% from the $^{+2}_{-4}$ $ns$ profile. All these time profiles along with the time profiles from the previous simulations are summarized in Table 5.2.

In conclusion an asymmetric time profile can be a useful tool for removing contributions of non-direct light from absorption/re-emission and scattering. However as the chosen wavelength increases and one must weight the benefit of more light collection versus the difficulty of working with non-direct light. The wavelengths that benefit from the $^{+3}_{-4}$ $ns$ asymmetric time profile are at 380 $nm$, 396 $nm$, and 421 $nm$ while the other wavelengths do not remove enough non-direct light to make up for the loss of prompt light. Therefore there would not be just one time profile but two different time profiles at this position.

| Scattering Only | | | | | |
|---|---|---|---|---|---|
| Wavelength | $\pm 4\ ns$ [%] | $^{+3}_{-4}\ ns$ [%] | Prompt Reduc. [%] | $^{+2}_{-4}\ ns$ [%] | Prompt Reduc. [%] |
| 380 | 5.36 | 3.86 | 4.18 | 2.32 | 12.17 |
| 396 | 6.66 | 5.18 | 3.49 | 3.43 | 10.26 |
| 421 | 3.63 | 2.52 | 4.38 | 1.42 | 13.20 |
| 439 | 3.82 | 3.24 | 3.49 | 3.13 | 10.75 |
| 490 | 5.18 | 4.47 | 2.42 | 3.57 | 7.74 |
| Absorption/Re-emission Only | | | | | |
| Wavelength | $\pm 4\ ns$ [%] | $^{+3}_{-4}\ ns$ [%] | Prompt Reduc. [%] | $^{+2}_{-4}\ ns$ [%] | Prompt Reduc. [%] |
| 380 | 19.69 | 13.95 | 9.20 | 8.22 | 20.84 |
| 396 | 9.36 | 6.53 | 4.90 | 3.74 | 12.47 |
| 421 | 5.29 | 3.62 | 4.95 | 2.03 | 14.17 |
| 439 | 3.94 | 2.68 | 4.13 | 1.49 | 12.24 |
| 490 | 2.93 | 2.05 | 2.51 | 1.18 | 7.60 |
| Both Scattering and Absorption/Re-emission | | | | | |
| Wavelength | $\pm 4\ ns$ [%] | $^{+3}_{-4}\ ns$ [%] | Prompt Reduc. [%] | $^{+2}_{-4}\ ns$ [%] | Prompt Reduc. [%] |
| 380 | 21.52 | 15.74 | 9.43 | 9.71 | 21.54 |
| 396 | 11.40 | 8.44 | 5.14 | 5.29 | 13.18 |
| 421 | 5.34 | 3.68 | 4.95 | 2.10 | 14.16 |
| 439 | 4.53 | 3.62 | 3.81 | 3.22 | 11.31 |
| 490 | 2.84 | 1.97 | 2.51 | 1.10 | 7.60 |

Table 5.2: The contributions of non-direct light for all laser dyes indicated by their peak wavelength, along with the reduction of prompt light, with an uncertainty of $\pm 0.06\%$, for different time profiles off the prompt peak. The laserball is positioned in the centre of the detector for all of these simulations.

## 5.4 Position (-1.9 $m$, 0, -4.6 $m$) Laserball Simulations

Non central laserball runs are done in order to understand the effects of shadowing of the hold up and hold down ropes and potential radial dependant effects. In order to get a clearer image several off centre positions have been chosen. Furthermore how well the PMTs collect light at different angles, the angular response, can also be measured. To understand the contribution of non-direct light from absorption/re-emission and scattering similar simulations were described in Section 5.3.

Figures 5.11 – 5.15 show the laserball simulations done at position (-1.9 $m$, 0, -4.6 $m$) from the centre of the detector. These simulations are done with time of flight corrections from calibrated PMTs. Due to the asymmetric distance from light produced by the laserball to the PMTs, the prompt peak is more spread out that from running the laserball at the centre of the detector. Also because of the sharpness on the left side of the prompt peak, going backwards in time, there is less non-direct light that can captured in a $\pm 4$ $ns$ time profile, seen in Table 5.3. Therefore the asymmetric time profile does not benefit laserball calibrations in this position.

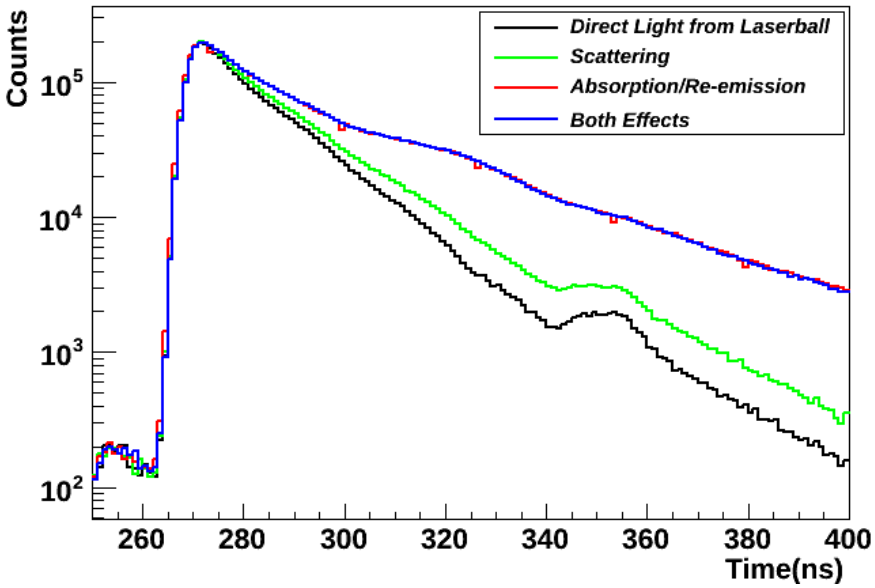


Figure 5.11: The different contributions of non-direct light for the laser running at 380 $nm$ in position (-1.9 $m$, 0, -4.6 $m$) in the detector.

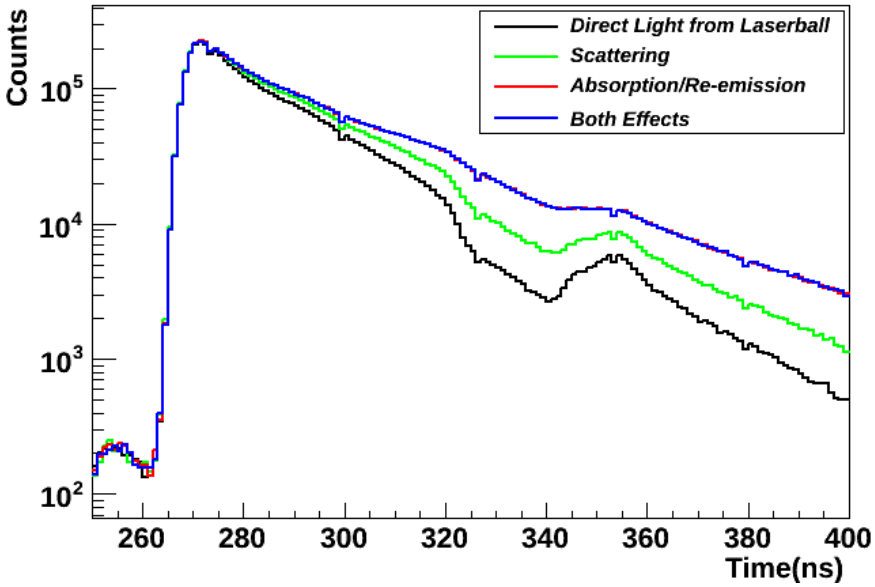


Figure 5.12: The different contributions of non-direct light for the laser running at 396 $nm$ in position (-1.9 $m$, 0, -4.6 $m$) in the detector.

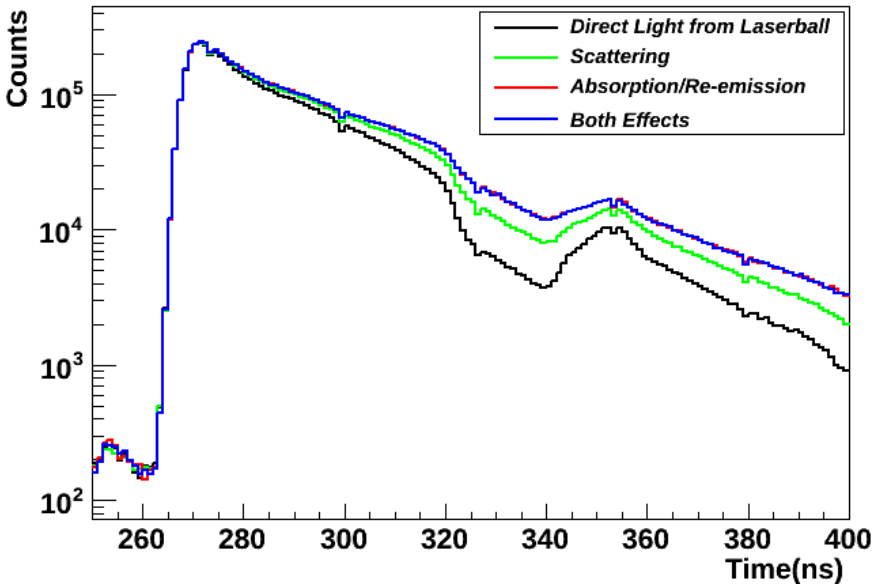


Figure 5.13: The different contributions of non-direct light for the laser running at 421 $nm$ in position (-1.9 $m$, 0, -4.6 $m$) in the detector.

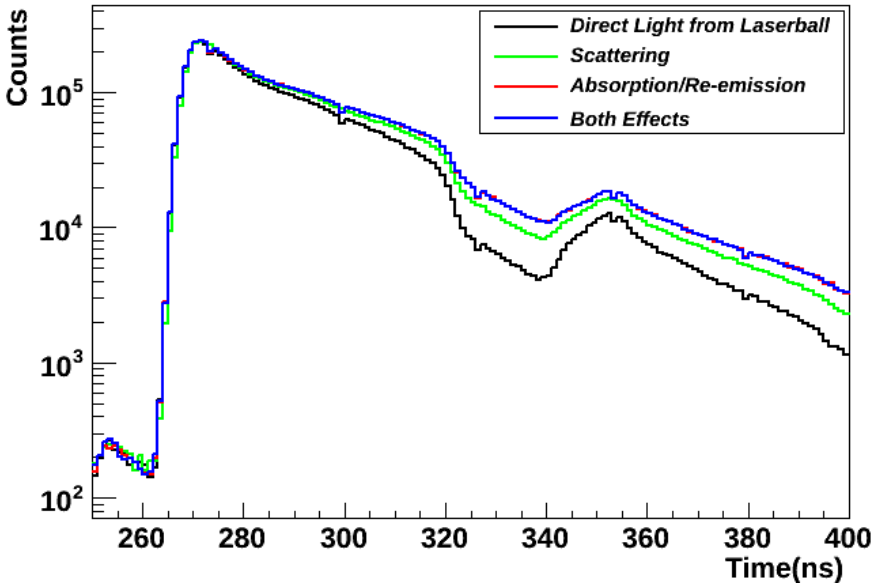


Figure 5.14: The different contributions of non-direct light for the laser running at 439 $nm$ in position (-1.9 $m$, 0, -4.6 $m$) in the detector.

| Scattering Only | | | | | |
|---|---|---|---|---|---|
| Wavelength | $\pm 4$ $ns$ [%] | $^{+3}_{-4}$ $ns$ [%] | Prompt Reduc. [%] | $^{+2}_{-4}$ $ns$ [%] | Prompt Reduc. [%] |
| 380 | 0.72 | 0.53 | 11.25 | 0.29 | 23.50 |
| 396 | 0.69 | 0.43 | 11.31 | 0.25 | 23.37 |
| 421 | 0.39 | 0.23 | 11.18 | 0.09 | 23.07 |
| 439 | 2.48 | 2.41 | 11.32 | 2.46 | 23.34 |
| 490 | 0.36 | 0.26 | 10.96 | 0.14 | 22.77 |
| Absorption/Re-emission Only | | | | | |
| Wavelength | $\pm 4$ $ns$ [%] | $^{+3}_{-4}$ $ns$ [%] | Prompt Reduc. [%] | $^{+2}_{-4}$ $ns$ [%] | Prompt Reduc. [%] |
| 380 | 2.92 | 2.40 | 11.64 | 2.00 | 24.04 |
| 396 | 1.25 | 0.83 | 11.47 | 0.49 | 23.67 |
| 421 | 0.77 | 0.54 | 11.23 | 0.29 | 23.20 |
| 439 | 0.79 | 0.59 | 11.18 | 0.33 | 23.16 |
| 490 | 2.15 | 2.35 | 10.84 | 2.69 | 22.48 |
| Both Scattering and Absorption/Re-emission | | | | | |
| Wavelength | $\pm 4$ $ns$ [%] | $^{+3}_{-4}$ $ns$ [%] | Prompt Reduc. [%] | $^{+2}_{-4}$ $ns$ [%] | Prompt Reduc. [%] |
| 380 | 2.39 | 1.66 | 11.80 | 1.03 | 24.32 |
| 396 | 1.36 | 0.93 | 11.46 | 0.54 | 23.67 |
| 421 | 0.80 | 0.56 | 11.24 | 0.26 | 23.24 |
| 439 | 0.78 | 0.58 | 11.18 | 0.38 | 23.12 |
| 490 | 1.93 | 2.13 | 10.85 | 2.45 | 22.54 |

Table 5.3: The contribution of non-direct light for all laser dyes indicated by their peak wavelength, along with the reduction of prompt light, with an uncertainty of $\pm 0.06\%$, for different time profiles off the prompt peak. The laserball is positioned at (-1.9 $m$, 0, -4.6 $m$) for all these simulations.

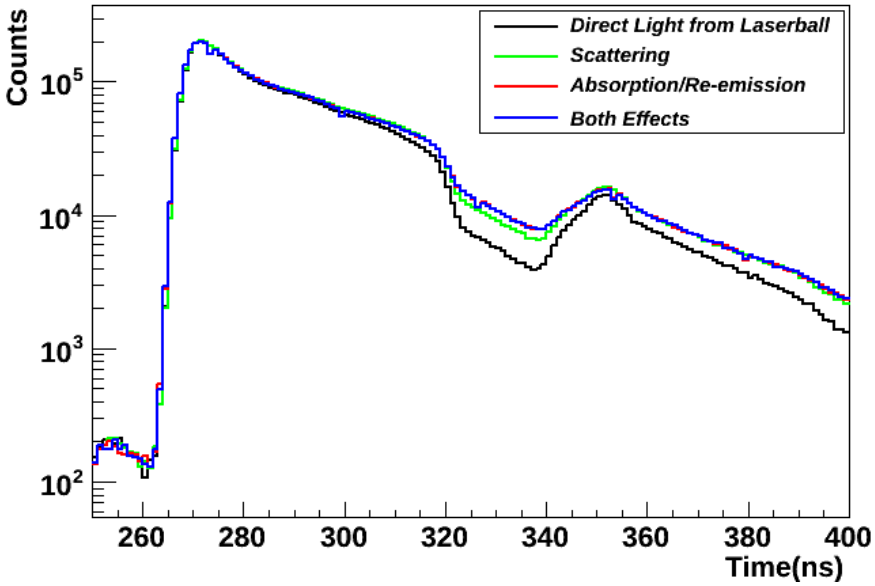


Figure 5.15: The different contributions of non-direct light for the laser running at 490 $nm$ in position (-1.9 $m$, 0, -4.6 $m$) in the detector.

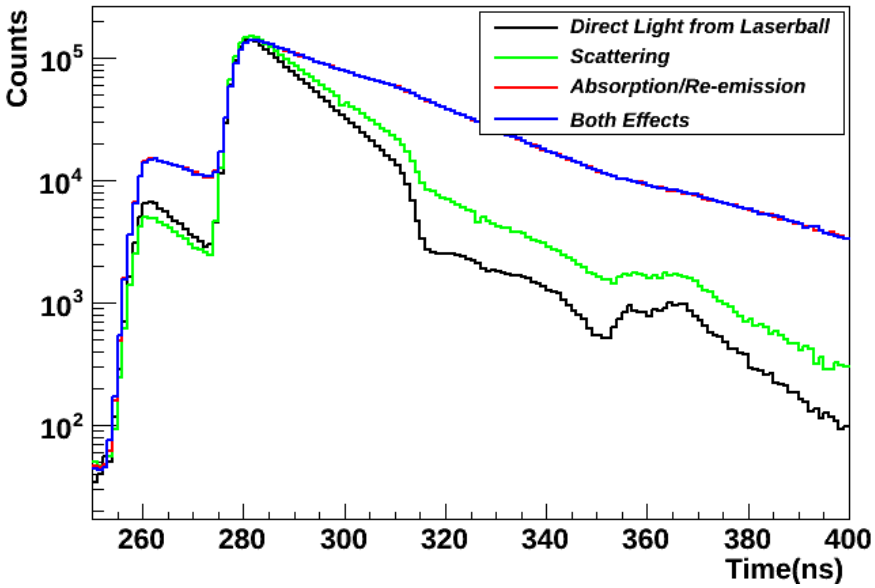


Figure 5.16: The different contributions of non-direct light for the laser running at 380 $nm$ in position (-2.3 $m$, 0, -2.3 $m$) in the detector.

## 5.5 Position (-2.3 $m$, 0, -2.3 $m$) Laserball Simulations

The following simulations in Figures 5.16 – 5.20 are for the laserball in position (-2.3 $m$, 0, -2.3 $m$) from the centre of the detector. Like with the previous position simulations the prompt light is also spread out, but it is more confined due to the laserball being closer to the centre of the detector. Furthermore because of this sharpness of the prompt peak, also seen in the previous position simulations, there is less non-direct light collected in the $\pm 4$ time profile. Therefore the asymmetric time profile does not benefit laserball calibrations in this position.

The 380 $nm$ simulation stands out from the all others at this position. A large amount of light collected pre-pulse from the prompt light and with absorption/re-emission this effect seems to have multiplied. By repeating the simulation at this wavelength several times and analyzing them separately the source of the error was determined to not be a human factor. It will be interesting to see if this effect is apparent during "live" laserball runs.

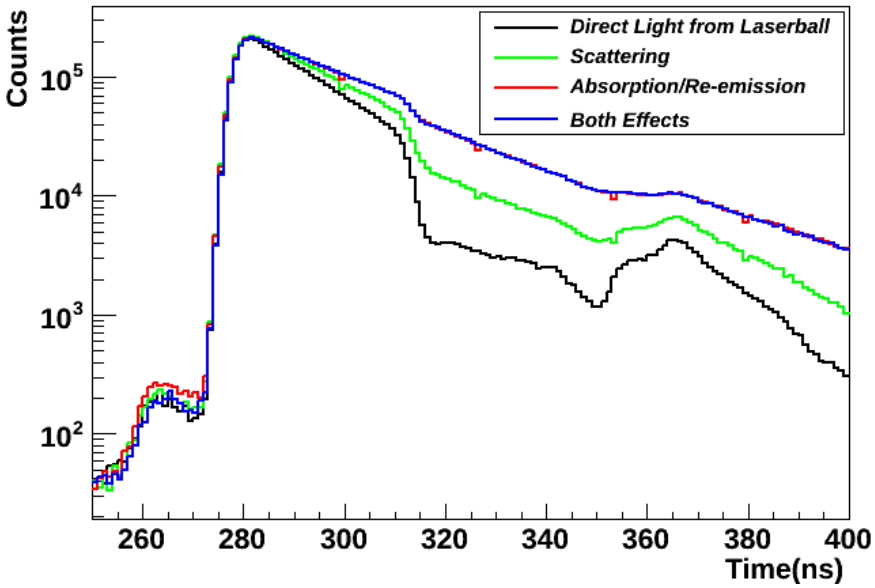


Figure 5.17: The different contributions of non-direct light for the laser running at 396 $nm$ in position (-2.3 $m$, 0, -2.3 $m$) in the detector.

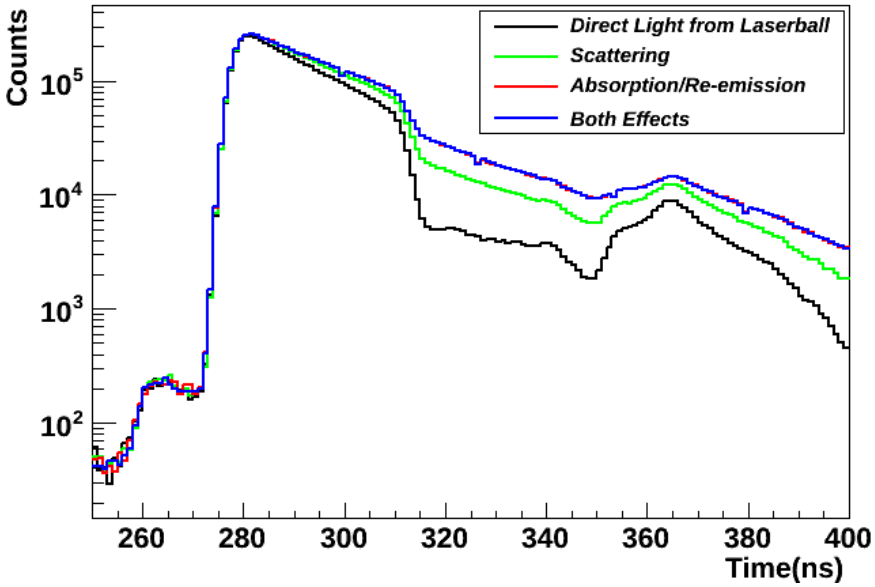


Figure 5.18: The different contributions of non-direct light for the laser running at 421 $nm$ in position (-2.3 $m$, 0, -2.3 $m$) in the detector.

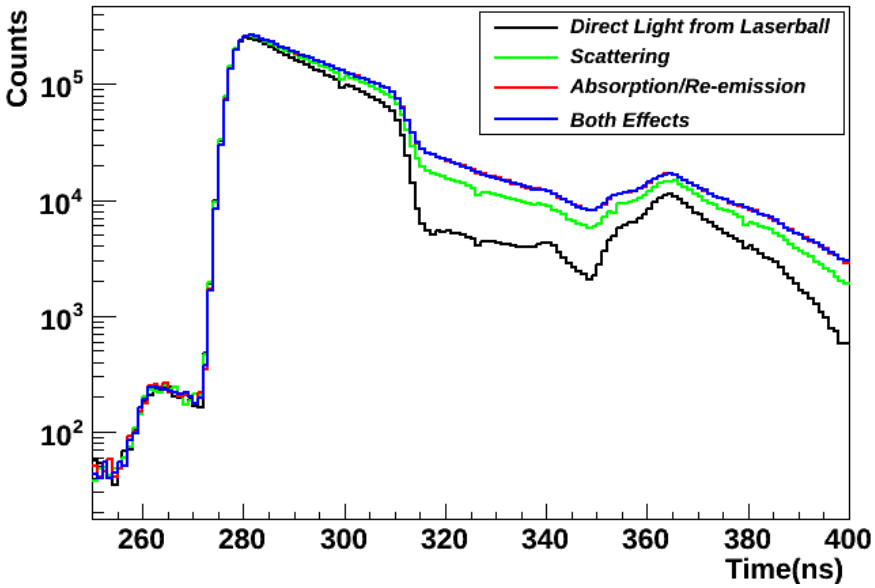


Figure 5.19: The different contributions of non-direct light for the laser running at 439 $nm$ in position (-2.3 $m$, 0, -2.3 $m$) in the detector.

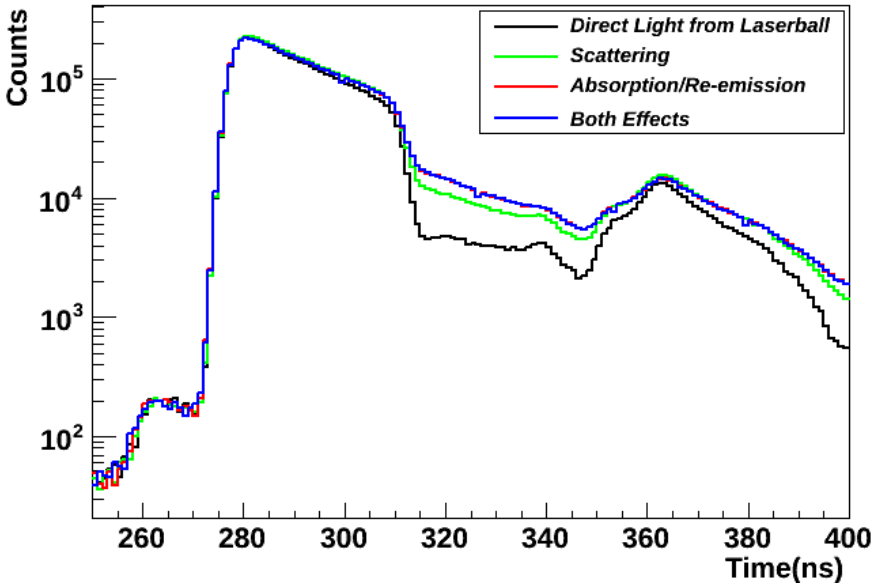


Figure 5.20: The different contributions of non-direct light for the laser running at 490 $nm$ in position (-2.3 $m$, 0, -2.3 $m$) in the detector.

| Scattering Only | | | | | |
|---|---|---|---|---|---|
| Wavelength | $\pm 4$ $ns$ [%] | $^{+3}_{-4}$ $ns$ [%] | Prompt Reduc. [%] | $^{+2}_{-4}$ $ns$ [%] | Prompt Reduc. [%] |
| 380 | 1.66 | 1.31 | 10.70 | 0.99 | 22.13 |
| 396 | 1.81 | 1.51 | 11.05 | 1.26 | 22.64 |
| 421 | 0.87 | 0.60 | 11.00 | 0.40 | 22.50 |
| 439 | 0.90 | 0.66 | 12.20 | 0.42 | 24.92 |
| 490 | 0.52 | 0.36 | 12.00 | 0.13 | 24.54 |
| Absorption/Re-emission Only | | | | | |
| Wavelength | $\pm 4$ $ns$ [%] | $^{+3}_{-4}$ $ns$ [%] | Prompt Reduc. [%] | $^{+2}_{-4}$ $ns$ [%] | Prompt Reduc. [%] |
| 380 | 4.87 | 3.37 | 11.92 | 1.88 | 24.27 |
| 396 | 2.43 | 1.73 | 11.42 | 1.07 | 23.31 |
| 421 | 1.40 | 0.99 | 11.08 | 0.62 | 22.63 |
| 439 | 1.62 | 1.23 | 12.47 | 0.83 | 25.43 |
| 490 | 0.82 | 0.85 | 11.83 | 0.89 | 24.15 |
| Both Scattering and Absorption/Re-emission | | | | | |
| Wavelength | $\pm 4$ $ns$ [%] | $^{+3}_{-4}$ $ns$ [%] | Prompt Reduc. [%] | $^{+2}_{-4}$ $ns$ [%] | Prompt Reduc. [%] |
| 380 | 4.96 | 3.44 | 11.93 | 2.02 | 24.21 |
| 396 | 2.55 | 1.79 | 11.58 | 1.08 | 23.60 |
| 421 | 1.32 | 0.96 | 11.04 | 0.57 | 22.61 |
| 439 | 1.77 | 1.35 | 12.49 | 0.93 | 25.46 |
| 490 | 0.87 | 0.85 | 11.86 | 0.86 | 24.20 |

Table 5.4: The contribution of non-direct light for all laser dyes indicated by their peak wavelength, along with the reduction of prompt light, with an uncertainty of $\pm 0.06\%$, for different time profiles off the prompt peak. The laserball is positioned at (-2.3 $m$, 0, -2.3 $m$) for all these simulations.

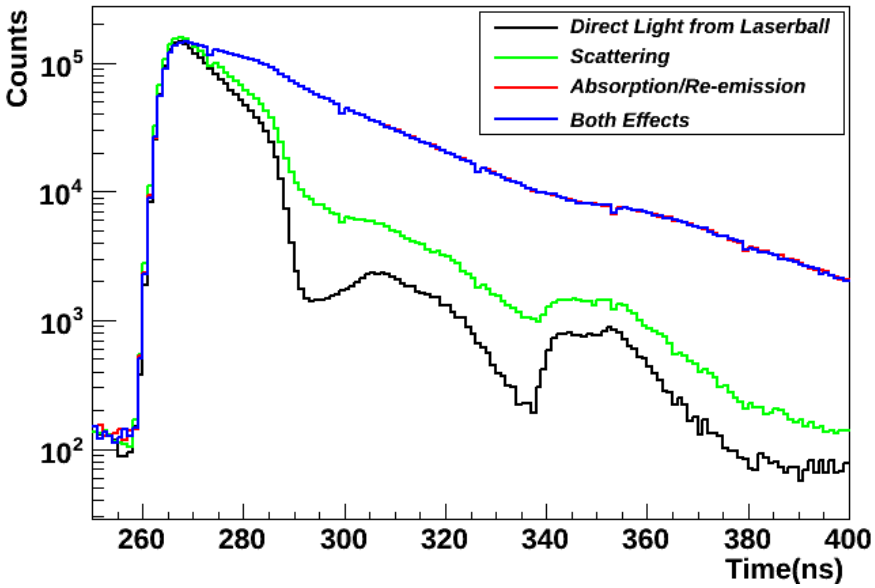


Figure 5.21: The different contributions of non-direct light for the laser running at 380 $nm$ in position (-1.5 $m$, 0, -1.5 $m$) in the detector.

## 5.6 Position (-1.5 $m$, 0, -1.5 $m$) Laserball Simulations

The following simulations in Figures 5.21 – 5.25 are for the laserball in position (-1.5 $m$, 0, -1.5 $m$) from the centre of the detector. Like with the previous position simulations the prompt light is also spread out, but it is more confined due to the laserball being closer to the centre of the detector. Furthermore because of this sharpness of the prompt peak, also seen in the previous position simulations, there is less non-direct light collected in the $\pm 4$ time profile. Therefore the asymmetric time profile does not benefit laserball calibrations in this position.

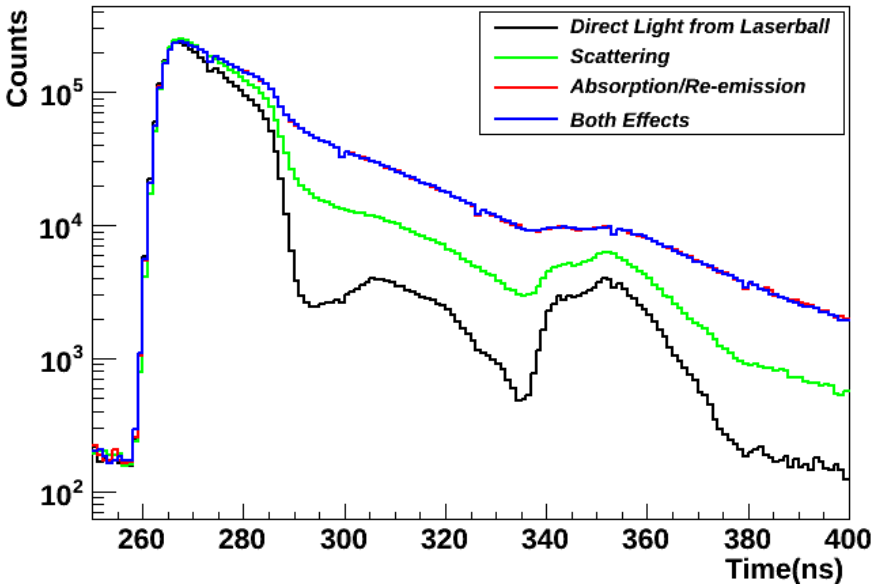


Figure 5.22: The different contributions of non-direct light for the laser running at 396 $nm$ in position (-1.5 $m$, 0, -1.5 $m$) in the detector.

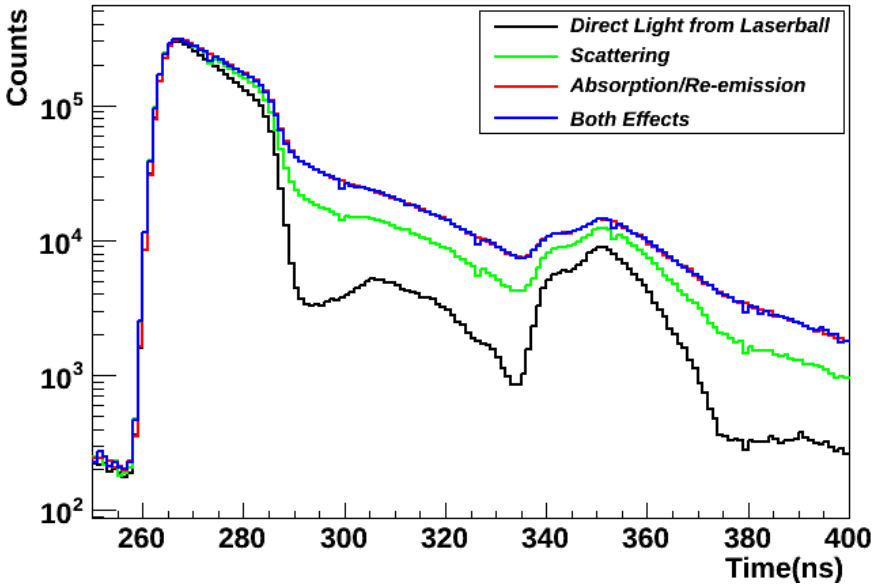


Figure 5.23: The different contributions of non-direct light for the laser running at 421 $nm$ in position (-1.5 $m$, 0, -1.5 $m$) in the detector.

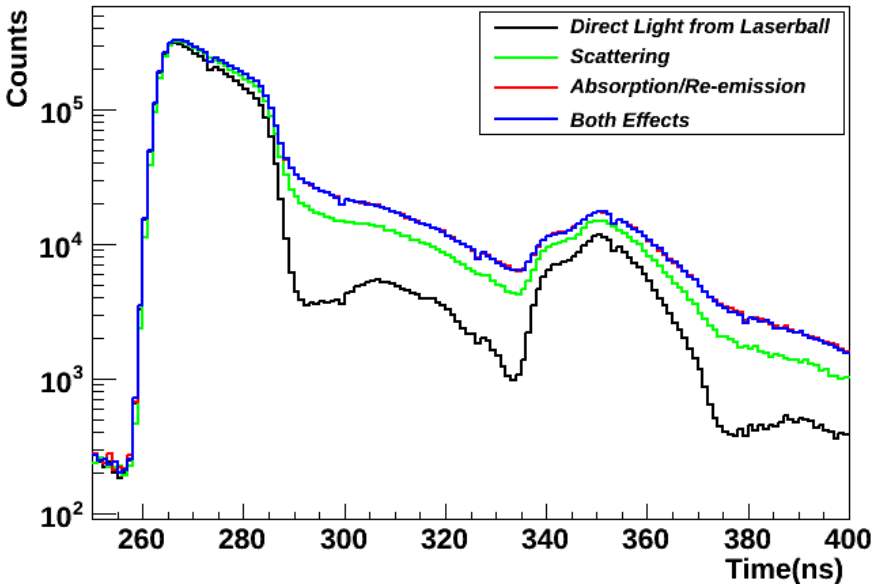


Figure 5.24: The different contributions of non-direct light for the laser running at 439 $nm$ in position (-1.5 $m$, 0, -1.5 $m$) in the detector.

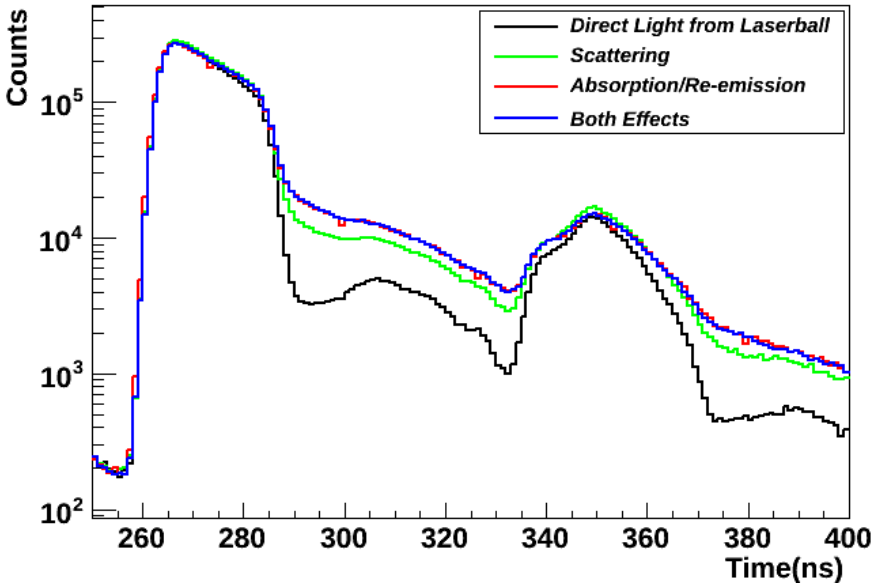


Figure 5.25: The different contributions of non-direct light for the laser running at 490 $nm$ in position (-1.5 $m$, 0, -1.5 $m$) in the detector.

| Scattering Only | | | | | |
|---|---|---|---|---|---|
| Wavelength | $\pm 4$ $ns$ [%] | $^{+3}_{-4}$ $ns$ [%] | Prompt Reduc. [%] | $^{+2}_{-4}$ $ns$ [%] | Prompt Reduc. [%] |
| 380 | 2.99 | 2.65 | 10.51 | 2.47 | 21.79 |
| 396 | 2.95 | 2.33 | 12.73 | 1.55 | 26.25 |
| 421 | 2.18 | 2.12 | 11.90 | 2.33 | 24.37 |
| 439 | 2.02 | 1.55 | 12.08 | 1.08 | 24.74 |
| 490 | 0.54 | 0.32 | 11.60 | 0.13 | 23.72 |
| Absorption/Re-emission Only | | | | | |
| Wavelength | $\pm 4$ $ns$ [%] | $^{+3}_{-4}$ $ns$ [%] | Prompt Reduc. [%] | $^{+2}_{-4}$ $ns$ [%] | Prompt Reduc. [%] |
| 380 | 6.67 | 4.62 | 12.25 | 2.76 | 24.79 |
| 396 | 3.37 | 2.40 | 12.82 | 1.50 | 26.15 |
| 421 | 1.90 | 1.32 | 12.47 | 0.83 | 25.51 |
| 439 | 1.53 | 1.04 | 11.86 | 0.62 | 24.24 |
| 490 | 1.69 | 1.78 | 11.27 | 1.91 | 23.14 |
| Both Scattering Only and Absorption/Re-emission | | | | | |
| Wavelength | $\pm 4$ $ns$ [%] | $^{+3}_{-4}$ $ns$ [%] | Prompt Reduc. [%] | $^{+2}_{-4}$ $ns$ [%] | Prompt Reduc. [%] |
| 380 | 6.74 | 4.69 | 12.26 | 2.82 | 24.82 |
| 396 | 3.15 | 2.23 | 12.80 | 1.28 | 26.18 |
| 421 | 2.32 | 2.05 | 12.09 | 2.03 | 24.71 |
| 439 | 1.74 | 1.23 | 11.87 | 0.81 | 24.25 |
| 490 | 0.48 | 0.31 | 11.57 | 0.13 | 23.71 |

Table 5.5: The contribution of non-direct light for all laser dyes indicated by their peak wavelength, along with the reduction of prompt light, with an uncertainty of $\pm 0.06\%$, for different time profiles off the prompt peak. The laserball is positioned at (-1.5 $m$, 0, -1.5 $m$) for all these simulations.

## 5.7 Summary of Laserball Simulations

Both the laserball and ELLIE systems will be used for optical calibrations in SNO+. Therefore simulations can be used as a tool to better understand the laserball properties, which will then be used to determine the best calibration methods and most effective analysis strategies. By improving on the generator to produce distributed wavelengths instead of a single wavelength, the simulations will more closely adhere to reality. Simulations can also be used to understand potential problems before they even occur, like the additional complexity of analysis from laserball calibration runs coming non-direct light from absorption/re-emission and scattering in the scintillator. By introducing an asymmetric time profile, constraining the time after the peak where most non-direct light would be seen, these contributions can be constrained.

Furthermore simulations can be used to select which physical processes are considered, something not achievable in the real world, and thus both effects can be compared independently to understand the basic effects. This reveals the wavelength dependence of absorption/re-emission and how lower wavelengths suffer more; for example there is 19.69% non-direct light at 380 $nm$, and only 2.93% non-direct light at 490 $nm$ both in the centre of the detector. Also seen is that scattering does not contribute much non-direct light and is less wavelength dependent than with absorption/re-emission.

By moving the position of the laserball away from the centre the overall shape of the full timing profile changes. This is because of the steepness of the signal, going backwards in time off the prompt peak, that there is little non-direct light seen. In conclusion, the only places that an asymmetric time window makes a significant contribution is for the 380 $nm$, 396 $nm$, and 421 $nm$ wavelength dyes used in the centre of the detector.

# Chapter 6: Calibration Manipulator Gloves

The calibration manipulator gloves will be used in SNO+ for the setup and deployment of a calibration source that will be deployed inside the detector. These gloves will be attached to two different systems, the universal interface (UI), Figure 4.2, and the source storage box, Figure 4.5. The gloves will also serve different purposes at each location; the UI requires use of the gloves to attach the side ropes from the side rope manipulator boxes, Chapter 4.2.4, and the source box requires the gloves to couple a selected source to the umbilical rope from the umbilical retrieval mechanism, Chapter 4.2.2.

The reason why glove materials need to be studied is that common materials used in glove manufacturing are known to allow radon found in the air to permeate through them. Since radon daughters are a known background for both double beta phase and solar phase, the contributions from the calibration manipulator gloves should be well understood. An effective way of estimating the contribution of radon from permeation is by developing a models for radon permeability. These models can than be used to simulate the amount of radon contribution from materials measured with low radon permeation and therefore be a key factor in choosing the appropriate glove material.

There are of course additional requirements that need to be met in selecting a compatible glove material. When using the gloves in the UI, vision is limited to a small acrylic window and thus the process of attaching the side ropes to a calibration source will rely heavily on the sense of touch. So if the glove material is too thick or too rigid it will effectively increase in the amount of time the gloves are used, or even make them unusable. Also, the gloves should not tear or easily develop pin holes, otherwise the effectiveness of the material as a radon barrier will be compromised. Furthermore, since calibration sources

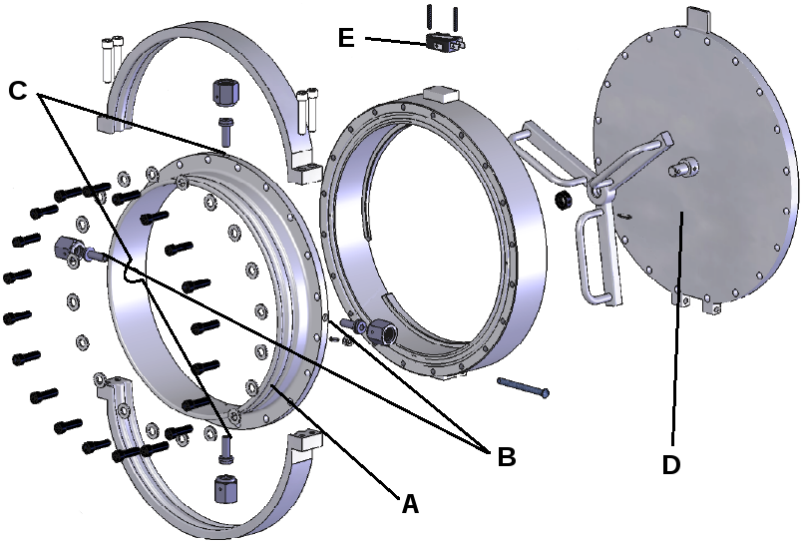


Figure 6.1: A deconstructed view of a glove port assembly designed by TRIUMF. Double o-ring seal (A) used to prevent leaks from the outer air surrounding the UI. The o-rings will be pumped through two 1/4 inch VCR ports (B). An additional pair of 1/4 inch VCR ports (C) will pump the air which will become isolated from the clamping port (D). A micro switch (E) is used to determine if the glove port is opened or closed.

will be deployed in the detector volume, the chosen glove material should not leech into or affect the absorption spectrum of the scintillator.

## 6.1 Glove Setup

There are four pairs of 8" diameter glove ports, see Figure 6.1, located around the upper UI. Between each pair of glove ports is a 6" inch view port which will give a limited view inside the UI. The source storage box will also have two pairs of 8" glove ports, but large windows to see inside.

Each glove port uses a double o-ring configuration with the glove material placed on top of the o-rings to act as a seal between the outer air volume and the inner cover gas volumes. Double o-rings are used so the air in between can be purged with cover gas to reduce the amount of radon in the seals. For further protection on the inside of the glove port is a pivoting clamping handle which can be used to isolate the gloves from the respective cover gas volume. Because the clamping seal is not visible from the outside, a micro switch is installed to indicate whether or not the seal is engaged. There are also VCR glands located

| Material | $P[cm^2/s]$ | $D[cm^2/s]$ | $S$ |
|---|---|---|---|
| Butyl Rubber | $2.1 \times 10^{-8}$ | $4.9 \times 10^{-9}$ | 4.4 |
| Butyl | $1 \times 10^{-11}$ | $2 \times 10^{-10}$ | 0.05 |
| Silver Shield | $4 \times 10^{-18}$ | $4 \times 10^{-17}$ | 0.1 |

Table 6.1: Permeability, diffusion, and solubility coefficients for Butyl rubber, Butyl and Silver Shield material[57][58].

between the glove and the clamping seal to purge the outer glove material with cover gas quality air to prevent surface lead build up.

The glove materials that have been researched are Butyl rubber and Silver Shield. Butyl rubber is a co-polymer of isoButylene with isoprene and is a well known glove material with low permeability to air. Commercially Butyl gloves comes in standard glove box size, 32" long and 8" port size, and has a thickness of either 15 mil or 30 mil, where mil is a thousandth of an inch. Silver Shield is a registered trademark of Siebe North, Inc. Silver Shield is a composite material of ethylene vinyl alcohol laminated to polyethylene and is known for excellent permeation protection against a large number of chemicals. However, the largest commercially produced Silver Shield glove is only 29" long, 2.7 mil thick, and only comes in a large hand size.

Permeability (P) constants for Butyl and Silver Shield have already been measured by Wojcik [57] and Schowalter, Connolly, and Doyle [58]. These values are reproduced in Table 6.1 along with the diffusion (D) and solubility (S) coefficients. These values for diffusion indicate the rate of transfer of radon through the respective material, where as solubility is the equilibrium constant between the external and internal concentrations of radon at the membrane surface. The value for permeability is just the product of diffusion and solubility, i.e. $P = D \times S$.

However, in the two cited articles there is a difference of three orders of magnitude between the Butyl and the Butyl rubber measurements. Schowalter, Connolly, and Doyle measured Butyl for use in gaskets, general shielding and glovebox materials and did not indicate if the measure material is the manufactured material specifically used for gloves. Furthermore, the calculation for the diffusion coefficient is derived from an estimation from

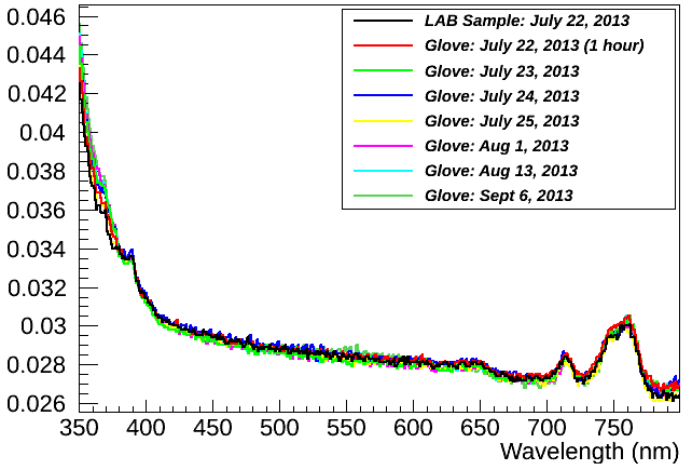


Figure 6.2: Effects on the absorption spectrum of the scintillator (LAB) with exposure to Silver Shield material.

the diffusion coefficients of other noble gases and their respective atomic diameters, whereas Wojcik directly measured the diffusion coefficient from radon diffusion. Therefore the permeability constants used for Butyl in the simulations will come from the measurements made by Wojcik.

The compatibility of the Silver Shield material with LAB was also measured with laser absorption spectrometry (LAS) on the surface facility of SNOLAB. First pure scintillator (LAB) was measured as the baseline and then the Silver Shield material was submerged in the same scintillator volume. Then the scintillator absorption was measured after an hour, and this test was repeated over periods of days. The result are shown in Figure 6.2, and therefore Silver Shield material is compatible with the scintillator.

## 6.2 Modelling Permeability

There are two models needed that have been developed to interpret the initial conditions of the gloves. The first condition is when the gloves are always left exposed to the lab air on the side where a person's hands would be placed. With a constant concentration of radon in the air these gloves will eventually reach a steady state condition, which is the first model.

The second model is derived from the condition that after the gloves are used a seal is placed on the user's side of the gloves and that air volume is purged and kept in cover

gas quality air. This would remove any build up concentration of radon inside the glove membrane so that when the gloves are used again it does not reach the fastest rate of permeation, the steady state rate. This model will be referred to as the active reduction model.

### 6.2.1 Steady State Rate

When the gloves are always left in the lab air after use it is easy to assume that permeation of radon will reach a steady state condition. The steady state flux rate of radon permeating through a glove of thickness $d$ is known to be proportional to the gradient of the concentration of radon within the material measured normal to the glove membrane i.e.,

$$F = -D\left(\frac{\partial C^{'}}{\partial x}\right), \tag{6.1}$$

in one dimension. Equation 6.1 is also known as Fick's first law of diffusion, where $D$ is the diffusion constant of the material, $C^{'}$ is the concentration of radon inside membrane and $x$ is the spatial coordinate normal measured normal to the membrane. If the diffusion coefficient is isotropic and constant in time, and assuming there exists a linear relationship between external concentration of radon in the air $C$ and the corresponding steady state concentration within the membrane then $C^{'}$ is determined to be the product of solubility of the material and the external concentration,

$$C^{'} = SC. \tag{6.2}$$

The concentration of radon within the glove membrane can be determined by using Fick's second law for a decaying substance,

$$\frac{\partial C^{'}}{\partial t} = D\frac{\partial^2 C^{'}}{\partial x^2} - \lambda C, \tag{6.3}$$

where $\lambda$ is the decay constant of radon. Using the steady state condition, i.e. $\frac{\partial C^{'}}{\partial t} = 0$, the

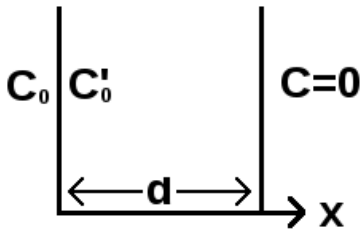


Figure 6.3: A cross sectional view of a glove material of thickness $d$ that acts as a barrier between the lab air and the cover gas.

solution to Equation 6.3 can be solved explicitly and the solution is found be in the form:

$$C^{'} = k_1 e^{\alpha x} + k_2 e^{-\alpha x}, \tag{6.4}$$

where $\alpha^2 = \frac{\lambda}{D}$ is used to simplify the solution.

The initial conditions is that the concentration of radon in the surrounding lab air, $C_0$, and the cover gas which does not contribute any amount of radon is separated by a glove membrane of thickness $d$. This is visually represented in Figure 6.3 and can be expressed mathematically as,

$$x = 0 \qquad C^{'} = SC_0, \tag{6.5}$$

$$x = d \qquad C^{'} = 0. \tag{6.6}$$

The exact solution of the steady state concentration is then given as,

$$C^{'}(x) = \frac{SC_0}{e^{-\alpha d} - e^{\alpha d}}(e^{-\alpha d}e^{\alpha x} - e^{\alpha d}e^{-\alpha x}). \tag{6.7}$$

From Fick's first law, Equation 6.1, and using the steady state concentration of radon inside the glove material, Equation 6.7, the radon flux can be determined. Furthermore, only the radon flux permeating into the cover gas is relevant, and so the following equation is simplified by taking the solution at $x = d$.

$$J = \frac{2\sqrt{\lambda D}SC_0}{e^{\alpha d} - e^{-\alpha d}}. \tag{6.8}$$

Because Equation 6.8 is also independent in time, then the amount of radon diffusing through the gloves into the cover gas at any time $t$ can be easily found as,

$$Q(t) = \frac{2\sqrt{\lambda D}SC_0A_S}{e^{\alpha d} - e^{-\alpha d}}t, \tag{6.9}$$

where $A_S$ is the surface area of the glove material.

### 6.2.2 Active Reduction Model

In contrast to the steady state model, the active reduction model assumes that the gloves are only exposed to the lab air while the gloves are in use. When not deployed the gloves are then purged on both sides of the membrane with cover gas quality air. This would encourage the radon concentration within the glove membrane to diffuse outwards. The motivation behind this method is to prevent the gloves from reaching the steady state rate. A more robust method is needed because the model needs to take into account the amount of radon inside the glove membrane, which would effect the diffusion rate for subsequent glove usage.

Because the exact solution from Fick's second law, Equation 6.3, is difficult to determine a numerical solution, the finite difference method, is used as an approximation to the differential equation. For the first order differential approximation is defined from the limit, i.e.,

$$\frac{\partial C}{\partial t} = \frac{C(t + \Delta t) - C(t)}{\Delta t}, \tag{6.10}$$

as $\Delta t$ approaches 0. $\Delta t$ is the time step used and is taken to be 1 second so that the term drops out of the equation. Similarly the second order differential approximation is found to be,

$$\frac{\partial^2 C}{\partial x^2} = \frac{C(x - \delta) - 2C(x) + C(x + \delta)}{\delta^2}, \tag{6.11}$$

where $\delta$ is a fractional width of the total width of the glove material $d$. Substituting the

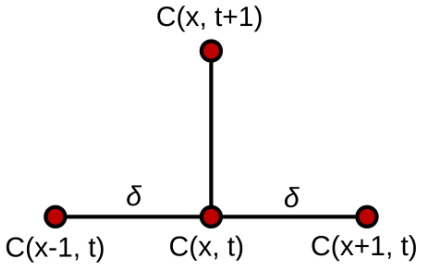


Figure 6.4: Explicit method for a finite difference scheme.

differential approximations back into Equation 6.3 and the concentration of radon within the glove membrane evolves in time as,

$$C(x,t+1) = \frac{D}{\delta^2}\Big(C(x-1,t) - 2C(x,t) + C(x+1,t)\Big) + (1-\lambda)C(x,t). \tag{6.12}$$

From here the amount of radon that diffuses into the cover gas volume is estimated from Equation 6.1 using the steady state from Fick's second law for a non-diffusing substance and then plugging the fractional width concentration of radon inside the glove membrane at the interface between glove and cover gas. This then leads to the following equation,

$$Q(t+1) = \frac{DA_S}{\delta}C(d-\delta,t) + Q(t). \tag{6.13}$$

An interesting exercise is comparing the two different models against each other. As one would expect, as time increases the active reduction model will eventually reach the steady state rate. Figure 6.5 demonstrates that the different models do indeed agree with one another. Also observable in the active reduction model is that there is a period of time where no radon permeates through the glove membrane, which occurs around half the time lag value. It is this feature that the active reduction model was created to exploit. By removing all of the build up radon in the glove membranes between uses, the amount of permeating radon would be placed back into the zero permeation region.

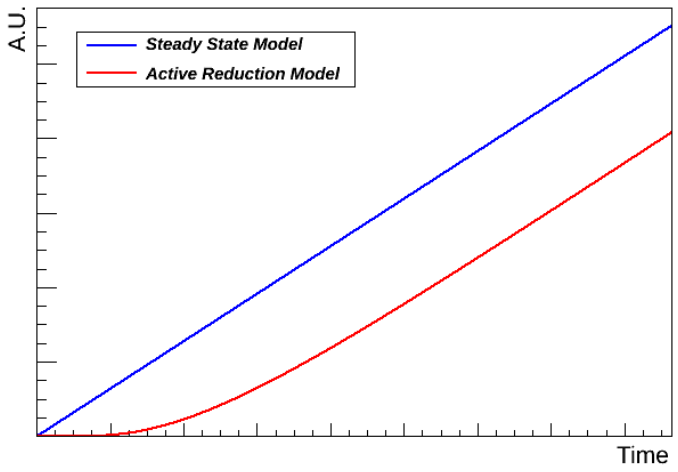


Figure 6.5: A comparison between steady state and active reduction models.

## 6.3 Results

The simulations assumed that the longest time it would take to attach the side motor ropes to a calibration source is an hour long. Also assumed is that the gloves are used once every three days and this process is simulated over a period of twenty-four days. These assumptions come from conservative estimates based on SNO experience where calibrations took place around 25% of the time.

Butyl gloves were simulated with a 30 mil glove thickness, which is the commercial standard for a thick glove box glove. For every hour exposed with these there is approximately 480 radon atoms permeating through the glove membranes. This corresponds to every jump seen in Figure 6.6 where the histogram considers the cover gas activity in decays per day. Where the model seems to reach a stable condition, that has a maximum value of 200 radon decays per day, this corresponds to a permeation rate of 200 radon atoms per day. Of course the stable condition is dependent on the frequency of glove use, but the amount of radon introduced during a single deployment still puts the gloves way over the radon budget that is imposed on the cover gas.

The other material considered, Silver Shield, only comes manufactured in 2.7 mil thickness. However, despite how relatively thin the Silver Shield gloves are, they still end up producing a steady state rate, from Equation 6.9, of 0. This comes from two factors, one

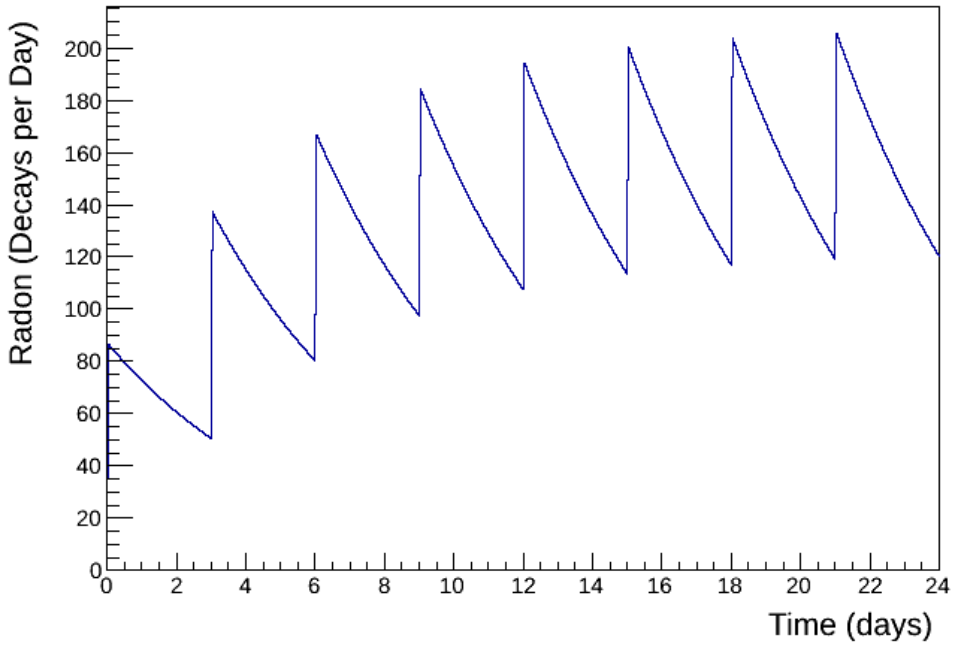


Figure 6.6: Simulated amount of radon in decays per day that permeates through a pair of 30 mil thick Butyl gloves. Each hour long spike represents an increase of 480 radon atoms introduced into the cover gas.

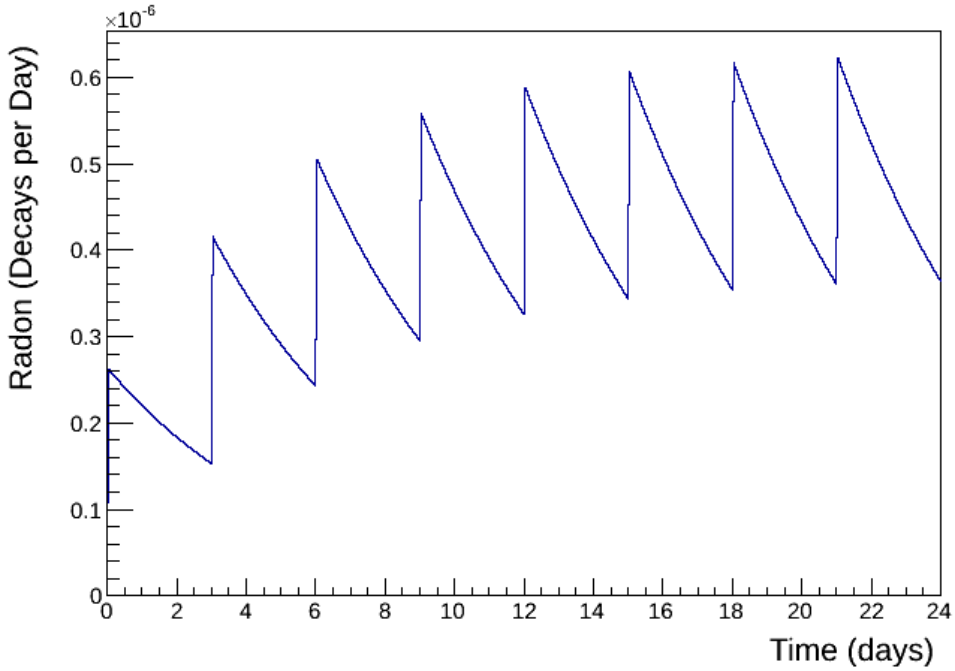


Figure 6.7: Simulated amount of radon in decays per day that permeates through a pair of 2.7 mil thick Silver Shield gloves. In this instance radon is considered to be non-decaying. For each hour exposed there is an increase of $1.1 \times 10^{-6}$ radon atoms introduced into the cover gas.

that the diffusion rate is extremely slow in Silver Shield, and two, because of the slow diffusion rate radon attempting to permeate through the material decays before reaching the other side of the glove. Nevertheless, since a null solution is not very interesting lets consider a permeation rate that ignores the decay of radon. This leads to an easily obtained steady state equation of

$$Q(t) = \frac{DSC_0A_S}{d}t. \tag{6.14}$$

Even without considering the decay of radon, the amount of radon that permeates for every hour with a pair of Silver Shield gloves is approximately $1.1 \times 10^{-6}$ radon atoms, as seen in Figure 6.7. Another fact to consider is that the time lag of the Silver Shield material is on the order of centuries, which interprets to that during the lifetime of SNO+ the Silver Shield material will never reach the steady state rate.

Because of its effectiveness as a radon barrier, Silver Shield is an excellent material to implement as the SNO+ calibration gloves. Unfortunately, the other properties of the material itself are less than ideal. The gloves only come manufactured in a large bulky hand size, the material crinkles quite easily and the smooth surface does not allow for a firm grip, which will be problematic when working with LAB. Furthermore, the way the gloves are designed, in that two hand shaped layers of the Silver Shield membrane are simply sealed together at the edges, proves problematic due to the seal itself develops pinholes quite easily.

One work around to the problem of the unfriendly Silver Shield material is by considering implementing the active reduction model with the Butyl material. Silver Shield is not considered applicable in this model because it already achieves a very low permeation rate without further complications and that this very low permeation rate also increases the amount of time needed to extract radon from the Silver Shield membrane.

During an hour long exposure to the lab air and the cover gas volume only 2.8 radon atoms permeate through a pair of gloves. The active reduction method greatly reduces the permeation that is seen in the steady state model, from 480 atoms down to only 2.8 atoms of radon. From the stable region in Figure 6.8, the gloves would only end up introducing

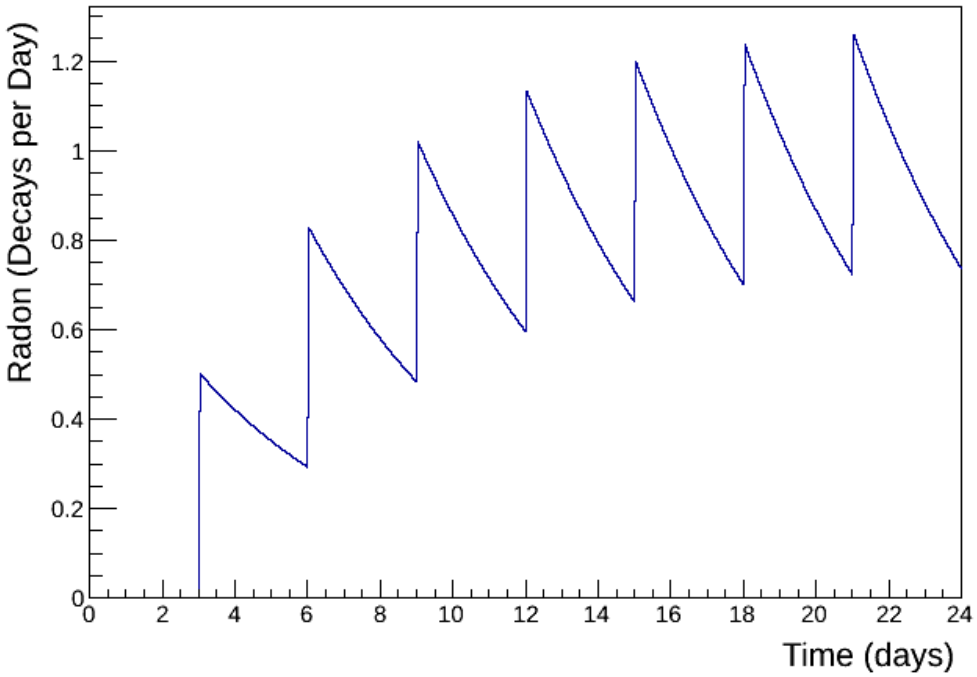


Figure 6.8: Active reduction model for 30 mil thick Butyl. For each hour deployment of a pair of gloves there are 2.8 radon atoms that are introduced into the cover gas.

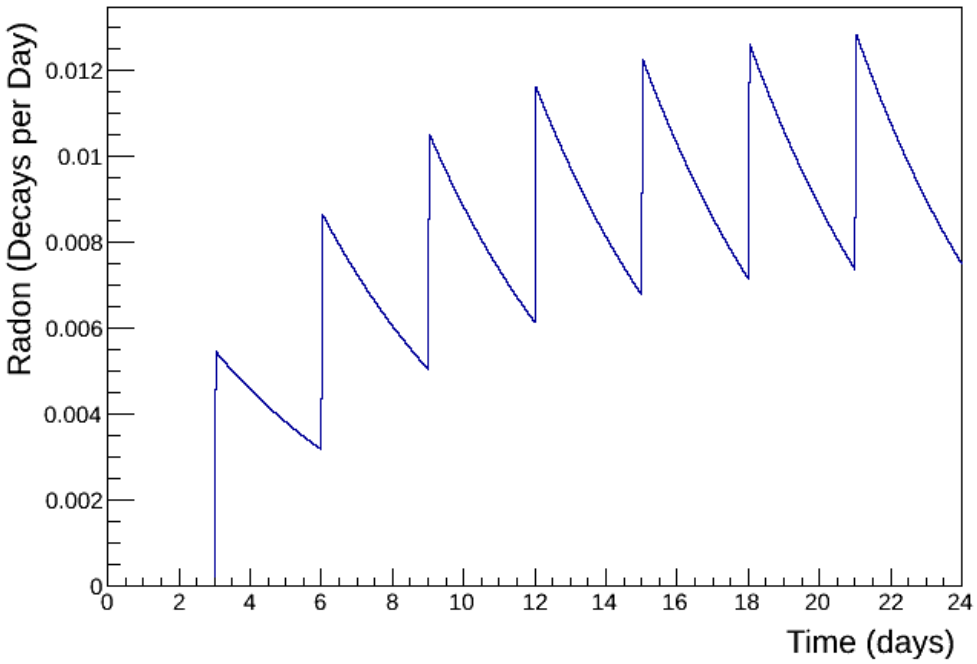


Figure 6.9: Active reduction model for 15 mil thick Butyl. With an hour long deployment of a pair of gloves there are $3 \times 10^{-2}$ radon atoms that are introduced into the the cover gas.

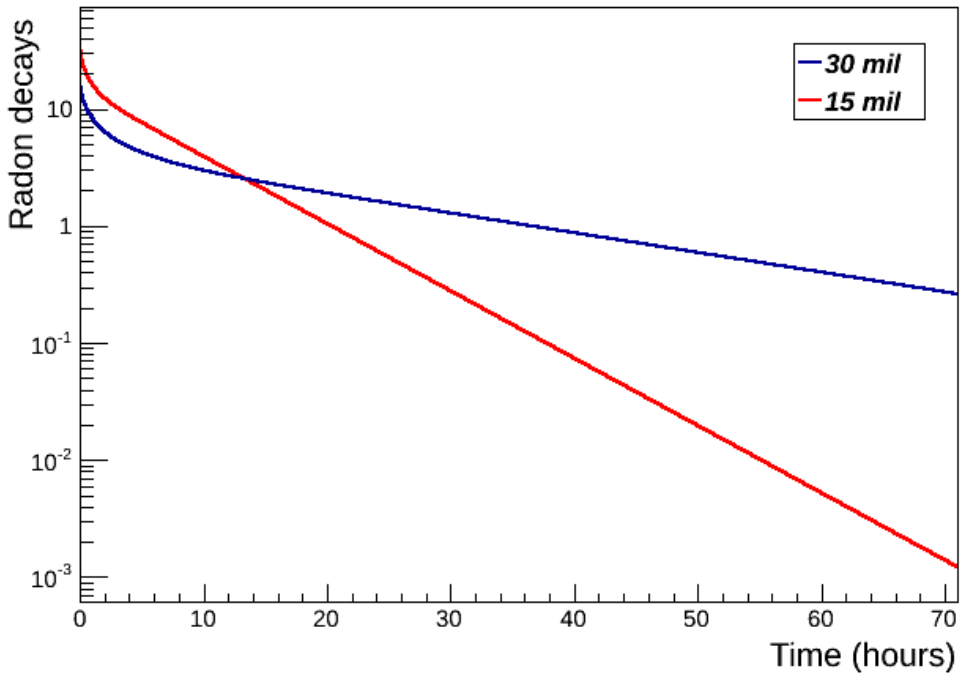


Figure 6.10: Concentration of radon left in both 15 mil and 30 mil thick Butyl gloves after being purged with cover gas over a period of 71 hours.

1.2 radon atoms per day. Also seen, there is a spike missing at day 0 that is normally found in the steady state models during the first exposure of the gloves. The reason this spike is indistinct occurs from the models assumption that there is initially no concentration of radon inside the glove membranes, which really takes advantage of the zero permeation region that is seen in Figure 6.5.

The other spikes are more distinct because the active reduction method of removing radon within the membrane of the glove does not remove all of the radon. Another interesting condition to consider is if a lower permeation rate can be achieved with a thinner glove. With a thinner glove, the radon concentration within the glove can diffuse outwards more easily and thus a better starting condition is achieved when the gloves are deployed for use.

Figure 6.10 not only demonstrates that a thinner glove has a better radon extraction rate, but also can be used to determine how long the gloves need to be purged. Assuming that a $10^{-3}$ is the desired level of radon left within the membrane, before glove deployment, then a 30 mil thick membrane would need to be purged for 215 hours. Likewise the 15 mil

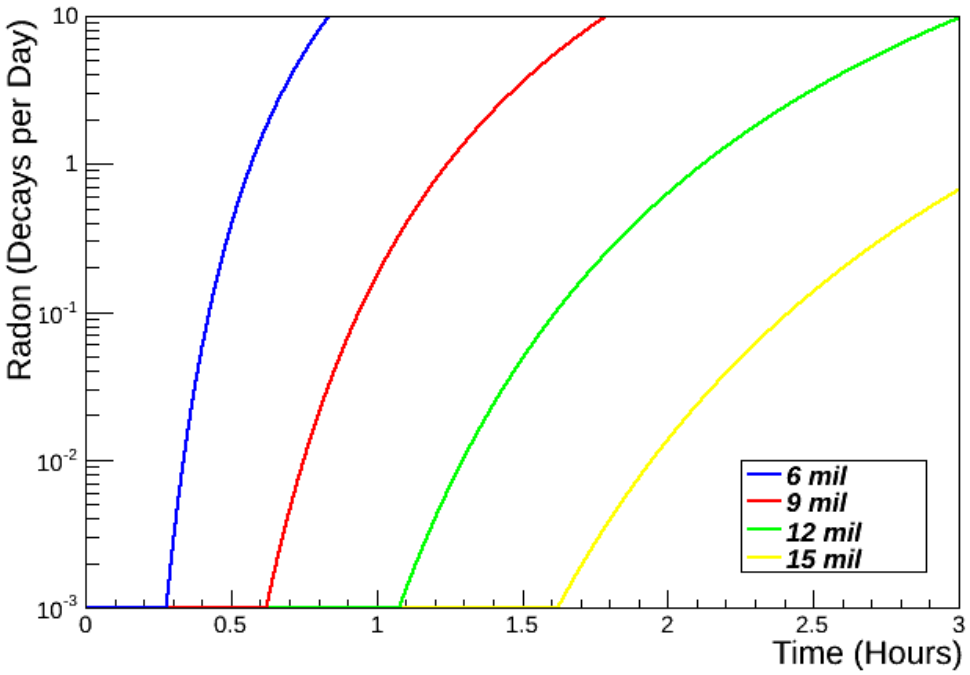


Figure 6.11: Different break through times for different glove thickness composed of a Butyl membrane.

thick membrane would only need to be purged for 72 hours. So not only can a thinner glove benefit in permeation rate, but also in the amount of time required to purge the membrane.

However, there is a limit to how thin the gloves can be made before radon permeates through the membrane in just the hour exposure. To figure out the optimal thickness for a Butyl glove, the active reduction model was used on Butyl membranes that are 6 mil, 9 mil, 12 mil and 15 mil thick. These were then simulated exposed to the lab air over a period of one day to determine the break through time in which a significant amount of radon permeates through the gloves. From Figure 6.11 it is shown the 12 mil Butyl membrane has a break through time over the assumed length of glove deployment of one hour. After simulating using the standard active reduction method, the 12 mil gloves in fact have a lower permeation rate of $2 \times 10^{-3}$ radon atoms per day per hour deployment.

In the possibility of a shorter deployment time, an even thinner glove could be used. Another possibility is selecting a different glove membrane that may have a worse diffusion co-efficient, but is more compatible with LAB or has better physical properties. The only thing this is required to take advantage of the active reduction method is that the break

| Material | Model | Thickness ($mil$) | Permeation (Rn/day) |
|---|---|---|---|
| Butyl | SS | 30 | 480 |
| Silver Shield | SS | 2.7 | $1.1\times10^{-6}$ |
| Butyl | ARM | 30 | 2.8 |
| Butyl | ARM | 15 | $3\times10^{-2}$ |

Table 6.2: Summary of radon permeation rates for gloves that are used inside the detector for a period of one hour. SS represents the steady state model, while ARM represents the active reduction model.

through time of the material is greater than the maximum deployment time for the glove.

However despite how effective the active reduction method is, the Silver Shield gloves have a lower permeation rate. The permeation rates for all methods are reproduced in Table 6.2 Also, the fact that the gloves would be essentially restricted from use while allowing the build up of radon atoms to naturally diffuse out, whereas Silver Shield could be used whenever. There is the further complications that the UI was not built to implement the active reduction method and an outer glove cover would have to be designed to flow cover gas. Ultimately Silver Shield is the best material to use for the calibration gloves.

## 6.4 Building the Calibration Manipulator Gloves

Because the Silver Shield gloves that are commercially manufactured do not have a large enough opening to fit the glove ports, come in an awkward hand size and do develop pinholes along the seams, the work around solution is to make a custom glove from the Silver Shield material. The company that manufactures the material does not sell the material in bulk, however, they do manufacture a spill apron from Silver Shield that is large enough to be used.

The gloves will be made similar to the pre-made gloves in that two sides of a glove will be cut out from the spill apron and sealed together with a heat sealer. In order to make a good seal with the fine details of a glove a hand held battery operated heat sealer was found. The sealing process will be done multiple times to ensure a good seal. The hand section of the glove will be designed with less spacing between fingers than the commercially

produced gloves in order to improve handling. At the other end, the glove will be made 13" wide for the cuff so that once made the glove will fit over the 8" glove port without need to stretch the material.

## 6.5 Conclusion

Gloves play an integral part in the deployment of calibration sources and are used regularly in SNO+. The challenged faced with integrating gloves in a low background system is that typically used glove materials are known to permeate radon, a source of background for both double beta and solar phase. Thus two low permeable materials, Butyl and Silver Shield, have been identified and studied to determine the best glove material to use in SNO+. Silver Shield was found to have the lowest permeation rate of only $1.1 \times 10^{-6}$ radon atoms per hour, with Butyl coming in second with a rate of 480 radon atoms per hour.

While Silver Shield definitely is superior in mitigating radon permeability, it does not function ideally as a glove. In order to reduce the radon permeation rate for Butyl, that functions much better as a glove, an active reduction model has been theorized. This method involves flowing cover gas on both sides of the glove while isolated from the detector, which pulls out radon left inside the glove membrane from exposure to mine air. This method is more efficient for thinner gloves as well and for Butyl gloves allows around $3 \times 10^{-2}$ radon atoms to permeate for one hour of use inside the Universal Interface. This also assumes that after each use the gloves are kept in the flowing cover gas for 3 days.

As a result the Silver Shield gloves still have a lower permeation rate which does not depend on a rigorous method to achieve. To improve on the usability of the Silver Shield gloves, they will be custom built to fit the needs for the calibration system and increase usability with the wearer.

# Bibliography


[1] P.A.R Ade and et. al. Planck 2013 results. XVI. Cosmological parameters. 2013.

[2] Ch. Kraus and et. al. Final results from phase II of the Mainz neutrino mass search in tritium $\beta$ decay. *Eur. Phys. J. C*, 40:447–468, 2005.

[3] C. D. Ellis and W. A. Wooster. The Average Energy of Disintergration of Radium E. *Proc. R. Soc. Lond.*, 117(776):109–123, December 1927.

[4] W. Pauli. Offener Brief an die Gruppe der Radioaktiven bei der Gauvereine Tagung zu Tüb, December 1930.

[5] J. Chadwick. Possible existance of a neutron. *Nature*, 129:312, Febuary 1932.

[6] E. Fermi. Tentativo di una teoria dei raggi $\beta$. *Ricerca Scientifica*, II(12), December 1933.

[7] C. L. Cowan Jr., F. Reines, F. B. Harrison, H. W. Kruse, and A. D. McGuire. Detection of the free neutrino: A confirmation. *Science*, 124(3212):103–104, July 1956.

[8] G. Danby, J-M. Gaillard, K. Goulianos, L. M. Lederman, N. Mistry, M. Schwartz, and J. Steinberger. Observation of high-energy neutrino reactions and the existence of two kinds of neutrinos. *Phys. Rev. Lett.*, 9:36–44, June 1962.

[9] Z. Maki, M. Nakagawa, and S. Sakata. Remarks on the unified model of elementary particles. *Prog. Theor. Phys.*, 28(5), November 1962.

[10] B. Pontecorvo. Mesonium and Antimesonium. *Sov. Phys. JETP*, 6:429, 1958.

[11] B. Pontecorvo. Neutrino experiments and the problem of conservation of leptonic charge. *Sov. Phys. JETP*, 26(6), May 1968.

[12] M. L. Perl and *et al.* Evidence for anomalous lepton production in $e^+$ $e^-$ annihilation. *Phys. Rev. Lett.*, 35(22), December 1975.

[13] The ALEPH, DELPHI, L3, OPAL, SLD Collaborations, the LEP Electroweak Working Group, and the SLD Electroweak and Heavy Flavour Groups. Precision electroweak measurements on the Z resonance. *Phys. Rept.*, 427:257–454, February 2006.

[14] K. Kodama and *et al.* Observation of tau neutrino interactions. *Phys. Lett. B*, 504(3):218–224, April 2001.

[15] R. Davis Jr., D. S. Harmer, and K. C. Hoffman. Search for neutrinos from the Sun. *Phys. Rev. Lett.*, 20(21):1205–1209, May 1968.

[16] J. N. Bahcall and G. Shaviv. Solar Models and Neutrino Fluxes. *Astrophysics Journal*, 153:113, July 1968.

[17] K. S. Hirata and *et al.* Observation of $^8$B solar neutrinos in the Kamiokande-II detector. *Phy. Rev. Lett.*, 63:16–19, July 1989.

[18] D. Casper and *et al.* Measurement of atmospheric neutrino composition with the IMB-3 detector. *Phys. Rev. Lett.*, 66(20):2561–2564, May 1991.

[19] P. Anselmann and *et al.* Solar neutrinos observed by GALLEX at Gran Sasso. *Phys. Lett. B*, 285(4):376–389, July 1992.

[20] The SNO Collaboration. The Sudbury Neutrino Experiment. *Nuclear Instruments and Methods in Physics Research*, A449:172–207, 2000.

[21] Q. R. Ahmad and *et al.* Measurement of the rate of $\nu_e + D \rightarrow p + p + e^-$ interactions produced by $^8$B solar neutrinos at the Sudbury Neutrino Observatory. *Phys. Rev. Lett.*, 87:071301, June 2001.

[22] M. Nakagawam Z. Maki and S. Sakata. Remarks on the Unified Model of Elementary Particles. *Progress of Theoretical Physics*, 28:870–880, November 1962.

[23] V. Gribov and B. Pontecorvo. Neutrino astronomy and lepton charge. *Phys. Lett. B.*, 28:493–496, January 1969.

[24] A. Gando and et. al. Constraints on $\theta_{13}$ from a three-flavor oscillation analysis of reactor antineutrinos at KamLAND. *Phys. Rev. D*, 83:052002, March 2011.

[25] P. Adamson and et. al. Measurement of the Neutrino Mass Splitting and Flavor Mixing by MINOS. *Phys. Rev. Lett.*, 106:181801, May 2011.

[26] J. Beringer and et. al. Review of Particle Physics. *Phys. Rev. D.*, 86:010001, July 2012.

[27] et. al H. V. Klapdor-Kleingrothaus.

[28] M. Agostini and et al. Results on neutrinoless double beta decay of 76Ge from GERDA Phase I. *Phys. Rev. Lett.*, 111:122503, 2013.

[29] M. Auger and et. al. Search for Neutrinoless Double-Beta Decay in $^{136}$Xe with EXO-200. *Phys. Rev. Lett.*, 109:032505, 2012.

[30] A. Gando and et. al. Limit on Neutrinoless $\beta\beta$ Decay of Xe-136 from the First Phase of KamLAND-Zen and Comparison with the Positive Claim in Ge-76. *Phys. Rev. Lett.*, 110:062502, 2013.

[31] S. Abe and et al. Measurement of the 8B Solar Neutrino Flux with the KamLAND Liquid Scintillator Detector. *Phys. Rev.*, C84:035804, 2011.

[32] G. Bellini and et al. Final results of Borexino Phase-I on low energy solar neutrino spectroscopy. 2003.

[33] G. Bellini and et al. Cosmic-muon flux and annual modulation in Borexino at 3800 m water-equivalent depth. *JCAP*, 1205:015, 2012.

[34] C. Peña-Garay A. Serenelli, W. Haxton. Solar models with accretion. i. application to the solar abundance problem. *Astrophysics Journal*, 743:24, 2011.

[35] C. Lunardini A. Friedland and C. Peña-Garay. Solar neutrinos as probes of neutrino-matter interactions. *Phys. Lett. B.*, B594, May 2004.

[36] M. Gonzalez-Garcia J. Bahcall and C. Peña-Garay. Does the Sun Shine by *pp* or CNO Fusion Reactions? *Phys. Rev. Lett.*, 90:131301, 2003.

[37] A. Gando et al. Reactor On-Off Antineutrino Measurement with KamLAND. *arXiv:1303.4667*, 2013.

[38] E. Guillian. *SNO+-doc-14-v1*, May 2007.

[39] S. Dye. Geo-neutrinos Status and Prospects. May 2012.

[40] T. Araki and et al. Experimental investigation of geologically produced antineutrinos with KamLAND. *Nature*, 436:499–503, July 2005.

[41] D. Klein A. Burrows and R. Gandhi. The Future of Supernova Neutrino Detection. *Phys. Rev.*, D45:3361–3385, 1992.

[42] C.J. Virtue. SNO and Supernovae. *Nucl. Phys. Proc. Suppl.*, 100:326–331, 2001.

[43] S. P. Korte. Simulating Supernova Physics at SNO+. August 2009.

[44] M. J. Reid. The distance to the center of the Galaxy. *Annual review of astronomy and astrophysics*, 31:345–372, 1993.

[45] A. Mastbaum. $^{130}$Te $0\nu\beta\beta$ Energy Spectrum Plot. *SNO+-doc-1975-v1*, July 2013.

[46] K. Majumdar. $^{214}$Bi Background Rejection in the Trigger Window. *SNO+-doc-1520-v2*, April 2013.

[47] K. Majumdar. $^{208}$Tl Background Rejection using Alpha-Tagging. *SNO+-doc-1456-v3*, April 2013.

[48] C. Arpesella and *et al.* Direct Measurement of the $^{7}$Be Solar Neutrino Flux with 192 Days of Borexino Data. *Physical Review Letters*, 101(9):091302, 2008.

[49] K. Majumdar. $^{212}$Bi$^{212}$Po Background Tagging in the Trigger Window. *SNO+-doc-1961-v2*, July 2013.

[50] S. Grullon S. Asahi and J. Maneria. External Background Simulations Studies for NewNd. *SNO+-doc-1720-v7*, July 2013.

[51] G. Gann. Solar neutrino figures and slides. *SNO+-doc-1640-v3*, September 2012.

[52] I. Lawson. Radon Levels in the SNO+ Radon Reduction Room and Acrylic Vessel. *SNO+-doc-1453-v7*, August 2012.

[53] C. Jillings N. Fatemighomi, R. Ford and O. Li. LAB Cover Gas System Design Specification. *SNO+-doc-1960-v2*, July 2013.

[54] A. Forstner. Implementation of a Passive Pressure Equalization System Into A Low Radioactive Calibration Source Manipulator For the SNO+ Project. *SNO+-doc-125-v1*, April 2008.

[55] N. Fatemighomi. Summary of Covergas Rn Background. *SNO+-doc-2048-v1*, August 2013.

[56] C. Jillings N. Fatemighomi, R. Ford and O. Li. LAB Cover Gas System Design Specification. *SNO+-doc-1960-v2*, July 2013.

[57] M. Wojcik. Measurement of radon diffusion and solubility constants in membranes. *Nuclear Instruments and Methods in Physics Research Section B*, 61:8–11, July 1991.

[58] S. J. Schowalter, C. B. Connolly, and J. M. Doyle. Permeability of noble gases through Kapton, butyl, nylon, and "Silver Shield". *Nuclear Instruments and Methods in Physics Research A*, 615:267–271, April 2010.

[59] C. Darrach. AV Cleaniness Update. *SNO+-doc-2051-v1*, August 2013.

# Appendix A: Acrylic Vessel Cleaning

One problem with developing an extremely sensitive detector comes from cleanliness levels. For SNO+ contamination to the acrylic vessel from uranium and thorium can also be found in the mine dust. This dust is deposited from the over time onto the surface of the AV. Also from surveying the shape of the AV, targets were attached that needed to be removed. Furthermore with all the work done inside the AV dust and debris built up over time on the bottom portion. All these are very good reasons why acrylic vessel cleaning had to be done. A large part of my own personal contribution to on site work for the experiment was involved in this cleaning.

In order to reach the entire surface of a 12 m diameter acrylic vessel, two different structures were deployed. To reach the bottom hemisphere a rotating stainless steel ladder was attached to anchor points that were used for SNO. The upper hemisphere was reached by deploying a suspended platform that was attached to a rotating deck placed on top of the neck of the AV.

The cleaning process was done in two passes for each section of acrylic that was in arms reach. The first pass started with rinsing the acrylic off with ultra pure water (UPW) that was delivered directly from the UPW plant through an attached hose with an attached garden hose head for a distributed spray. Then a "bug sponge" used for cleaning cars was used in a rolling motion to remove any large debris to prevent scratching while scrubbing and the sprayed down with the UPW hose for multiple uses. Afterwords the section was sprayed down with a cleaning detergent called alconox diluted to 1% with UPW and scrubbed down with another bug sponge, usually differentiated by having different colours between sponges. Then again the acrylic is sprayed off with another pass of the UPW hose. Small pieces of

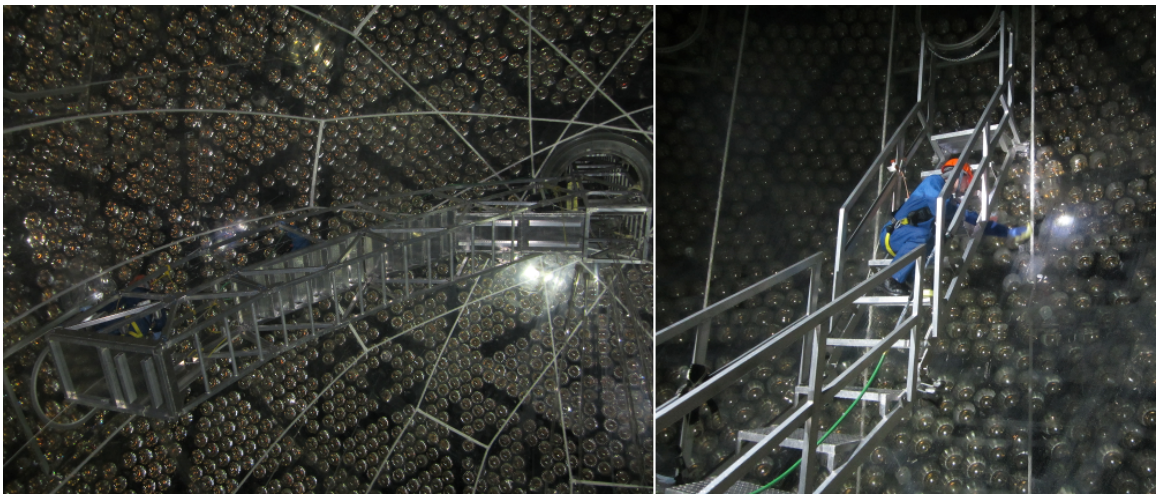

Figure A.1: Cleaning the acrylic vessel from the upper hemisphere on suspended platform and cleaning the bottom hemisphere from the cleaning ladder.

a sticky material called quickmask were used to mark areas that where cleaned.

This was done for each area reached by suspended platform or cleaning ladder, then followed up by the second cleaning pass for slice of AV before moving the suspended platform or cleaning ladder. Cleaning was done first on the upper hemisphere before going to the bottom hemisphere to have an efficient top to bottom cleaning. The second cleaning pass started with the removal of the quickmask markers on the counter clockwise direction on the upper hemisphere, because the suspended platform was rotated in a counter clockwise direction and quickmask markers were removed from clockwise side of the lower hemisphere, due to the cleaning ladder being rotated in a clockwise direction. This discrepancy came from the starting location of the suspended platform and cleaning ladder with respect to the acrylic pipes installed in the AV.

The actual cleaning after the removal of quickmask was followed by another rinse from the UPW hose followed by another spray down of alconox wash and more scrubbing. Extra care was taken in areas where the quickmask was placed to make ensure no residue left behind. After each section was washed a tape lift was taken from the bottom corner near where the quickmask was removed to be measured by an x-ray fluorescence (XRF) spectrometer. Another piece of quickmask was then placed near where the removed markers to allow overlap cleaning of the region during the cleaning of the first pass for next slice of

| Location | $^{238}$U (decays/year) | | $^{232}$Th (decays/day) | |
|---|---|---|---|---|
| | Before Cleaning | After Cleaning | Before Cleaning | After Cleaning |
| Upper Hemi. | – | 25.2 ±0.8 | – | 42 ±1 |
| Lower Hemi. | 74 ±2 | 16 ±1 | 124 ±3 | 27 ±2 |
| Neck | – | 2.47 ±0.05 | – | 4.60 ±0.08 |

Table A.1: Amounts of mine dust before and after cleaning the AV, found using the peak wing fitting method, measured using x-ray fluorescence spectrometry. [59]

acrylic.

The same method was used on the acrylic neck but instead of working on a platform or ladder a removable section was placed on the steel rungs that allowed access down the neck from the suspended platform. After sections of the neck were cleaned quickmask was used to cover the areas to prevent more mine dust and debris from building up after cleaning. When the AV was finished with the entire cleaning process the cleaning ladder was removed from the bottom and cleaning was carefully done at the very bottom to remove the last traces of debris.

The result of cleaning was determined by the tape lifts taken. The x-ray fluorescence spectrometer does not measure the backgrounds from Uranium and Thorium chains but it can determine the amount of iron. From the iron levels and known radioactivity of the dust we can infer the amount of Uranium and Thorium left on the surface of the AV and how effective cleaning is; see Table A.1. Here you can clearly see that cleaning did accomplish the goal it set out to do, to lower backgrounds from mine dust.

# Appendix B: Cover Gas Instrumentation

Part of my work included keeping track of the instrumentation that was wanted/required for the calibration and cover gas system. To allow for other individuals that had say what instrumentation was used to include their information in an easy way, Google Docs was used. Access was controlled to this document by only allowing those who had a relevant part in its formation and maintenance the URL. This was then broken up into two sections, instrumentation and gas lines.

## B.1 Instrumentation

The following tables for instrumentation have the name of the structure in which the sensors are a part of denoted in bold font. If there is also a name for the sensor system that is also found on the far left side of the tables.

The Lower UI is the section that connects the acrylic vessel with the stainless steel of the universal interface. Here the pipes for flowing in liquid into the acrylic vessel is located. The Lower UI is to be instrumented with a sense rope system, which makes use of extensometers, which is used to monitor the position of the neck of the acrylic vessel.

The Upper UI is heavily instrumented because it controls the entry to inside the acrylic vessel for calibrations. The gate valves have sensors to determine whether or not a calibration is being deployed, which is important also for the supernova trigger. The

| **Lower UI** | Sensor | # | Input | Output | D/A |
|---|---|---|---|---|---|
| Sense Ropes | Extensometer | 7 | | 4-20 $mA$ | Analog |

Table B.1: Instrumentation for the Lower UI.

| **Upper UI** | Sensor | # | Input | Output | D/A |
|---|---|---|---|---|---|
| Gate Valve Sensors | Microswitch | 12 | | | Digital |
| Glove Port Clamps | Microswitch | 8 | | | Digital |
| Instrumentation | PMTs | 4 | | | Analog |
| | Level Sensor | 2 | | | Analog |
| | Level Switch | 1 | | | Analog |
| | Oxygen Monitor | 1 | | | Analog |
| | Pressure Transducer | 1 | | | Analog |
| | Portable Oxygen Monitor? | 1 | | | Analog |

Table B.2: Instrumentation for the Upper UI.

| **Cover Gas Bags** | Sensor | # | Input | Output | D/A |
|---|---|---|---|---|---|
| Bag Monitoring | Position Sensors | 3 | | 4-20 $mA$ | Analog |
| | Webcam | 1 | | | Analog |
| U-tube system | Pressure Transducer | 1 | | | Analog |

Table B.3: Instrumentation for the Cover Gas system.

glove ports clamps which are used to isolate the the gloves from the inner UI volume are instrumented with micro-switches to ensure proper use. Other instrumentation includes a pressure transducer to determine the pressure difference between inside/outside UI, level sensors for measuring the level of the scintillator, and a sensitive oxygen monitors, possibly a portable, to determine radon contamination in the cover gas.

The cover gas bags used in the passive pressure equalization system also require their own separate set of instrumentation. This includes position sensors for each bags to determine how inflated the bags are, and a webcam to monitor the bags. Also for the emergency U-tube system a pressure transducer will be used to monitor pressure differences in the cover gas volume and as a trigger for activating the system itself.

The source storage box may also require an oxygen monitor for determining the amount of radon inside it. Furthermore since gloves will be used to manipulate sources inside the storage box, microswitches will be needed to determine when the gloves are isolated. However, since the source box is still being designed the instrumentation may change.

| **Storage Box** | Sensor | # | Input | Output | D/A |
|---|---|---|---|---|---|
| Glove Port Clamps | Microswitch | 4(?) | | | Digital |
| Instrumentation | Oxygen Monitor | 1 | | | Analog |

Table B.4: Instrumentation for the Storage Box.

| **Permanent Pump** | Gas L. | Sensors | # | Input | Output | D/A |
|---|---|---|---|---|---|---|
| UI-to-AV O-ring | 4 | Pressure Gauge | 1 | | | Analog |
| | | Flow Meter | 1 | | | Analog |
| UI Upper/Lower O-ring | 4 | Pressure Gauge | 1 | | | Analog |
| | | Flow Meter | 1 | | | Analog |
| G.V. to UI O-ring | 6 | Pressure Gauge | 3 | | | Analog |
| | | Flow Meter | 1 | | | Analog |
| Cover Gas Bags | 6 | Flow Meter | 3 | | | Analog |
| | | Actuated Valves | 3 | 24 VDC | | Analog |

Table B.5: Permanently attached cover gas quality air purge/pump system.

## B.2 Gas Lines

The gas lines are separate systems from the main cover gas system. These are used primarily for purging/pumping cover gas quality air. The gas lines are broken down further into 3 different pumping systems, a permanent pump system where the gas lines are fixed permanently, a bag pump system dedicated to depressurizing the cover gas bags, and last of all a portable pump system, where the gas lines can be attached to different connectors based on need of use. Each gas line is connected by at least one VCR connector for flowing in cover gas, the purging process, and by one VCR connector for removing excess air, the pumping process. For each pump/purge system there will be a flow meter and a pressure gauge for monitoring purposes.

The permanent pump system is primarily used for keeping radon free air between o-ring seals. This is used to prevent radon diffusion through the seals into the cover gas system. Furthermore each cover gas bag will have a gas line that can be opened using actuated valves and monitored with flow meters to inflate the bags if needed.

| **Bag Pump** | Gas L. | Sensors | # | Input | Output | D/A |
|---|---|---|---|---|---|---|
| | 1 | Flow Meter | 1 | | | Analog |
| | | Actuated Valve | 1 | 24 VDC | | Analog |

Table B.6: Permanent pump system used to depressurize the cover gas bags.

| **Portable Pump** | Gas L. | Sensors | # | Input | Output | D/A |
|---|---|---|---|---|---|---|
| Portable Line #1 | 2 | Flow Meter | 1 | | | Analog |
| | | Pressure Gauge | 1 | | | Analog |
| Portable Line #2 | 2 | Flow Meter | 1 | | | Analog |
| | | Pressure Gauge | 1 | | | Analog |

Table B.7: Pump system with de-attachable gas lines to use on an as needed basis.

The cover gas bag pump is used to depressurized the cover gas bags. It is controlled with an actuated valve which when opened, closes the connection to the cover gas and when closed, opens back the connection to the cover gas.

The idea behind having a portable pump system is to decrease the amount of gas lines, along with their respective sensor. Also by not having to purge/pump certain locations all the time the cost of cover gas quality air can be reduced. For sake of convenience, two sets of gas lines are connected to the portable pump system. For example, these two lines can be used simultaneously during connection to the source storage box for purging the a selected source transfer tube and its corresponding gate valve separation tube.

The different connection purge/pump pairs for the portable gas system are listed in Table B.8. Notice that there are only 4 connection pairs for glove port o-rings and isolation volume. This is because it does not make much sense to purge/pump each glove port separately and so each pair will have connecting tubes.

| **Portable Connections** | # |
|---|---|
| G.V. to Source Storage O-rings | 3 |
| G.V. Separation Tube O-rings (UI) | 6 |
| G.V. Separation Tube O-rings (UI) | 6 |
| G.V. Separation Tube (UI) | 3 |
| G.V. Separation Tube (Source Storage) | 3 |
| Glove Port O-rings (UI) | 4 |
| Glove Port O-rings (Source Storage) | 2 |
| Glove Isolation Volume (UI) | 4 |
| Glove Isolation Volume (Source Storage) | 2 |
| Source Transfer Tube | 3 |

Table B.8: Pairs of connection spots where the portable pump can be utilized.